

Thin films preparation
of $\text{Fe}_{3-x}\text{Co}_x\text{O}_4$ with $x = 0, 0.1, 0.5, 1$
and their properties

Inaugural - Dissertation
zur
Erlangung des Doktorgrades
der Mathematisch-Naturwissenschaftlichen Fakultät
der Universität zu Köln

vorgelegt von
Akfiny Hasdi Aimon
aus Padang, Indonesien

Köln 2014

Berichterstatter: Prof. Dr. T. Michely
Prof. Dr. L. H. Tjeng
Tag der mündlichen Prüfung: 21.10.2014

Contents

1	Introduction	1
1.1	Tunability of physical properties in ferrites thin films	1
1.2	Structure and properties	4
1.2.1	Magnetite (Fe_3O_4)	4
1.2.2	Cobalt Ferrite (Fe_2CoO_4)	6
1.3	Scope of this thesis	7
2	Experimental Techniques and Set-up	9
2.1	Thin films growth	10
2.1.1	Epitaxy	10
2.1.2	Molecular Beam Epitaxy (MBE)	12
2.2	RHEED and LEED	14
2.2.1	RHEED	14
2.2.2	LEED	17
2.3	X-Ray Diffraction	19
2.4	Spectroscopy	21
2.4.1	XPS	23
2.4.2	XAS	25
2.5	Magnetometry (SQUID)	28
3	Epitaxial growth and structural characterization of $\text{Fe}_{3-x}\text{Co}_x\text{O}_4$ films	31
3.1	Introduction	31
3.2	$\text{Fe}_{3-x}\text{Co}_x\text{O}_4$ thin films growth	32
3.2.1	Substrate preparation	32
3.2.2	Growth conditions	34
3.3	Structural characterization	35
3.3.1	In-situ RHEED and LEED	35
3.3.2	Ex-situ XRD	41
4	X-ray Photoemission study of $\text{Fe}_{3-x}\text{Co}_x\text{O}_4$ Thin Films	47
4.1	Introduction	47
4.2	Experiment	48
4.3	Results and Discussion	48
4.3.1	Core Levels	49
4.3.2	Valence band	54

5	Initial study of sites occupation on $\text{Fe}_{3-x}\text{Co}_x\text{O}_4$ films by X-ray Absorption (XAS)	59
5.1	Introduction	59
5.2	Experiment	60
5.3	Results	60
5.3.1	Substitution dependence	62
5.3.2	Thickness dependence	64
6	Magnetic study of $\text{Fe}_{3-x}\text{Co}_x\text{O}_4$ films	69
6.1	Introduction	69
6.2	Experimental	70
6.3	Results	71
6.3.1	Bulk magnetic properties of $\text{Fe}_{3-x}\text{Co}_x\text{O}_4$ films	71
6.3.2	Magnetic anisotropy induced by strain in Fe_2CoO_4 films	74
7	Summary	81
	Bibliography	85
	Abstract	93
	Kurzzusammenfassung	95
	Acknowledgement	97
	Erklärung	99
	Curriculum vitae	101

Introduction

1.1 Tunability of physical properties in ferrites thin films

During the past decades, transition metal (TM) oxide compounds have attracted growing research interest because of their promising applications in microelectronic, and microwave devices as well as sensitive sensors. In particular, these materials display a variety of unique magnetic and electronic properties such as magnetoresistance (MR), magnetoelectric and magneto-optic effects, as well as others that result in their prospective applications for data storage and switching devices involving actuators and transducers [1–5]. These properties are now commonly understood to have their main origin in the strongly correlated 3d electrons occupying the incomplete 3d orbitals in the transition metal cations.

For advanced applications, it is often desirable to have materials with magnetic properties which can be effectively controlled by external parameters such as applied electric field, elastic stress, or light. In this respect, ferrites, Fe_3O_4 (magnetite), is a highly promising candidate. Firstly, it has a high Curie temperature of $T_c \approx 860$ K and according to band-structure calculation, it is expected to be half-metal [6–9]. Secondly, recent experiments show that the MR value of Fe_3O_4 can be enhanced by Mn substitution [10]. Thirdly, it was demonstrated that the magnetic anisotropy of Fe_3O_4 can be tuned by elastic stress imposed by a piezoelectric actuator. Moreover, this compound is known to exist in either the normal or the inverse spinel structure [11]. The degree of the two structure mixing can be quantified by an inversion parameter, λ , that is the fraction of divalent cations that reside on the octahedral sites ($\lambda=0$ for normal spinel and 1 for inverse spinel). It is known that even a small changes in λ can lead to significant changes in magnetization [12].

The physical properties of a magnetite can also be tuned through small changes in chemical composition (substitution) in addition to strain effect. For examples both the electronic and magnetic properties of Fe_3O_4 can be nicely tailored in solid solution system of $\text{Fe}_{3-x}\text{M}_x\text{O}_4$ ($M = \text{Mn}, \text{Co}, \text{Ni}$ and Zn) by proper variation of the substitution concentration (x) [13–17]. Besides, external pressure and temperature can also be employed to induce remarkable changes in the electronic structure and properties. It was shown in a nanocrystalline sintered cobalt ferrite powder, that a large magnetostriction and coupling coefficient were obtained at room temperature

for sample pressurized at 8 MPa. Further, magnetic annealing of the sample at 300 °C in a magnetic field of 0.5 T exhibited an enhanced magnetostriction and coupling coefficient [18].

In addition to the importance of thin films for device applications, it is well known that thin films can also produce novel functionalities in the associated materials since their physical parameters can be modified by their structure changes induced by substitution, thickness, and strains. Recently, doped magnetite ($\text{Fe}_{3-x}\text{M}_x\text{O}_4$, with $M = \text{Mn}, \text{Co}, \text{Ni}$ and Zn) in thin films forms were extensively studied to investigate the substitution effect on the structural and magnetic properties of magnetite, and to exploit new functional materials [19–26]. They show that the degree of substitution can control the conductivity of spinel ferrite. The resistivity and density of states near the Fermi energy of $\text{Fe}_{3-x}\text{M}_x\text{O}_4$ thin films behaves systematically upon substitution. Moreover, the magnetic structure of $\text{Fe}_{3-x}\text{M}_x\text{O}_4$ have shown that the magnetic moment behaves nonlinearly with the substitution agent and does not obey Neel’s theory of ferrimagnetism [19–25]. This has been attributed to changes in the strength of the magnetic interactions among the different cations.

Apart from the substitution effect, the thin films properties can also be tuned by the films thickness. It has been reported by Lisfi *et al.* [27] that the spin reorientation in Fe_2CoO_4 thin films epitaxially grown along the (100) axis of MgO substrate can be affected by structural transition in the film from a tetragonal to cubic symmetry induced by the films thickness variation. Another evident is also reported by Moyer *et al.* [28] that the effect of film thickness on magnetic properties of $\text{Fe}_{3-x}\text{Co}_x\text{O}_4$ films shown a superparamagnetic state in ultrathin sample.

The strain effect as a consequence of the substrates used has been shown to provide the possibility for inducing ferroelectric (FE) and ferromagnetic (FM) coupling leading to more efficient electric-magnetic field controllability of the related device operation [29, 30]. Meanwhile, a number of studies have been carried out in order to understand the correlation between the magnetic behaviors and the strain of Fe_2CoO_4 thin films. For examples, Liu *et al.* has reported their studies on Fe_2CoO_4 films grown on glass and single-crystal quartz substrates by sputtering method [31]. They found that the high coercivity mechanism is associated with nanocrystalline structure, in particular the presence of relatively large residual strain in the sample. Meanwhile, Huang *et al.* also revealed that the strong magnetic anisotropy is highly dependent on the lattice-mismatch induced strain in Fe_2CoO_4 thin films epitaxially grown on SrTiO_3 and MgO (001) [32]. In a most recent report by Moyer *et al.* It was shown that λ can be increased and decreased by the application of compressive and tensile epitaxial strains. These changes result in the changes of the transition metal cations distribution in the A and B lattice sites (to be explained later in section 1.2.1) as well as the film conductivity [33]. Taken all together, in view of those interesting versatile and tunable properties of magnetite, the thin films of this material has become a focus of recent research activities.

It is worth noting, that instead of applying hydrostatic pressure on bulk sample which is limited to producing compressive strain only, epitaxial strain can produce both compression and tensile strains to a thin film sample. This is achieved by simply choosing the sign of the lattice mismatch between substrate and films. Moreover, a 2% of epitaxial strain between the substrate and the film is equivalent to the effect of 10GPa hydrostatic pressure. It should be noted that a strain of a few percents can be easily realized by epitaxial growth as long as the thickness of the layer is smaller than the critical thickness for spontaneous dislocation. The additional advantage of epitaxial strain is the possibility to expand or compress the crystal structure along the direction perpendicular to the surface which can not be achieved by hydrostatic pressure. Thus, the epitaxial growth process can deform the unit cell of the film from cubic into tetragonal symmetry, which will in turn give rise to changes of certain physical properties of a thin film [34, 35]. An example presents in figure 1.1 which is associated to a simple schematic diagram of the energy levels due to tetragonal distortion in octahedral symmetry.

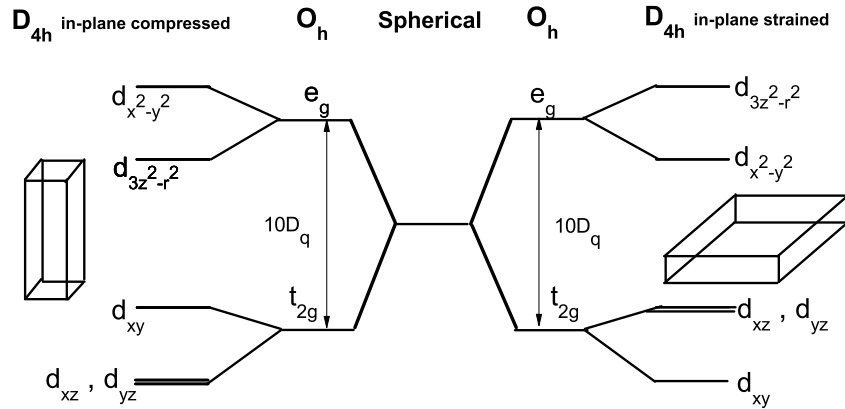


Figure 1.1: The d energy levels diagram for a transition metal atom in a tetragonal distorted octahedra.

However in this study, it will only focus on the study of the influences of Co-substitution and epitaxial strain on the physical properties of $\text{Fe}_{3-x}\text{Co}_x\text{O}_4$ thin films. In addition, the thickness dependent of $\text{Fe}_{3-x}\text{Co}_x\text{O}_4$ thin films is also studied to figure out the cations distribution behavior in this compound. In the next section, a brief introduction will be given on the most relevant bulk properties of Fe_3O_4 and Fe_2CoO_4 systems.

1.2 Structure and properties

1.2.1 Magnetite (Fe_3O_4)

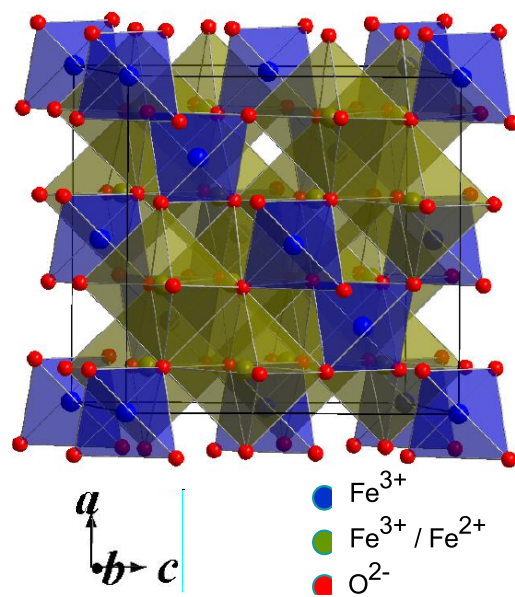


Figure 1.2: The inverse spinel structure of Fe_2CoO_4 . It consists of an fcc network of oxygen anions (small red spheres) with cations occupying different interstitial sites of the fcc lattice, resulting in tetrahedrally coordinated A-sites (blue) and octahedrally coordinated B-sites (green). Picture has been generated using Diamond.

Prior to detailed discussion of the structure and properties of Cobalt Ferrite (Fe_2CoO_4), it is helpful to give a brief introduction recalling what are commonly known about Magnetite (Fe_3O_4) which is the mother compound of the ferrites. The Fe_3O_4 compound is known to have the inverse spinel crystal structure with space group $Fd\bar{3}m$ as sketched in figure 1.2. It has a slightly distorted cubic close packed lattice of O^{2-} anions as its basis. The lattice constant of Fe_3O_4 is 8.394 \AA [36]. The Fe_3O_4 is among the most interesting iron oxides due to the presence of Fe cations in two valence states; namely the ferrous Fe^{2+} and the ferric Fe^{3+} ions. The Fe^{2+} ions are known to be located in the octahedral (B) sites only, while the Fe^{3+} are found to reside in both octahedral (B) sites and tetrahedral (A) sites. A simple schematic picture of the electron configuration in this compound is shown in figure 1.3.

It is well known that in each lattice site, the spins of Fe^{3+} and Fe^{2+} in the B sites are aligned in ferromagnetic order. Often this is explained in term of a double exchange mechanism as shown in figure 1.4. However, it is the strong antiferromagnetic superexchange coupling between the A sites and the B sites that

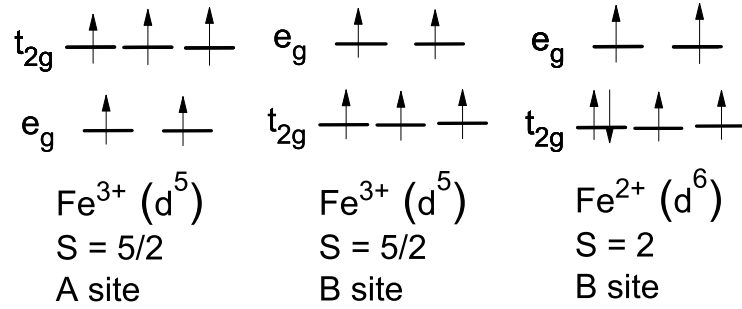


Figure 1.3: a) The electron configurations of Fe^{3+} in tetrahedral site and those of Fe^{3+} and Fe^{2+} in octahedral site. All the tetrahedral and octahedral sites are high spin state (weak crystal field).

makes the B sites to have the same spin alignment. As a result the total spins of the system arises from the sole configuration Fe^{2+} leading to a net magnetic moment of $4 \mu_B$ per formula unit of Fe_3O_4 . Consequently, the Fe_3O_4 is effectively a ferrimagnetic material with a Curie temperature T_C of 858 K.

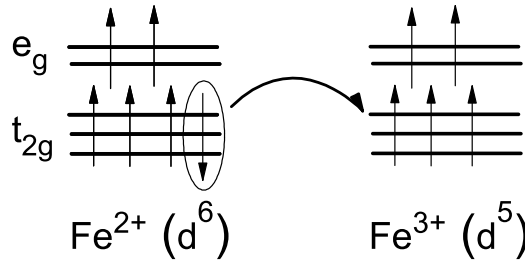


Figure 1.4: The double-exchange mechanism giving ferromagnetic coupling between ions participating in $\text{Fe}^{2+}/\text{Fe}^{3+}$ electron transfer.

At room temperature, Fe_3O_4 is known to exhibit reasonable conductivity due to the hopping of electrons between the Fe^{2+} and Fe^{3+} ions in the octahedral strings. The ferromagnetic alignment of neighboring ions is shown to maintain the high-spin arrangement of electrons on both the donating and the receiving ion. When the compound is cooled down through the Verwey transition temperature T_V of 124 K in bulk Fe_3O_4 crystal, the electron hopping freezes out, leading to an ordered array of Fe^{2+} and Fe^{3+} ions and an increase of resistivity by over two orders of magnitude [37]. This transition is also marked by the concurrent change of the crystal structure from cubic to monoclinic, along with the changes of orbital and charge orders.

1.2.2 Cobalt Ferrite (Fe_2CoO_4)

One of the most important attributes or advantages of ferrites is the very high degree of their compositional variability. Among the most well known compounds is Cobalt Ferrite (Fe_2CoO_4). The Fe_2CoO_4 is a hard magnetic material with high degree of magnetic anisotropy and magnetostriction. The unique magnetic properties of this material can be understood from its structural and electronic configuration. The study of magnetism in Fe_2CoO_4 has recently become a focus of material research due to its promising applications for oxide based magnetoelectric devices, in particular in nanocrystalline form [18].

A previous Neutron diffraction measurement on powder Fe_2CoO_4 sample confirmed that the Fe_2CoO_4 has inverse spinel structure [38]. Specifically, the Co^{2+} ions were found to occupy the B site replacing the Fe^{2+} whereas the Fe^{3+} ions were shown to be distributed equally in the A and B sites. A unit cell of Fe_2CoO_4 is also shown to have a face-centered cubic (fcc) structure with the lattice parameter (a_0) of 8.3765 Å. This is perceptibly shorter than that for Fe_3O_4 (8.394 Å) mention in previous subsection. Comparing this parameters of Fe_3O_4 and Fe_2CoO_4 one readily concludes that the structure of the Co-doped crystal has become compressed due to the presence Co atoms in the structure.

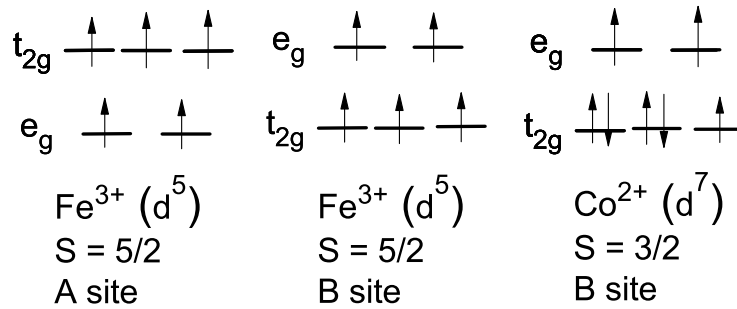


Figure 1.5: The electron configurations of Fe^{3+} in tetrahedral site and those of Fe^{3+} and Co^{2+} in octahedral site. All the tetrahedral and octahedral sites are high spin state (weak crystal field).

The electron configuration of Fe_2CoO_4 is shown in figure 1.5. Recalling that in the case of Fe_3O_4 the eight Fe^{3+} ions in tetrahedral sites are aligned antiferromagnetically with respect to the remaining eight Fe^{3+} ions in octahedral sites via superexchange interactions mediated by oxygen ions. Thus the uncompensated Co^{2+} ions which have three unpaired electrons in their d -orbitals would give a theoretical saturated magnetization of $3 \mu_B$. This turns out to be smaller than the experimental value ($3.35 \mu_B$ at 300K) given by Neutron data [38]. The discrepancy between the theoretical and experimental values could be attributed to two factors. Firstly,

the calculation was done by neglecting the contribution from the orbital motion of electrons. Secondly, the Fe^{3+} moments in the A and B sites were assumed to be aligned in perfect anti-parallel directions, while in reality they may be canted. In addition, the distribution of the cations in different sites may not be as perfect as assumed.

Still another interesting effect of Co-substitution in Fe_3O_4 is worthwhile to be presented in this connection. As mentioned earlier, the Fe_3O_4 is known to be conductive magnetic material at room temperature. It was shown however that adding the Co ions in the compound can increase the resistivity of the Fe_2CoO_4 up to $10^7 \Omega\text{cm}$ [39]. This drastic change may partly due to the effective replacement of Fe^{2+} by Co^{2+} which has a different electronic structure from the Fe^{2+} ions.

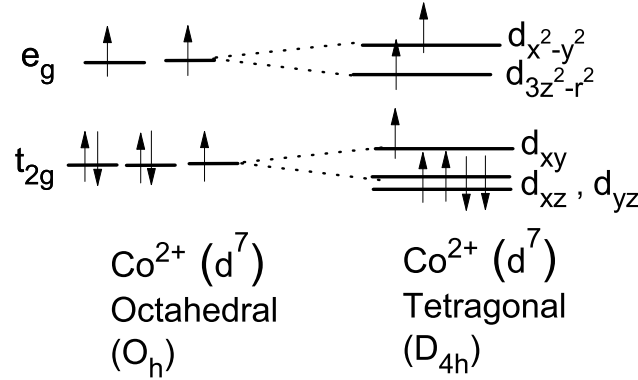


Figure 1.6: The change in the Co^{2+} orbital energy scheme and electron configuration induced by J-T distortion.

Besides, as described early, Co-substitution is also expected to induce structural change which will intern modify overall electronic structure. The presence of orbital degree of freedom on the Co^{2+} octahedral site is expected to induce a weak Jhan-Teller (J-T) distortion resulting in the lowering of the octahedral symmetry to tetragonal symmetry as shown in figure 1.6, along with the resulted orbital energy split. Taken together, those changes may no longer provides the favorable condition for the electron hopping mechanism.

1.3 Scope of this thesis

This thesis is devoted to the investigation of a number of structural, spectroscopic, electric and magnetic properties of the $\text{Fe}_{3-x}\text{Co}_x\text{O}_4$ thin films for varying x ($x = 0, 0.1, 0.5, 1$). The Molecular Beam Epitaxy (MBE) method was employed to prepare the epitaxial and monocrystalline thin films. A main concern of this thesis work

is to explore the influences of the epitaxy strain on the physical properties of the films. The use of epitaxial strain is expected to modify the site occupation of the cations and the orbital ordering as well as the influences of those modification on the physical properties. For these investigation the quality and the structure of the resulted thin film are characterized by Reflection High Energy Electron Diffraction (RHEED), Low Energy Electron Diffraction (LEED) and X-Ray Diffraction (XRD). The spectroscopy study are performed by means of X-Ray Photoemission Spectroscopy (XPS) and X-Ray Absorption Spectroscopy (XAS) measurements for the purpose of determining the electron configurations of the cations. Additionally, the SQUID measurements are carried out to study the magnetic properties of the films.

Aside of the introductory chapter, the rest of this thesis will be organized as follows. In the next chapter (chapter 2), descriptions will be presented on the experimental techniques employed for sample preparation as well as the sample characterizations and physical properties measurements. Specifically, the MBE method will be explain together with the set-up used for the growth of the films. Next, the RHEED, LEED, and XPS method will be describe for in-situ measurements, while the XRD, SQUID and XAS techniques will be explain for ex-situ characterizations.

Chapter 3 contains the detailed description of the growth procedure for the $\text{Fe}_{3-x}\text{Co}_x\text{O}_4$ $x = 0, 0.1, 0.5, 1$ thin films on different substrates, namely MgO (100), MgAl_2O_4 (100), and SrTiO_3 (100). Also presented in this chapter is the explanation of the quality verification steps taken in the entire process of the films growth using RHEED, LEED and XRD measurements.

In chapter 4, it will present the result of the XPS measurement and the associated analysis of the electronic structures. The evidence of the Co valency revealed by the Co_{2p} core level spectra is presented as the result of the XPS analysis. This is followed by the discussion of the effect of Co-substitution in the Fe_{2p} and O_{1s} core level spectra. Based on the valence band spectra, one may deduce the effect of the Co-substitution on the electronic properties.

Further study on the electronic spectroscopy of $\text{Fe}_{3-x}\text{Co}_x\text{O}_4$ will be described in chapter 5. Here it will discuss the XAS spectra unraveling the ionic valencies and the local symmetry of the cations due the present of the Co atoms. The discussion on the thickness effect on the valency and the site occupation will also be given.

In chapter 6, we report the magnetic properties of the $\text{Fe}_{3-x}\text{Co}_x\text{O}_4$ films based on the SQUID measurement of the hysteresis loop characteristics. Further analysis of this data provide the information of the rotation of the magnetic easy axis due to strain effect. Moreover, the X-Ray Linear Dichroism (XLD) measurement will be shown to substantiate the study on strain effect related to the use of different substrate by proving the information of the spin orientation and also orbital occupancy as a function of the epitaxial strain. Finally, in chapter 7, it will summarize the work on this thesis.

Experimental Techniques and Set-up

This chapter delivers the experimental technique that was used for this thesis work. It will introduce the basic concept and the experimental set-up. Figure 2.1 shows the chamber that was used to grow thin film samples for this thesis. The MBE chamber was directly connected to LEED and XPS chamber (not shown in the figure) so that the freshly prepared samples could be transferred and measured all *in vacuo*, thereby assuring the cleanliness and reliability of the data.

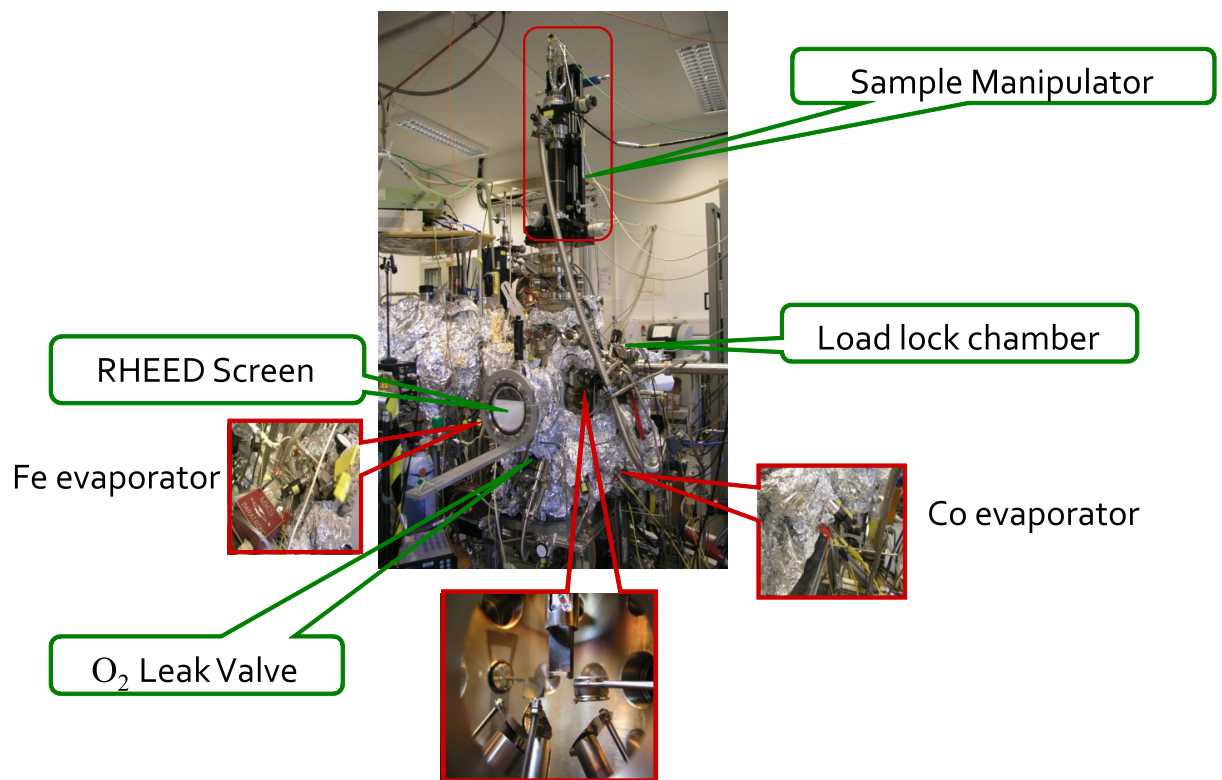


Figure 2.1: MBE set-up for film growth at the experimental Lab. in Köln.

2.1 Thin films growth

2.1.1 Epitaxy

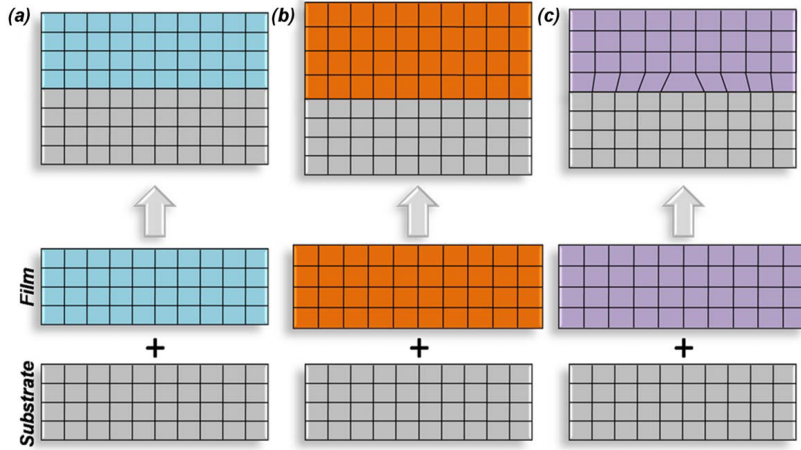


Figure 2.2: Schematic illustration of (a) nearly perfectly lattice matched, (b) strained, and (c) relaxed heteroepitaxial film growth. This figure is retrieved from Ref. [40].

Epitaxy is the extended single-crystal film formation on top of a crystalline substrate. There are two general types of epitaxy; homoepitaxy and heteroepitaxy. As the name implies, the homoepitaxy is the thin films growth on the same substrate material, for instance doped-Si on a Si substrate. It can produce high quality film, free of defects, but have a different substitution or functional nature than the substrate. The other type of epitaxy, heteroepitaxy, is the case where the film and substrate are different materials, but have similar structures that help to guide the film growth. Figure 2.2 illustrates the differences between these two epitaxy. Figure 2.2a is typical growth of homoepitaxy, while figure 2.2b and c are the heteroepitaxy type. As shown in figure 2.2a, epitaxy can be succeeded if the film material is exactly the same as the substrate or they are different materials that have very small difference in lattice parameter and interfaces so that it only gives little disturbance of the structure across the interfaces. However, if the film and substrate have different materials and also different lattice mismatch, it is possible to form one of two types of interfaces as sketched in figure 2.2b and c. Figure 2.2b is so-called strained-layer epitaxy for the film which has similar structure and lattice mismatch with the substrate (i.e., perovskite on perovskite). The last type of growth is relaxed epitaxy as shown in figure 2.2c. In this type of growth the film has a larger lattice mismatch with the substrate and even different crystal struc-

ture. As a consequence, the film turns out to have relatively quick relaxation to its bulk structure through the formation of defect, like dislocation, that accommodates interfacial strain in the system and lead to a relaxed film.

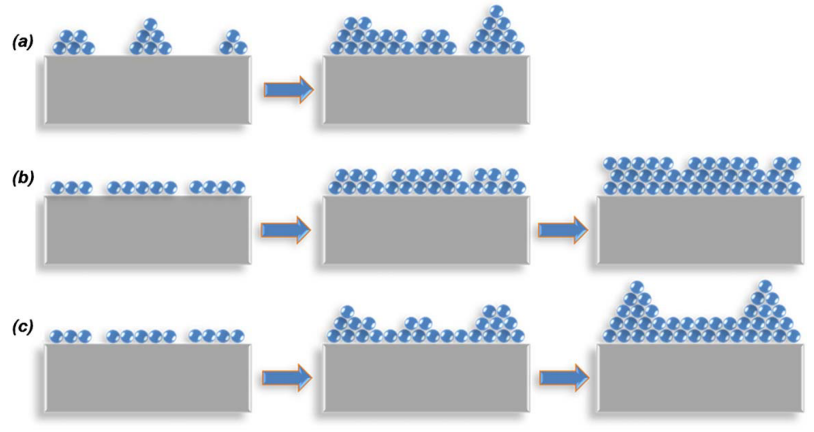


Figure 2.3: Illustration of basic growth modes: (a) Volmer-Weber (island), (b) Frank-Van der Merwe (layer-by-layer), and (c) Stranski-Krastanov. This figure is retrieved from Ref. [40].

In an epitaxy process, there are three typical modes to grow a thin film: (1) Volmer-Weber or island growth, (2) Frank-Van der Merwe or layer by layer growth, and (3) Stranski-Krastanov growth. These growth mechanisms are illustrated in figure 2.3. The Volmer-Weber or island growth (figure 2.3a) arises when the smallest stable clusters nucleate on the substrate and grow into three-dimensional island features. This growth behavior can be explained in the simple picture that the evaporated atoms or molecules have strongly bonded to each other than to the substrate material. This can be found for different film and substrate materials, for example metal grown on oxide substrates. However, the opposite characteristic is revealed by Frank-Van der Merwe or layer by layer growth (figure 2.3b). It takes place when the extension of the smallest nucleus occurs in two dimensions resulting in the formation of planar sheets. In this type of growth mode the evaporated atoms or molecules are more strongly bonded to the substrate than each other. Therefore, each layer is progressively less strongly bonded than the previous layer. This behavior will remain continuously until it reaches the bulk bonding strength. This is typically growth mode of semiconductors and oxide materials. The final growth mode is the Stranski-Krastanov growth (figure 2.3c) which is a combination of the layer-by-layer and island growth. In this type of growth, the film starts to grow in a layer-by-layer fashion. After several monolayers this type of growth is not energetically favorable, therefore it starts to change into islands mode. This type

of growth is fairly common in a number of metal-metal and metal-semiconductor systems.

2.1.2 Molecular Beam Epitaxy (MBE)

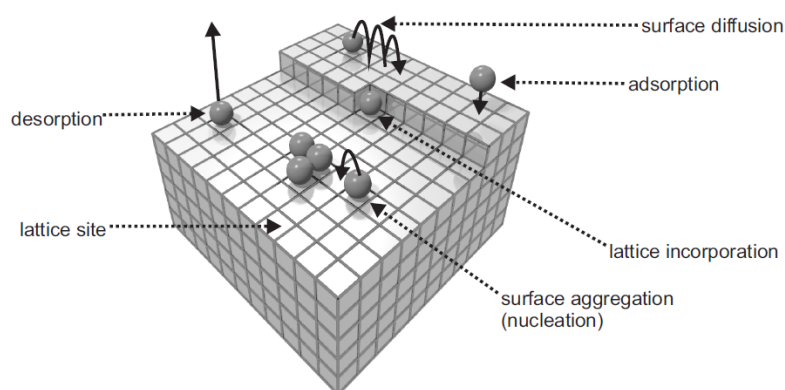


Figure 2.4: Schematic illustration of the fundamental processes for thin film deposition. This figure is retrieved from Ref. [41]

Molecular Beam Epitaxy is a thin film growth technique in which the materials in the form of molecular or atomic beams condensate at a heated substrate surface under certain growth conditions. The MBE growth mechanism involves three steps; the production of molecular beams, the transport of molecular beams to the substrate and the deposition of the molecular beams onto the substrate. The molecular beam can be generated by the effusion cell (Knudsen cell) or electron beam (e-beam) evaporators. In an effusion cell the material is evaporated from crucible that is surrounded by a heating coil. For materials that require a (very) high temperature for evaporation, it can be used the e-beam evaporator. In this type of evaporator, the evaporant can be either a rod or lie in a crucible, and then the electrons are emitted from a circular filament that is positioned slightly above the evaporant. Typically, the MBE set-up is in Ultra High Vacuum (UHV) conditions which are in the $10^{-9} - 10^{-11}$ mbar range, compatible with photoelectron spectroscopy experiments. The last step for the MBE growth process is the deposition of the molecular beams onto the substrate. These fundamental processes for thin film deposition on a substrate are illustrated in figure 2.4. The evaporated atoms or molecules will hit the substrate and may diffuse on the surface until the other process sets in. They may nucleate to small clusters or at special sites such

as defects or steps. However, they can also diffuse into the substrate or even be re-evaporated [41].

There are several ways to conduct thin film growth with MBE technique, one of them is co-evaporation method. In this way of growth, two or more beams are arriving simultaneously at the substrate. Another way of MBE growth experiment is modulated beam which is usually used for complex material. In this method, the beams are shuttered periodically to obtain the desired stoichiometry. Using this technique, the deposition of materials is achieved by depositing sublayers of less complex materials. This is often used for the growth of perovskite oxide (ABO_3) [42].

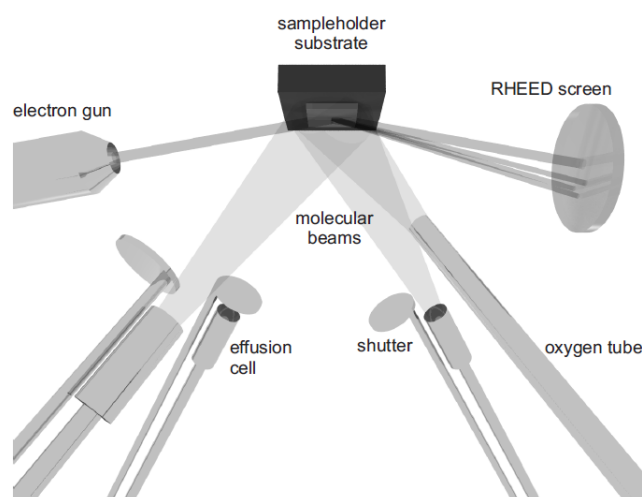


Figure 2.5: Schematic drawing of the MBE set-up. This figure is retrieved from [42].

Typically, the MBE set-up for the growth of oxides is illustrated in figure 2.5. It consists of the beam source, oxidation agent, and RHEED to control the film growth. The beam source is mounted in a vacuum chamber pointing toward the sample. As mentioned before, there are two types of beam source for solids. The beam source can be covered by shutters for precise control over the growth. In order to oxidize the evaporated atoms or molecules, an oxidizing gas is supplied into the vacuum chamber. The gas source which is commonly used is molecular oxygen (O_2). But O_3 , NO_2 , H_2O_2 or plasma (atomic oxygen, O) are also used to increase the oxidizing power. The oxidizing gas is supplied through a tube connected with a leak valve. RHEED is used not only to give valuable information on the growing surface, but also to provide feedback for the control of shutters.

2.2 RHEED and LEED

Common techniques to characterize the surface structure of thin films are Reflection High-Energy Electron Diffraction (RHEED) and Low-Energy electron Diffraction (LEED). These techniques are very surface sensitive. The electron beam is generated to the sample and then scattered from the sample. The structural information can be acquired by analyzing the diffraction pattern. The diffraction pattern is directly related to the reciprocal lattice, so that the evaluation of the crystal structure can be straightforward.

Based on diffraction theory, the wave vectors k_0 and k' of the incident and diffracted beams differ by a reciprocal-lattice vector G as in eq. 2.1. By considering the elastic scattering events, the energy is conserved, i.e., $|k'| = |k_0|$. This diffraction condition can be depicted by the geometrical structure of the Ewald sphere in the reciprocal space.

$$k' - k_0 = G. \quad (2.1)$$

Since the probing particles are electrons, one can determine the momentum k_0 which will determine the size of the Ewald sphere, by using equation 2.2, at a certain electron energy. The magnitude of the electron momentum is determined by the kinetic energy (E), where m_0 is the rest mass of the electron. The second term under the square root is the relativistic contribution.

$$k_0 = \frac{1}{\hbar} \sqrt{2m_0E + \frac{E^2}{c^2}}. \quad (2.2)$$

2.2.1 RHEED

RHEED is an in-situ surface sensitive electron diffraction technique. It can provide information about the surface structure and morphology during growth. In an epitaxial growth, the RHEED oscillations acquire information about the growth rate and allow the growth to be controlled with atomic precision.

Typically, the RHEED setup consists of electron gun, fluorescent screen and CCD camera. The electron gun emits electrons with energy between 10 and 30 keV. This electron beam hits the surface of the growing film at a small angle. Afterwards, the diffracted electron beams are imaged on a fluorescent screen and recorded by a CCD camera.

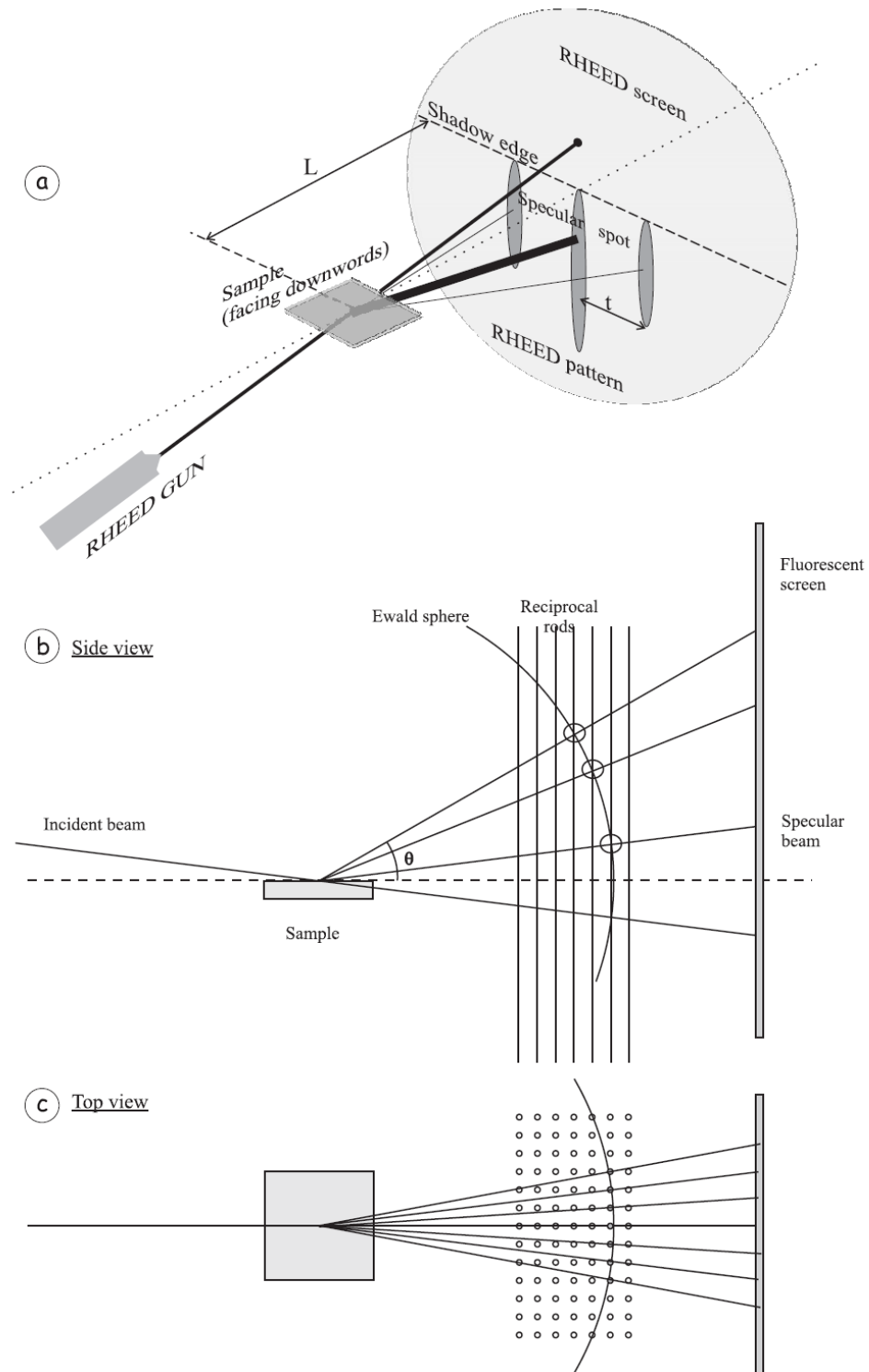


Figure 2.6: (a) Typical RHEED set-up with the Ewald sphere construction for the RHEED case, side view (b) and top view (c). This figure is retrieved from [43].

Figure 2.6 shows schematic views of the RHEED set-up and the Ewald sphere construction. The streaks (or spots) originate from the interference of the electrons which suffered elastic collisions with the surface atoms. If the surface is well ordered, the interference of these electrons gives Bragg maxima. The Bragg condition is fulfilled at the points of intersection of the rods and the Ewald sphere for a fixed angle of incidence electron beam. The resulting Bragg spots will sit on circles. In practice the reciprocal lattice rods have a finite width due to the finite size of the lateral domains and a finite coherence length of the electron beam as shown in figure 2.6. The coherence length is defined as the distance along the surface over which the diffracted electron beams still interfere constructively. It determines the upper limit of the long range order that can be studied with this technique.

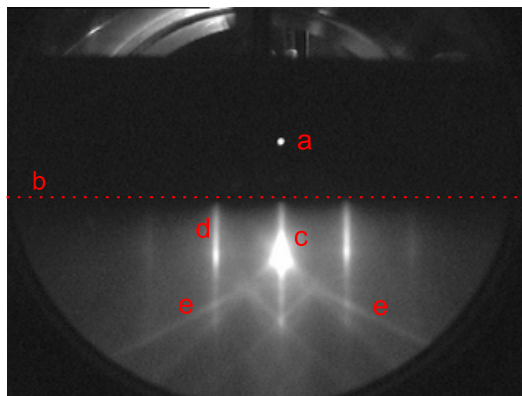


Figure 2.7: RHEED pattern of a MgO (100) single crystal: a) direct beam, b) shadow edge, c) specular (00) beam, d) off-specular (02) rod, e) Kikuchi lines

In the ideal case of a perfectly flat crystal and no divergence of the electron beam, the RHEED pattern would consist of spots on a circle. In a real experiment, however, beam divergence and crystal steps can cause some spread in k_0 , and thus the radius of the Ewald's sphere. As the diffraction condition is less strict in the out-of-plane direction, the spots can elongate in this direction to form streaks. Figure 2.7 shows typical RHEED pattern from MgO (100) single crystal. There are three clearly visible diffraction spots; the specular (00), 02 and $0\bar{2}$ diffraction lines (rods). The inelastic scattering and multiple scattering effects are also visible in this pattern due to strong interaction between electrons and matter. Kikuchi lines are one of the features that arise from the multiple scattering.

In an island growth, the transmission of the electron beam through the growing islands still can happen. As the diffraction geometry is different in this case, the pattern changes into spotty. Figure 2.8 shows a typical 3D transmission pattern of Fe_3O_4 islands on SrTiO_3 (100) substrate. Depending on the size and the spacing of the islands, several intermediate cases between a pure reflection pattern and a

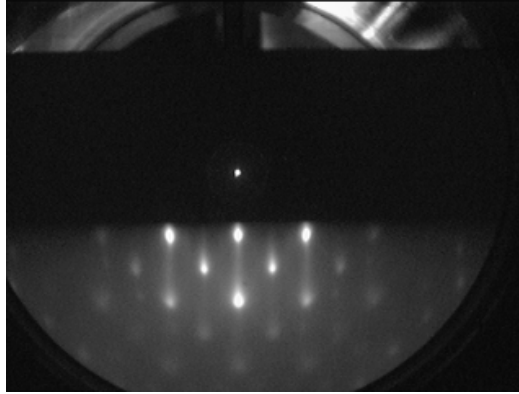


Figure 2.8: RHEED pattern of an island growth Fe_3O_4 film on SrTiO_3 (100) substrate.

pure transmission pattern can occur. Each case has completely different condition. Therefore, it is possible to distinguish reflection and transmission contributions by rotating the azimuth of the sample. Reflection spots will move, whereas transmission spots will stay.

2.2.2 LEED

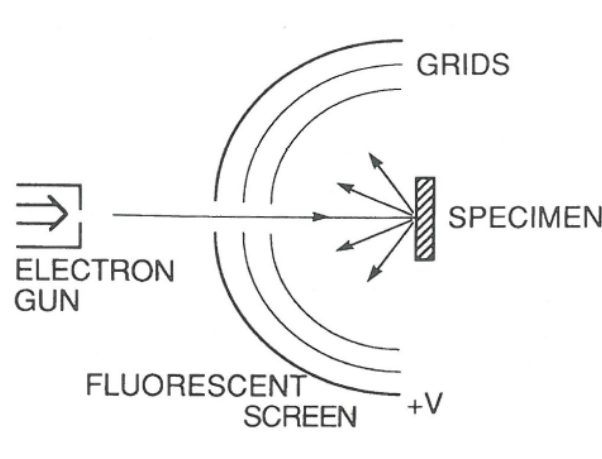


Figure 2.9: Schematic view of the LEED set-up [44].

LEED is an in-situ diffraction technique for structure identification purposes. In a typical LEED experiment, electrons with kinetic energies between 50 eV and 300 eV impinge perpendicularly on a surface of single crystal having a well or-

dered surface. The electrons are diffracted by the surface atoms and imaged on a fluorescent screen. The fluorescent screen is situated around the electron gun with a hemispherical shape centered on the crystal surface. A typical construction of LEED set-up is depicted in figure 2.9. In a LEED experiment, the Ewald sphere intersects the lattice rods at particular points that fulfill the Laue condition which defines the scattered wave vectors for diffracted beams, as shown in figure 2.10. Generally, the normal geometry is less sensitive to the topmost atomic layers. Due to the very short elastic mean free path of the LEED electrons, which range between 5\AA and 10\AA [45], LEED becomes a highly surface sensitive electron diffraction technique.

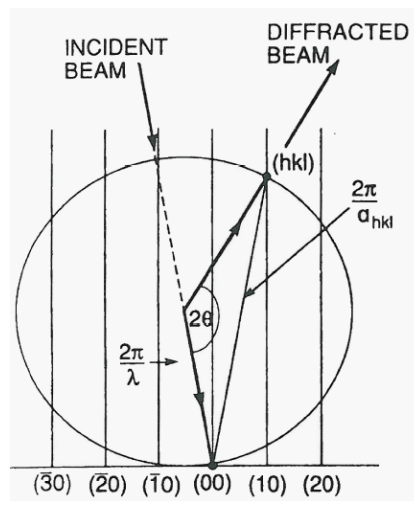


Figure 2.10: The Ewald sphere construction in LEED technique [44].

Figure 2.11 shows typical LEED picture from a well ordered surface of MgO (100) single crystal. The arrangement and the distance of the spots contain information about the surface lattice symmetry, and the in-plane lattice constant. The sharpness, brightness and profile of the spots denote the quality of the crystallinity. Intense and sharp spots and low background intensity suggest a well ordered surface. On the other hand, broadening and weakening spots, and also an increase background intensity show a presence of structural defects, crystallographic imperfections and domains. Moreover, the absence of any spots indicates considerably disorder or even polycrystallinity of the surface.

The difference between RHEED and LEED techniques is the radius of the Ewald sphere. The low electron energy at 150 eV, for example, the electrons wave length is 1\AA , and the radius of the Ewald sphere is 6\AA^{-1} , which is only three times larger than the separation between the reciprocal rods of, for example, MgO (2.1

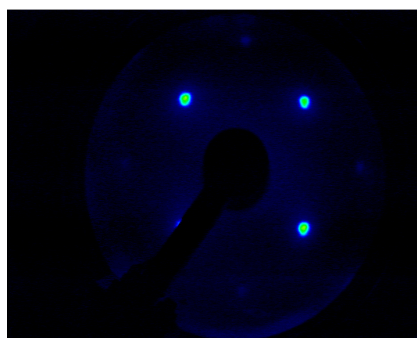


Figure 2.11: An example of LEED picture for a good crystallinity surface from a MgO (100) single crystal.

\AA^{-1}). Therefore, the Ewald sphere in LEED is comparable to the spacing of the reciprocal lattice rods. As a consequence, the intersections of the Ewald sphere with reciprocal lattice rods in LEED are much more sharply defined and the diffraction features are more similar to spots than to streaks.

Another important differences between RHEED and LEED arise from the experimental geometries. In RHEED, at very grazing incidence and at high kinetic energies (large Ewald sphere radius) only a few Laue zones are practically imaged on the screen which lies parallel to the elongated direction of the reciprocal lattice rods. Therefore, a RHEED pattern is only a projection of a small part of the surface reciprocal lattice. On the other hand, a LEED technique has the plane of the screen perpendicular to the reciprocal lattice rods and the small Ewald sphere radius, so that it can provide a projection of the full surface Brillouin zone. As a result, the LEED pattern can acquire the full symmetry of an ordered surface, whereas in RHEED it can be attained only by recording pattern at different azimuthal angles. In conclusion, RHEED and LEED techniques are two complementary techniques which combination is a powerful tool to study the translational symmetry of surface and interfaces, and the growth mode of thin films.

2.3 X-Ray Diffraction

X-Ray Diffraction (XRD) is a technique for structural characterization that can be done ex-situ. This technique investigates the structure and gives direct information about the reciprocal space. It can obtain information about the large range order in the sample. By this technique, the incident X-Ray beam is specularly reflected from a family of lattice planes at the Bragg angle. Then the scattered beam will have a sharp maximum intensity. By knowing the scattering angle, the inter planar distance can be determined from the Bragg law.

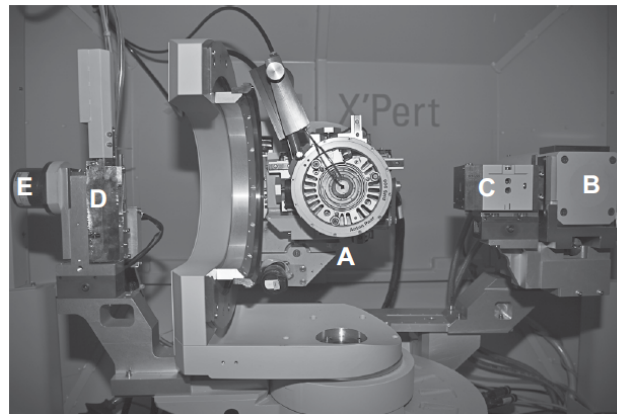


Figure 2.12: The X'pert diffractometer, a) sample stage, b) x-ray tube, c) hybrid x-ray mirror, d) diffracted beam optics, and e) detector. This figure is retrieved from Ref. [42].

The XRD measurement in this thesis used a Philips X'pert diffractometer as shown in figure 2.12. It was equipped with a hybrid mirror/monochromator for Cu $K\alpha$ radiation ($\lambda = 1.54056 \text{ \AA}$), a 4-circle goniometer, and a programmable slit in front of the detector. Figure 2.13 shows typical geometry for XRD measurement. The x-ray source (incident beam) is fixed and the sample is rotated around θ while the detector is moved by 2θ . The ψ axis allows for 180° rotation and the ϕ axis which is perpendicular to the sample surface enables 360° rotation. All rotations are done by the 4-circle goniometer. Based on this set-up, three different measurement modes can be obtained. They are x-ray reflectivity (XRR), θ - 2θ x-ray diffraction, and reciprocal space mapping (RSM).

XRR is a tool to determine the thickness of poly-crystalline or single crystalline films, and extracting information about the roughness of the surface and the interfaces. The incident beam irradiates the film at very low angles ($0^\circ < \theta < 4^\circ$) with respect to the film plane. The diffracted beam are collected in the detector at angle 2θ with respect to the incident beam after experiencing multiple reflection and refraction at the different interfaces in the film. The XRR profile shows interface fringes, the period of which indicates the total thickness of the film. The decay of XRR intensity is related to the roughness of the film surface, and of the interface with the substrate.

The θ - 2θ x-ray diffraction provides information about the chemical phases present in the sample and the out-of-plane lattice parameter (c). The diffraction pattern is obtained in the Bragg-Brentano geometry, where the incident beam is directed to the sample at an angle θ with respect to the surface plane. Then, the intensity of the reflected beam is measured at an angle 2θ with respect to the incident beam. Due to

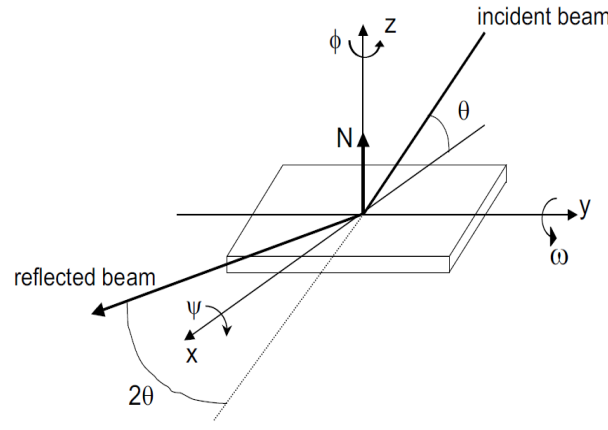


Figure 2.13: Schematic drawing of XRD geometry. This figure is retrieved from Ref. [46].

this specific geometry, the incident beam is scattered at a certain Bragg angle only at the lattice planes hkl , which are parallel to the sample surface. The out-of-plane lattice parameter can be evaluated using the Bragg equation:

$$2d_{hkl}\sin\theta = n\lambda \quad (2.3)$$

where n is an integer and has a meaning of the reflection order, λ is the wavelength, θ is the diffraction angle and d_{hkl} is the interplanar spacing and in case of cubic crystal equal to :

$$d_{hkl}\sin\theta = \frac{c}{\sqrt{h^2 + k^2 + l^2}} \quad (2.4)$$

The RSM measurement is used to study the in-plane quality of the grown film to the substrate. It can obtain information about the in-plane lattice parameter (a), the growth mode, the relaxation state, and even the imperfections in strained. This measurement is acquired by performing a set of θ - 2θ versus ω scans at different ω angles around a non-specular reflection common to the film and the substrate. The 2θ and ω are the detector and sample orientations with respect to the direction of the incident beam.

2.4 Spectroscopy

When atoms condense into solids, the electronic states of the outer electron, which is named the valence electron states (VES), are strongly affected depending on the atomic species and their arrangements in solids. The characteristic features of VES

will influence the properties of the solids. The VES comprise the partially filled conduction band states in metals and the filled valence and empty conduction band states in insulator, including the 3d electrons states of transition metal (TM) elements. Therefore, the study of VES is important in solid state physics. On the other side, inner electron (core electrons) of atoms are deeply bound inside the atoms and unchanged even when the atoms condense into solids. Core level spectroscopy is a powerful tool to study the characteristic of solid. It will excite a core electron by incident x-rays. In order to excite the core electrons, the incident x-rays must have energies larger than the core level binding energies. Every photon being absorbed by a solid must have created some kind of excitation, and by studying the intensities related to these excitations many properties of the solid can be revealed.

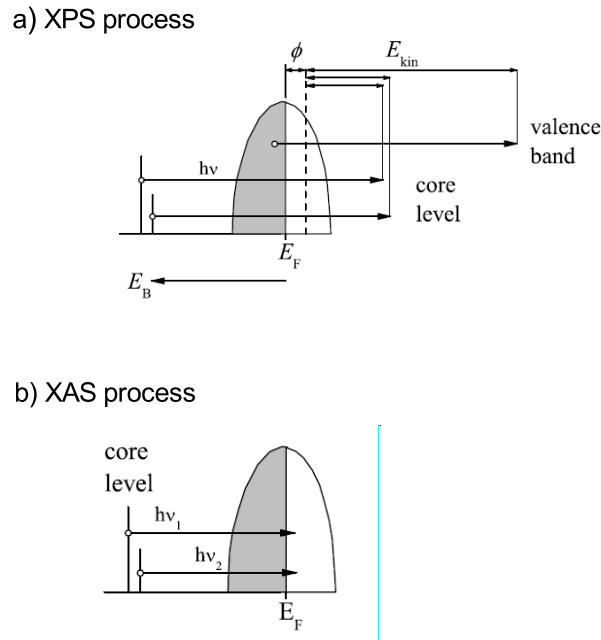


Figure 2.14: Schematic representation of XPS and XAS excitation process by using the independent particle picture. Taken from Ref. [47]

There are various kinds of core level spectroscopy, two of the famous ones are X-ray Photoelectron Spectroscopy (XPS) and X-ray Absorption Spectroscopy (XAS). They are also used in this thesis to provide information about electronic properties of $\text{Fe}_{3-x}\text{Co}_x\text{O}_4$ thin films. Figure 2.14 shows schematically the process for a simple case of these spectroscopy. In the case of XPS, a core electron is excited by the incident x-ray to the high-energy continuum states and detected as a photoelectron. On the other hand, in the XAS, a core electron is excited near to the excitation threshold just above the Fermi level. Therefore, the XPS reveals

information on the occupied electronic states, while XAS probes the unoccupied states.

2.4.1 XPS

XPS is a powerful technique to study the surface physics that can provide valuable information about the electronic structure and the chemical composition of the film. It works based on the photoelectric effect, which is the emission of electrons from a material caused by incoming photons. The energy conservation law in the photoemission process is the basis for the photoelectron spectroscopy:

$$E_{kin} = h\nu - E_B - \phi, \quad (2.5)$$

where E_{kin} is the kinetic energy, $h\nu$ the energy of the incoming x-rays, E_B denotes the binding energy, and ϕ the work function of electron analyzer. By analyzing the E_{kin} from the emission electron, the E_B of the electron in the material can be deduced.

The XPS spectrum is commonly constructed by sharp peaks at the binding energies corresponding to the core levels of the elements in the sample which come from photoelectrons with negligible energy loss. A background feature in the XPS spectrum comes from photoelectrons suffering energy losses due to inelastic scattering with others electrons inside the solid. A small deviation of E_B from the free atom value, which is denoted by the chemical shift, provides information on the chemical bonding of VES. Auger electrons peaks are also usually seen in the XPS spectrum. Auger electrons are emitted with the kinetic energies that are gained via the decay process of an electron from a higher energy level into the core hole that was created by the incoming x-rays. The kinetic energy of the Auger peaks is independent to the energy of the x-ray source. Besides studying the XPS core levels line shape, it is also great interest to study the valence band spectra. It contains a lot of information on the electronic properties of the sample.

In a one-electron approximation, the XPS spectrum can be explained with the occupied density of electronic states. If the system is weakly correlated, this approximation may be valid and methods like e.g. density-functional theory can be used to describe the spectrum of the valence band. Therefore, another method is needed to address for a correlated electrons system. There are two simple bases for understanding the photoemission process [48–50]. As a three-step process, it is divided into the excitation of the photoelectron, the traveling to the surface, and the escape from the solid into the vacuum. The photoemission process can also be considered as a one-step process, where a many body state with n electrons (as the ground state) is transformed into a final state with $n - 1$ electrons plus a free photoelectron. The binding energy is therefore defined as the difference between the

total energies of the excited final state and the ground state. A formulation of the one-step process is to express the spectral function of the photoemission as the one-particle Green's function [51]. Full-multiplet calculations like described in some literatures can also be used to interpret XPS spectra [47, 48, 52].

The many-body charge-transfer effect in the XPS spectrum can be observed as an asymmetry of the spectral shape and as satellite structures. It can be explained when the core hole is created in the XPS process, VES are polarized by the core hole potential and screen it. The polarization of VES occurs mainly by the charge transfer effect. Thus, the core hole plays a role of 'test charge', which induces the charge transfer of VES, and the effect of charge transfer is reflected in the XPS spectrum.

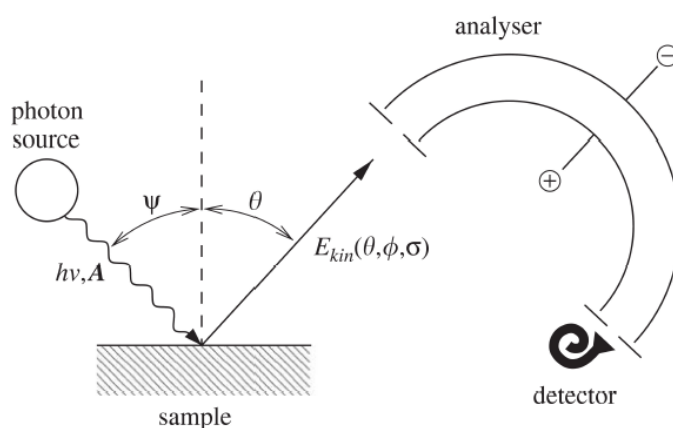


Figure 2.15: A typical XPS set-up. Taken from Ref. [53]

Typical XPS experiment consists of photon source (x-ray source), sample, analyzer and detector as shown in figure 2.15. The x-ray source is constructed by an electron gun, a water-cooled Al anode, and a Vacuum Generators twin crystal monochromator. An electron gun generated electrons and then accelerated up to 10 kV and focused on the water-cooled Al anode. After that it will emit a characteristic x-ray spectral lines together with a continuous background. The x-ray will be monochromatized by Bragg refraction at two separately adjustable quartz crystal for the Al $K\alpha$ radiation at 1486.6 eV. The monochromatized x-ray is finally focused onto the sample. The photoemission electrons are emitted from the sample and then collected using the Gramdata Scienta R3000 electron energy analyzer unit. It consists of an electron lens system, a hemispherical deflection analyzer, and a micro-channel plate (MCP) with phosphor screen as a detector unit. The electron lens system will focus the photoelectrons onto the analyzer entrance slit, and then decelerate (or accelerate) their kinetics energies in order to be matched with a se-

lected energy scanning range. At the hemispherical analyzer, an electrostatic field within two concentric hemispheres with radii of 110 mm and 190 mm is established to only allow photoelectrons of a given energy (the so-called pass energy) to arrive at the detector slits and onto the MCP detector itself. The MCP works as an electron multiplier with a gain of the order of 10^6 . These electrons will arrive at the phosphor screen, where light flashes are emitted and subsequently recorded by a CCD camera. The position of the light flash is then related to the kinetic energy of the photoelectron. The detection unit is connected to a computer and controlled via the SES software.

2.4.2 XAS

XAS is a spectroscopy technique where a core electron is excited near to the threshold by the incident x-ray through the electric dipole transition. Since the core electron state is known, the XAS spectrum delivers information on the symmetry-projected partial density of state of the excited states. The projected symmetry depends on the symmetry of the core-electron states and the selection rule of the photo-excitation including the polarization of the incident x-ray.

In XAS technique, it measures the photon energy dependent absorption of x-ray in a sample. The absorption of x-ray can be measured by using yield mode. Here, secondary effects are used to measure the absorption cross section. Upon relaxation from the photo-excited state, fluorescence photons, Auger electrons, photoelectrons, and even ions are emitted from the sample. They are supposed to give a signal that is proportional to the absorption cross section [54]. The detection technique which is used in this thesis is so-called total electron yield (TEY). It is the most frequently used detection mode because of its convenience to be implemented by collecting the drain current. The drain current is the net current of all charged particles emitted from the sample so that it can measure with high accuracy. The TEY has a probing depth about 40 Å which is good enough to measure thin film sample [55].

The interaction of x-ray with the matter can be described by Fermi's golden rule. Whereas, the probability W of a system for a transition between initial state ψ_i and final state ψ_f can be described as the following [48]:

$$W = \frac{2\pi}{\hbar} |\langle \Psi_f | \mathbf{T} | \Psi_i \rangle|^2 \delta(E_f - E_i - \hbar\omega), \quad (2.6)$$

E_i and E_f are described as the total energies of the initial and final state. \mathbf{T} is the transition operator. It is defined by dipole approximation which is customary written as:

$$\mathbf{T} = \hat{e}_q \cdot \mathbf{r}, \quad (2.7)$$

The dipole operator is only non-zero if the orbital quantum number of final and initial state differ by 1, and the spin is conserved, thus, $\Delta L = \pm 1$ and $\Delta S = 0$.

Due to dipole selection rules, XAS is quite selective in multiplet structures. It determines the final states that can be reached and with what intensity, starting from a certain initial state. As a consequence, only limited access can be visible as separate structures in the spectrum. Therefore, XAS is extremely sensitive to the symmetry of the initial state, i.e., the spin, orbital, and valence states of the element.

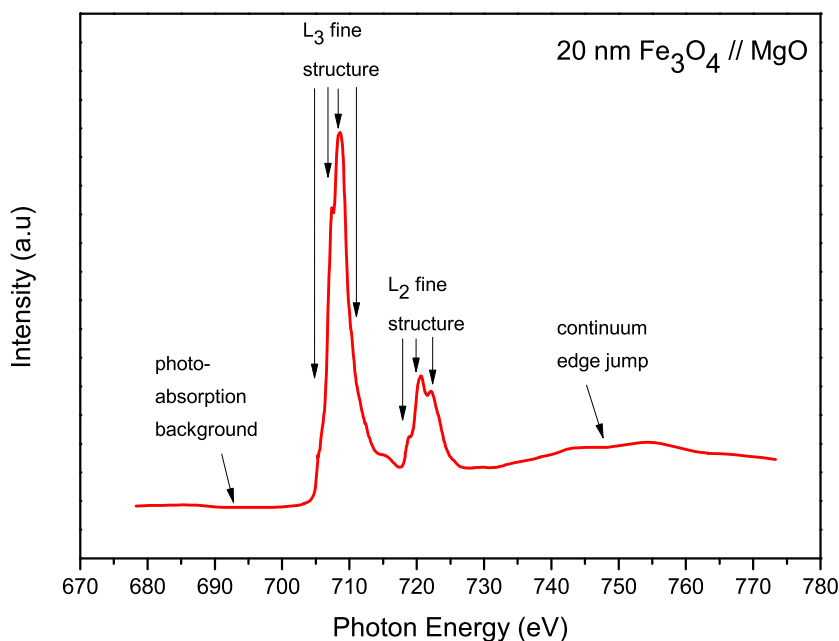


Figure 2.16: An example for Fe $L_{2,3}$ XAS spectra: 20nm Fe₃O₄ grown on MgO substrate

Figure 2.16 shows typical example for Fe $L_{2,3}$ XAS spectra of Fe₃O₄ film. There are two white lines L_3 and L_2 on the photoabsorption background. It shows fine structure that originates from the multiplet character of the final states. At higher energies, there is an edge jump due to electrons excitation into a continuum delocalized states. The absolute energy position of the main peaks depends on the potential of the atomic core. This makes XAS as element sensitive technique. The amount of screening of the core potential from the surrounding electrons also determines the energy of the main peaks. Thus XAS spectra are also sensitive to the valency. The spectra of higher valencies appear at higher photon energies by about 1 eV per different in electron occupation [56, 57].

In general, however, the satellite intensity in $L_{2,3}$ XAS spectra of transition metal compound is much weaker rather than in XPS spectra. The experimental

XAS spectral shape is mainly determined by the intra-atomic multiplet coupling effect. The physical reason for the weaker charge transfer effect in XAS is caused by the screening of the core hole potential by the excited electron in XAS. Where this excited electron stays in the 3d states and causes the screening of the core hole potential. As a result, it is suppressing a further screening by the charge-transfer effect in going from initial to final states of XAS. On the contrary with XPS, a core electron is excited to the high-energy continuum to be detected as a photoelectron and never participates in the screening of the core hole potential.

XAS measurement would not be possible without the availability of modern synchrotron light sources. It can provide a continuous spectrum of x-rays with high brilliance. Spectroscopy of an x-ray absorption edge yields rather intense spectra, and is often not a challenge in terms of statistics, but rather in needs of beam stability, good focus and small spot sizes, as well as a high degree of polarization for dichroic measurements. The x-rays are monochromatized by gratings with about 1000 lines per mm in the soft x-ray range. The XAS measurements in this thesis were done on beamlines with a 'Dragon' set-up of the monochromator, a fixed entry slit before the grating and a moveable exit slit behind it. Moreover, the experiments are even performed in UHV as soft x-ray may possess a large cross section with air. It also helps to avoid contamination and chemical reaction of the surface for the measurement, and thus enlarges the lifetime of the film surface.

2.4.2.1 Linear Dichroism

The XAS measurement by making used linear polarized x-rays is highly sensitive to the symmetry of the electronic ground state. This is the result from the dipole character of the excitation. The term 'linear dichroism' reflects when the direction of the linear polarized E vector is changed relative to the sample. In nonmagnetic system, the anisotropy arises from an anisotropic charge distribution caused by bonding. For magnetic sample, an additional anisotropy may exist to the magnetization direction of the sample. It is important to note that the measured anisotropy arises from a nonspherical charge distribution. If the origin of the charge anisotropy is from the bonding along, it is called 'natural' linear dichroism (XNLD), while for the system with magnetic contribution it is named 'magnetic' linear dichroism (XMLD).

For XNLD, the electric field factor E acts as a search light for the direction of the maximum and minimum number of empty valence states. The transition intensity is directly proportional to the number of empty valence states in the direction of E. For example, it is known that the charge distribution of the individual p and d orbitals is symmetric in space, and therefore as the symmetry is lowered below cubic, transition to individual p and d orbitals will depend on the orientation of the E-vector relative to the x,y,z coordinate system of the crystal. This is the origin of

the natural linear dichroism effect.

The XMLD originates from a spin polarization in the initial state of the XAS process. The effect comes from uniaxial spin alignment and exists for both ferromagnets and antiferromagnets. It can be observed in materials with magnetic order, or magnetized samples, and multilayer systems that are coupled magnetically.

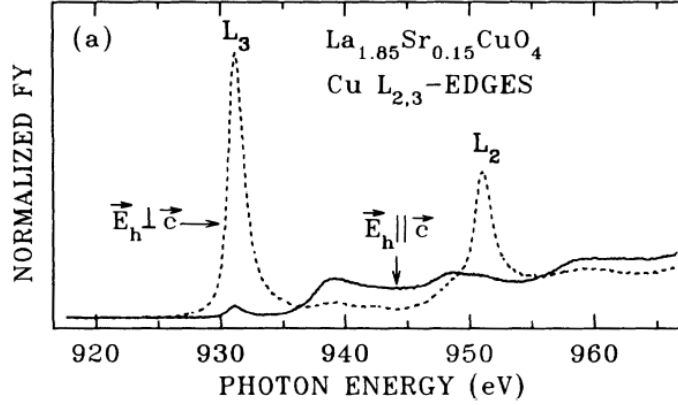


Figure 2.17: Cu $L_{2,3}$ linear dichroism spectra of $\text{La}_{1.85}\text{Sr}_{0.15}\text{CuO}_4$ for $\mathbf{E}||\mathbf{c}$ (solid line) and $\mathbf{E}\perp\mathbf{c}$ (dashed line). Taken from Ref. [58].

Figure 2.17 shows a typical example where XNLD effect can be seen on high-temperature superconductor $\text{La}_{1.85}\text{Sr}_{0.15}\text{CuO}_4$ [58]. It shows the Cu $L_{2,3}$ XAS for two polarizations, parallel and perpendicular to the tetragonal c axis. The Cu ions ($\text{Cu}^{2+} d^9$) are surrounded by an octahedron of O ions, whose (out-of-plane) c -axis is considerably elongated compared to the a -axis. Looking at figure 2.17, the spectra intensity for \mathbf{E} parallel to c -axis is almost 100% suppressing, proving that the hole of the Cu $3d^9$ configuration has an in-plane configuration.

2.5 Magnetometry (SQUID)

A superconducting quantum interface device (SQUID) magnetometer is a very sensitive device for measuring the magnetic moment of a magnetic sample. It works in a wide range of temperature between 2 and 400 K and applied magnetic field up to 7 T. This device works based on a combination of superconducting materials and Josephson junction. The flux quantization in superconducting loops and the Josephson effect allow for the detection of a variation of a magnetic field associated with one elemental flux quantization.

A typical basic component of a SQUID magnetometer consist of: a superconducting magnet, a superconducting detection coil (pick-up coil), a SQUID elec-

tronic circuit and a superconducting magnetic shield. The superconducting magnet is a superconducting wire in the form solenoid which produces uniform magnetic field to magnetize the sample. The detection coil is a single superconducting wire in the form of three counter wound coils configured as a second-order gradiometer. This configuration preserves the data signals from spurious signals caused by the fluctuation of the large magnetic field from the superconducting magnet and also reduces noise from nearby magnetic objects. The SQUID circuit component has a function to convert the induced current to the voltage. It works by measuring changes of magnetic field associated with one flux quantum. The superconducting magnetic shield will protect the SQUID sensor from the fluctuation of external magnetic field in the surrounding. The detection coils which are placed at the center of the superconducting magnet and connected to the SQUID electronic, are located in a magnetic shield and must be kept at liquid helium temperature.

The measurement is performed by moving the sample along the symmetry axis of superconducting magnet and detection coils. Due to its movement, the magnetic moment of the sample induces an electric current in the detection coils. A change of magnetic flux in these coils will change the persistent current in the detection circuit which produces variation of output voltage in the SQUID. It is essentially proportional to the magnetic moment of the sample.

One technique to measure thin film sample with SQUID magnetometer is named reciprocating sample option (RSO). With this technique, the sample is rapidly and sinusoidally moved through the pick-up coils. The application of a servo motor and digital signal processor allows for RSO technique to obtain a high sensitivity of approximately 5×10^{-9} EMU. During the measurement, a shaft encoder on the servo motor tracks the sample position and also records synchronously to the acquisition of the SQUID signal. Hence, the magnetic moment of the sample is obtained by fitting the recorded data to an ideal dipole response using a nonlinear which is named least-squares fitting routines.

Epitaxial growth and structural characterization of $\text{Fe}_{3-x}\text{Co}_x\text{O}_4$ films

3.1 Introduction

As already stated in chapter 1, the properties of Fe_3O_4 (magnetite) can be tune by substitution, thickness variation and strain effects. This thesis mainly discusses the substitution and strain effects on the structure, electronic and magnetic properties of Co-doped in Fe_3O_4 thin films. In this chapter, the growth and the structure study of $\text{Fe}_{3-x}\text{Co}_x\text{O}_4$ ($x = 0, 0.1, 0.5, 1$) with different Co concentration on MgO , MgAl_2O_4 and SrTiO_3 substrates will be described. The Fe_3O_4 is chosen as the parent compound due to its feasibility to grow in thin film form. Once good quality Fe_3O_4 films are grown, Co is doped with the concentration 3.3% ($x=0.1$), 16.25% ($x=0.5$) and 33% ($x=1$) of the metal element into the parent compound. The Co element was chosen as the substitution agent which has a big magnetocrystalline constant and tunes the magnetic properties of Co-ferrite [59, 60].

Taking into consideration the lattice mismatch, the size and the sign of the epitaxial strain in the films were controlled by a suitable choice of substrate material. The $\text{Fe}_{3-x}\text{Co}_x\text{O}_4$ is grown under tensile strain on MgO substrate. In order to have a comprehensive study on strain effects in $\text{Fe}_{3-x}\text{Co}_x\text{O}_4$ compound, MgAl_2O_4 and SrTiO_3 single crystals were also chosen as a substrate. The later substrates can provide compressive strain on $\text{Fe}_{3-x}\text{Co}_x\text{O}_4$ films and have a bigger lattice mismatch to the $\text{Fe}_{3-x}\text{Co}_x\text{O}_4$ films. Therefore, study on the growth mode of $\text{Fe}_{3-x}\text{Co}_x\text{O}_4$ on these substrates is desired to be discussed further.

The films were grown by using Molecular Beam Epitaxy (MBE) technique in a UHV chamber with the base pressure 10^{-11} mbar. By using this technique, an epitaxial growth of films with good crystallinity and single phase can be obtained. In order to study the structure and the film quality, RHEED, LEED and XRD measurements were used to characterize the films structure. RHEED and LEED characterizations were used to follow the morphology and the structure of the film growth during and after deposition. The XRD measurement complete the structure study by providing detailed information on the lattice parameters and the strain state.

3.2 $\text{Fe}_{3-x}\text{Co}_x\text{O}_4$ thin films growth

3.2.1 Substrate preparation

Epitaxial growth is a recrystallization process where gaseous atoms condense on a template created by the substrate to form a single crystal film. The substrate plays an important role in the formation of a good crystalline film. The most important crystallographic parameters for the substrate is crystalline symmetry and in-plane lattice parameter. The substrate symmetry has a big influence in determining the structure of the overlaid films, particularly in our case oxide-on-oxide epitaxy. The lattice mismatch refers to the difference of in-plane lattice parameters of the substrate and the film. The lattice mismatch can be defined as in the following formula 3.1. For a strain study, the determination of the lattice parameter of the substrate and the films is an important parameter that must be considered. If $a_{\text{film}} < (>) a_{\text{sub}}$, the film will experience a compression (tension) strain prior to relaxation.

$$f = \frac{a_{\text{sub}} - a_{\text{film}}}{a_{\text{sub}}} \quad (3.1)$$

The starting point in this study was epitaxial grow of $\text{Fe}_{3-x}\text{Co}_x\text{O}_4$ on MgO substrate which is a perfect substrate to grow $\text{Fe}_{3-x}\text{Co}_x\text{O}_4$ [22, 61]. Both the rocksalt structure of MgO and the inverse spinel structure of $\text{Fe}_{3-x}\text{Co}_x\text{O}_4$ are based upon a face centered cubic (fcc) oxygen anion lattice. This allows for continuous oxygen sublattice over the MgO and $\text{Fe}_{3-x}\text{Co}_x\text{O}_4$ interface. By using this substrate, one can ensure to prepare a clean, and a well ordered surface [22, 61, 62].

Two types of MgO substrates, which are cleaved and polished substrates, are used in this study. The cleaved MgO can be obtained by simply cutting a single crystal block (10x10x10 mm³ size, brought from MaTeck GmbH) into platelets. The best surface are obtained by laying a cubic crystal block with one edge on a solid support (such as stone table top), pressing a knife blade on the opposite edge, and then gently knocking with a hammer on the blade until the crystal separated. Thus obtained MgO platelets (size 10x10x1 mm³) contains macrosteps on the surface. The steps can have height in the order of 1 μm , and even visible with the naked eye. This quality of the MgO cleaved substrate is appropriate to study the epitaxial growth and calibrate the film thickness by RHEED oscillations. On the other hand, cleaved substrate has disadvantages for other measurements such as XPS and XAS, because the macrosteps can create the films discontinuity. Therefore polished substrates are used to overcome this problem. Polished substrates are widely available commercially. The polishing of the substrate has been done by doing mechanical polishing and/or etching with strong bases, such as H_3PO_4 , until the surface are mirror-like flat. Figure 3.1 shows the difference of the surface microscopic structure on polished (a) and cleaved (b) MgO (100) substrate [61].

The polished substrate has small grains while the cleaved substrate has steps on the surface. These substrate were brought from SurfaceNet GmbH with $10 \times 10 \times 1 \text{ mm}^3$ size.

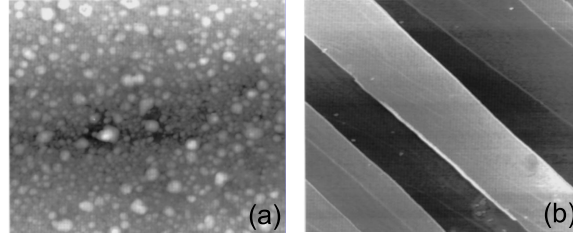


Figure 3.1: Atomic Force Microscopic (AFM) images of polished (a) and cleaved (b) MgO (100) substrate. The figures were taken from Ref. [61].

Besides MgO substrate with a lattice constant (a) 4.212 \AA , the epi-polished MgAl_2O_4 ($a = 8.08 \text{ \AA}$) and SrTiO_3 ($a = 3.905 \text{ \AA}$) were utilized as a substrate in order to study the strain effects in Fe_2CoO_4 films. The MgAl_2O_4 has the same spinel structure with Fe_2CoO_4 with fcc oxygen anion lattice, while SrTiO_3 has a perovskite structure based cubic anion lattice. By using formula 3.1 to calculate lattice mismatch with the film, one can chose the substrate to apply a different strain on the films. As already known, the lattice constants of Fe_2CoO_4 is $a = 8.3765 \text{ \AA}$ [38]. Therefore, MgO substrate has 0.3% lattice mismatch which induces tensile strain in the Fe_2CoO_4 film plane; while MgAl_2O_4 and SrTiO_3 substrates have -4% and -7.4% lattice mismatch, respectively, which induce compressive strain in the Fe_2CoO_4 film plane. The growth mode of Fe_2CoO_4 films on these substrate will be discussed in the following section.

The substrate was mounted on a stainless steel plates as a sample holder. Two stainless-steel stripes were spot-welded on both sides of the sample holder and folded over the edges of the substrate. They suppose to prevent the sample from being knocked off during handling in the UHV system. Afterward, the substrate was introduced to the UHV system throughout a load lock chamber with the base pressure of low 10^{-9} mbar .

Prior growing, the substrate has to be cleaned in order to remove the contaminants (such as water, hydrocarbon) on the substrate surface. The annealing process was done under oxygen atmosphere. The substrate was heated up at $600 \text{ }^\circ\text{C}$ and oxygen partial pressure $3 \times 10^{-7} \text{ mbar}$ for 2 hours. This way of annealing is used to ensure the cleanness of the surface and yield well-ordered crystal surface where the heat will burn any carbon contaminant at the surface and than react with O_2 to form CO_x species. Besides, annealing in O_2 might heal oxygen vacancies at the MgO surface.

3.2.2 Growth conditions

There are three parameters that influence the epitaxial growth of thin films using MBE technique: the oxidation agent, the substrate temperature and the metal flux. In this study, the molecular oxygen (O_2) was chosen as the oxidation agent since it can oxidize Fe and Co metals atom easily. Systematic studies on molecular O_2 as the oxidizing agent show that the degree of oxidation depends on the relative amounts of chemisorbed O_2 molecules and condensed atoms [63]. Beside that, substrate temperature also affects the chemisorption process of O_2 gas. To fulfill these conditions, in this study the O_2 flux and the substrate temperature are fixed during film deposition. The total metal flux is also constant but the flux ratio between Fe and Co atoms are varied depending on the atomic concentration.

The growth of Fe_3O_4 compound can turn out to be complicated since the oxidation of Fe atom with O_2 gas can possibly produce different Fe-oxides such as Fe_3O_4 , Fe_{1-x}O , $\gamma\text{-Fe}_2\text{O}_3$, and etc. The molecular oxygen will have the dissociation reaction $\text{O}_2 \rightarrow 2\text{O}$ while the oxidation reaction for Fe_3O_4 is $3\text{Fe} + 4\text{O} \rightarrow \text{Fe}_3\text{O}_4$ which consists of Fe^{3+} and Fe^{2+} ions. If the Fe rate is faster than the rate of O_2 dissociation, it will create Fe_{1-x}O (wustite) with mostly Fe^{2+} ion. On the other hand, if the Fe rate is too low, the Fe atoms will fully oxidize into Fe^{3+} ion forming $\gamma\text{-Fe}_2\text{O}_3$. In the extreme limit of low atomic oxygen production rate relative to Fe rate, Fe metal will nucleate and may form clusters if the kinetics permit. Therefore, the Fe-rate should have slightly faster than the rate of O_2 dissociation in order to grow Fe_3O_4 thin film.

In this work, the metal atoms evaporated under oxygen partial pressure of 8×10^{-7} mbar. This oxygen pressure is sufficient to oxidize the evaporated Fe atoms to form Fe_3O_4 [64]. The molecular O_2 gas was simultaneously supplied into the growth chamber through a leak valve and monitored from an ion gauge reading. The substrate temperature was set at 250°C during film deposition. This temperature was chosen to assure a good layer-by-layer growth mode and prevent the interdiffusion of the Mg atom from the substrate to the films surface [65].

Pure Fe and Co metals were evaporated from alumina crucibles onto the substrate. The flux rate was kept at $1 \text{ \AA}/\text{min}$ determined by using a calibrated quartz crystal monitor at the growth position. This rate was chosen to assure a formation of 1 monolayer (ML) of Fe_3O_4 (100) for every minute which contains 8.5×10^{18} Fe particles m^{-2} . Hence, a flux of $1 \text{ \AA}/\text{min}$ corresponds to 1.4×10^{17} Fe particles $\text{m}^{-2}\text{s}^{-1}$, forming a ML of Fe_3O_4 in 60 s (1 min). While for the $\text{Fe}_{3-x}\text{Co}_x\text{O}_4$ sample, the total metal flux was distributed between Fe and Co rates in a certain ratio calculated according to the number of cations per m^2 per second. The flux rates for the growth of $\text{Fe}_{3-x}\text{Co}_x\text{O}_4$ were tabulated in table 3.1. Similar growth conditions were employed to all samples on different substrates.

substitution (x)	0		0.1		0.5		1	
	Fe	Co	Fe	Co	Fe	Co	Fe	Co
atomic ratio	3	0	2.9	0.1	2.5	0.5	2	1
flux rate ($\text{\AA}/\text{min}$)	1.00	0.00	0.95	0.05	0.82	0.18	0.65	0.35

Table 3.1: Flux rate of Fe and Co atom for different Co-substitution concentration.

3.3 Structural characterization

3.3.1 In-situ RHEED and LEED

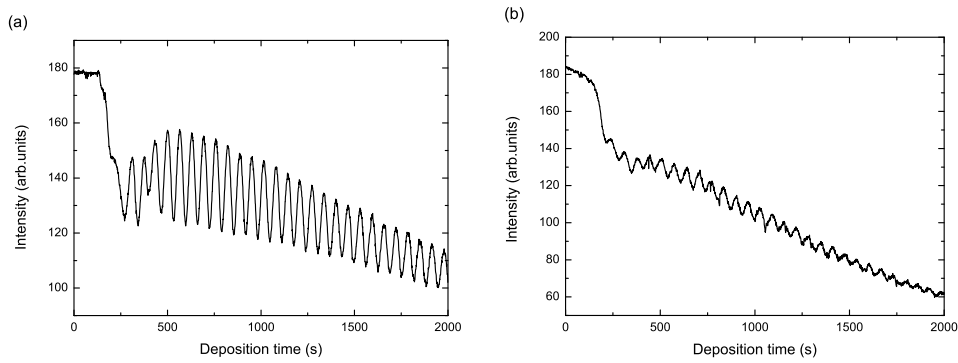


Figure 3.2: RHEED intensity oscillations of the specularly reflected electron beam during growth of a Fe_3O_4 (a) and Fe_2CoO_4 (b) films grown on cleaved MgO crystal. Every oscillation corresponds to a ML of the films.

Epitaxial films of $\text{Fe}_{3-x}\text{Co}_x\text{O}_4$ have been grown on cleaved MgO and epi-polished MgO, MgAl_2O_4 and SrTiO_3 substrates by using MBE technique. To calibrate the film thickness, Fe_3O_4 and Fe_2CoO_4 films were deposited on cleaved MgO (100) substrate to observe its RHEED oscillation during deposition. The results are shown in figure 3.2. These oscillations indicate a two-dimensional (2D) layer-by-layer or Frank-van der Merwe growth mode. It reflects the periodic changes of surface morphology and relates to the step-density as the step-length per unit area. Starting with a smooth substrate surface, the step-density will be in a minimum. Upon deposition, islands nucleate and grow out leading to an increase in step density. As deposition continues, the islands coalesce and finally form a complete monolayer. In this stage, the step density reduces to the initial value of the smooth surface, and specular intensity recovers. As a result, the period of the oscillations corresponds to the formation time of 1 ML. Based on figure 3.2, 1 ML Fe_3O_4 and

Fe_2CoO_4 films will be formed in about 64.25 and 64.7 seconds, respectively. This information was used to calibrate the film thickness. For example, 20 nm Fe_3O_4 thin film was grown for 1 hour 40 minutes.

Figure 3.3 (top panel) shows RHEED patterns (from left to right) of a clean epi-polished MgO (100) substrate (a), and 20 nm thick of $\text{Fe}_{3-x}\text{Co}_x\text{O}_4$ films with $x = 0, 0.1, 0.5$ and 1 (b-e) after the growth on epi-polished MgO (100) substrate. The patterns were taken along [100] beam incident with an electron beam energy of 20 keV. The patterns show a streak rods which indicates the presence of a smooth and flat surface. The MgO substrate has a cubic unit cell with face centered cubic symmetry. Based on Bragg's law, the diffraction streak are visible when $h + k = 2n$. Therefore, the (20) and ($\bar{2}0$) diffraction lines are clearly visible on MgO RHEED pattern. Double lattice constant of the substrate compared to the films, the in-plane dimension of the spinel unit cell of $\text{Fe}_{3-x}\text{Co}_x\text{O}_4$ are exactly twice those of the rocksalt unit cell of MgO. So that a set of diffraction rods will appear on the half spacing of the substrate diffraction rods. Consequently, the (40) lines of $\text{Fe}_{3-x}\text{Co}_x\text{O}_4$ have the same spacing as (20) line of MgO substrate. There is an extra structure on Fe_3O_4 RHEED pattern in the zeroth Laue arch zone. It is a ($\sqrt{2} \times \sqrt{2}$)R45° reconstruction which is a signature of epitaxial Fe_3O_4 pattern [61].

This reconstruction pattern is also confirmed by LEED pattern of Fe_3O_4 as shown in the bottom panel of figure 3.3b. The LEED photograph was taken at electron beam energy around 96 eV. From the pattern, one can see the number of spots become fourfold along the [100] directions. The observed patterns correspond to a c(2x2) reconstruction, with respect to the bulk unit cell of Fe_3O_4 [61]. Differing from Fe_3O_4 pattern, the LEED patterns of $\text{Fe}_{3-x}\text{Co}_x\text{O}_4$ (see Fig. 3.3c-e at the bottom panel) along [100] only show double spots (figure 3.3). Both MgO and $\text{Fe}_{3-x}\text{Co}_x\text{O}_4$ have a cubic, non-primitive unit cell with face-centered symmetry, i.e. c(1x1) [22, 66]. Based on Bragg's law, for RHEED and LEED patterns, diffraction features will occur with indices (h, l) that fulfill the condition $h + l = 2n$. Somehow in Fe_3O_4 case, the reconstruction patterns eliminates this face centered symmetry at the surface. So that, the symmetry becomes primitive cubic, i.e. c(2x2), and also diffraction features with indices $h + k = 2n + 1$ will become visible [61].

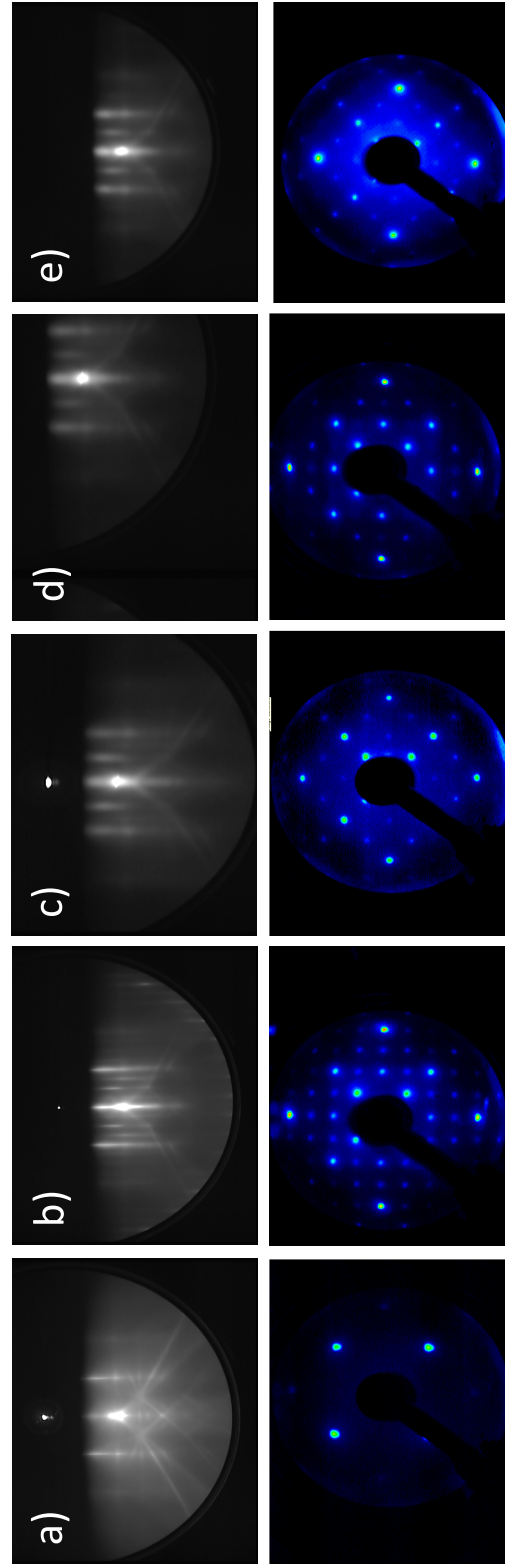


Figure 3.3: Top panel shows RHEED patterns at 20 keV electron energy on [001] direction of (from left to right) (a) MgO substrate, Co-substitution in $\text{Fe}_{3-x}\text{Co}_x\text{O}_4$ films with $x = 0$ (b), $x = 0.1$ (c), $x = 0.5$ (d), and $x = 1$ (e). The LEED pattern of the corresponding sample is showed in the bottom panel. The pattern were recorded at electron beam energies of (from left to right) 96, 96, 133, 98, 130eV.

Further study on strain effect of $\text{Fe}_{3-x}\text{Co}_x\text{O}_4$ films is continued by growing the films on MgAl_2O_4 substrate, which is supposed to give compressive strain. It has 4% lattice mismatch with Fe_2CoO_4 . Figure 3.4 shows RHEED patterns of a clean MgAl_2O_4 (100) substrate (a), and 20 nm thick of $\text{Fe}_{3-x}\text{Co}_x\text{O}_4$ films with $x = 0, 0.5$ and 1 (b-d) after the growth on MgAl_2O_4 substrate. It also shows a streak patterns suggesting the presence of a smooth and flat surface after $\text{Fe}_{3-x}\text{Co}_x\text{O}_4$ thin films deposition. Since MgAl_2O_4 substrate and $\text{Fe}_{3-x}\text{Co}_x\text{O}_4$ films have spinel structure with face centered symmetry, the $h + l = 2n$ diffraction lines are expecting to show in the pattern. Therefore, the (20) and (40) diffraction lines are visible in both MgAl_2O_4 and $\text{Fe}_{3-x}\text{Co}_x\text{O}_4$ RHEED patterns. It means that the film follows the structure of MgAl_2O_4 substrate. These RHEED patterns look similar with $\text{Fe}_{3-x}\text{Co}_x\text{O}_4$ grown on MgO substrate. The difference is the absence of the $(\sqrt{2} \times \sqrt{2})\text{R}45^\circ$ reconstruction peak on Fe_3O_4 film. It may be do to less crystalline surface quality of the Fe_3O_4 on MgAl_2O_4 substrate.

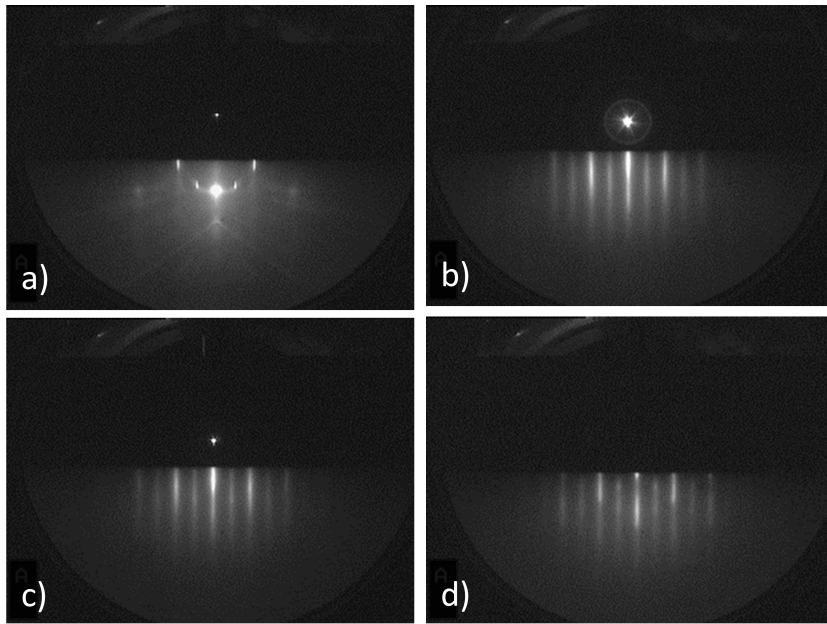


Figure 3.4: RHEED patterns on [001] direction of (a) MgAl_2O_4 substrate for growing epitaxial $\text{Fe}_{3-x}\text{Co}_x\text{O}_4$ thin films with $x = 0$ (b), $x = 0.5$ (c), and $x = 1$ (d).

Figure 3.5 (top panel) shows RHEED patterns (from left to right) of a clean SrTiO_3 (100) substrate (a), and 20 nm $\text{Fe}_{3-x}\text{Co}_x\text{O}_4$ films with $x = 0, 0.1, 0.5$ and 1 (b-e) after the growth on SrTiO_3 substrate. RHEED result of SrTiO_3 substrate shows a streak patterns suggesting the presence of smooth and flat surface after annealing. Since SrTiO_3 substrate has the perovskite structure, it can observe the (10) and $(\bar{1}0)$ diffraction lines in the RHEED pattern. However, once the $\text{Fe}_{3-x}\text{Co}_x\text{O}_4$

films grown on top of SrTiO_3 substrate, the (10) lines of SrTiO_3 substrate change into (20) diffraction lines for $\text{Fe}_{3-x}\text{Co}_x\text{O}_4$ films. Subsequently, the patterns transform into spotty after the films deposition. Based on this evidence, it indicates the tendency of the island terminated growth [33, 67, 68]. Bigger lattice mismatch makes the $\text{Fe}_{3-x}\text{Co}_x\text{O}_4$ films do not grow coherently on SrTiO_3 but still grow epitaxially on it. Some studies report that the $\text{Fe}_{3-x}\text{Co}_x\text{O}_4$ films start relaxing at a critical thickness of 4 nm [67, 68]. Furthermore, LEED results (see Fig. 3.5 bottom panel) confirm this incoherent grow of $\text{Fe}_{3-x}\text{Co}_x\text{O}_4$ on SrTiO_3 substrate. So that perfect LEED patterns can not be obtained since the sample starts to growth in 3D form (island growth).

Based on RHEED and LEED results, the Co atoms with well-tuning concentrations are nicely tailored into $\text{Fe}_{3-x}\text{Co}_x\text{O}_4$ ($x = 0, 0.1, 0.5$ and 1) thin films. The $\text{Fe}_{3-x}\text{Co}_x\text{O}_4$ films show epitaxial growth on MgO , MgAl_2O_4 and SrTiO_3 substrates. They grown coherently on MgO and MgAl_2O_4 substrates but not on SrTiO_3 substrate. Bigger lattice mismatch between the $\text{Fe}_{3-x}\text{Co}_x\text{O}_4$ and the SrTiO_3 substrate allows to Stranski-Krastanov growth mode.

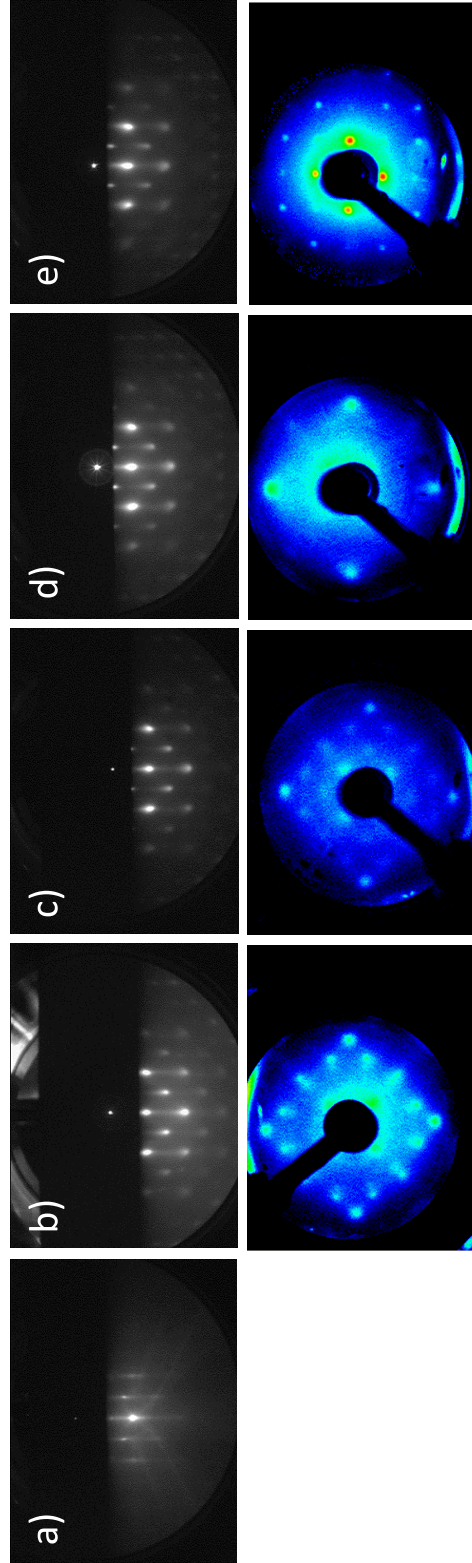


Figure 3.5: Top panel shows RHEED patterns at 20 keV electron energy on [001] direction of (from left to right) (a) SrTiO_3 substrate, Co-substitution in $\text{Fe}_{3-x}\text{Co}_x\text{O}_4$ films with $x = 0$ (b), $x = 0.1$ (c), $x = 0.5$ (d), and $x = 1$ (e). The LEED pattern of the corresponding sample is showed in the bottom panel. The pattern were recorded at electron beam energies of (from left to right) 97, 96, 85, 143 eV,

3.3.2 Ex-situ XRD

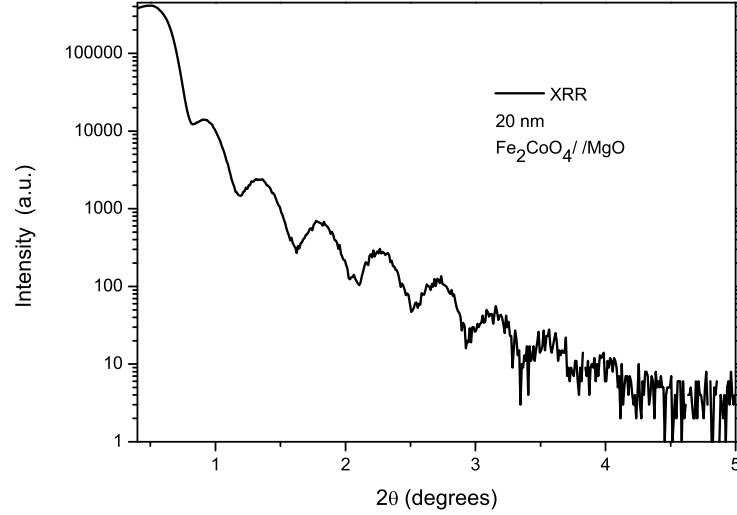


Figure 3.6: XRR measurement of Fe_2CoO_4 grown on cleaved MgO (100) substrate.

Ex-situ XRD measurements have been conducted for further study the strain effect in Fe_2CoO_4 films. It provides quantitative information of the film structure. To simplify the case, the measurements were carried out on 20 nm thick Fe_2CoO_4 films grown on MgO , MgAl_2O_4 and SrTiO_3 substrates. As shown in figure 3.6, the X-ray reflectivity (XRR) measurement confirms the thickness of the films by showing a clear Kiessig oscillation.

Figure 3.7 presents the $\theta - 2\theta$ scans of 20 nm Fe_2CoO_4 film on MgO (100) (a), MgAl_2O_4 (100) (b) and SrTiO_3 (100) (c) substrates. The reflection peaks are broadened due to the finite thickness of the film. The $\theta - 2\theta$ scans of $\text{Fe}_2\text{CoO}_4//\text{MgO}$ show pronounced (002) and (004) diffraction peaks of MgO substrate. In the vicinity of (004) diffraction peak, a weak (008) diffraction peak of Fe_2CoO_4 can be observed, showing that the Fe_2CoO_4 film has the same rocksalt structure as MgO substrate. Same goes with the $\theta - 2\theta$ scans of Fe_2CoO_4 grown on MgAl_2O_4 and SrTiO_3 . Complete sets of diffraction peaks of the substrate can be observed. The (004) and (008) diffraction peaks of Fe_2CoO_4 also appear close to the substrate diffraction peaks (002) and (004). It gives an evidence that the Fe_2CoO_4 film grows with cube-to-cube orientation on MgO , MgAl_2O_4 and SrTiO_3 substrates. However, there are no other peaks corresponding to the other phases.

Detailed look in figure 3.7, the Fe_2CoO_4 diffraction peaks are obtained at higher 2θ values (for $\text{Fe}_2\text{CoO}_4//\text{MgO}$) or lower 2θ values (for $\text{Fe}_2\text{CoO}_4//\text{MgAl}_2\text{O}_4$ and $\text{Fe}_2\text{CoO}_4//\text{SrTiO}_3$) relative to the substrate peaks. It gives an evidence that the c lattice parameter of the films changes depending on the strain induced by the sub-

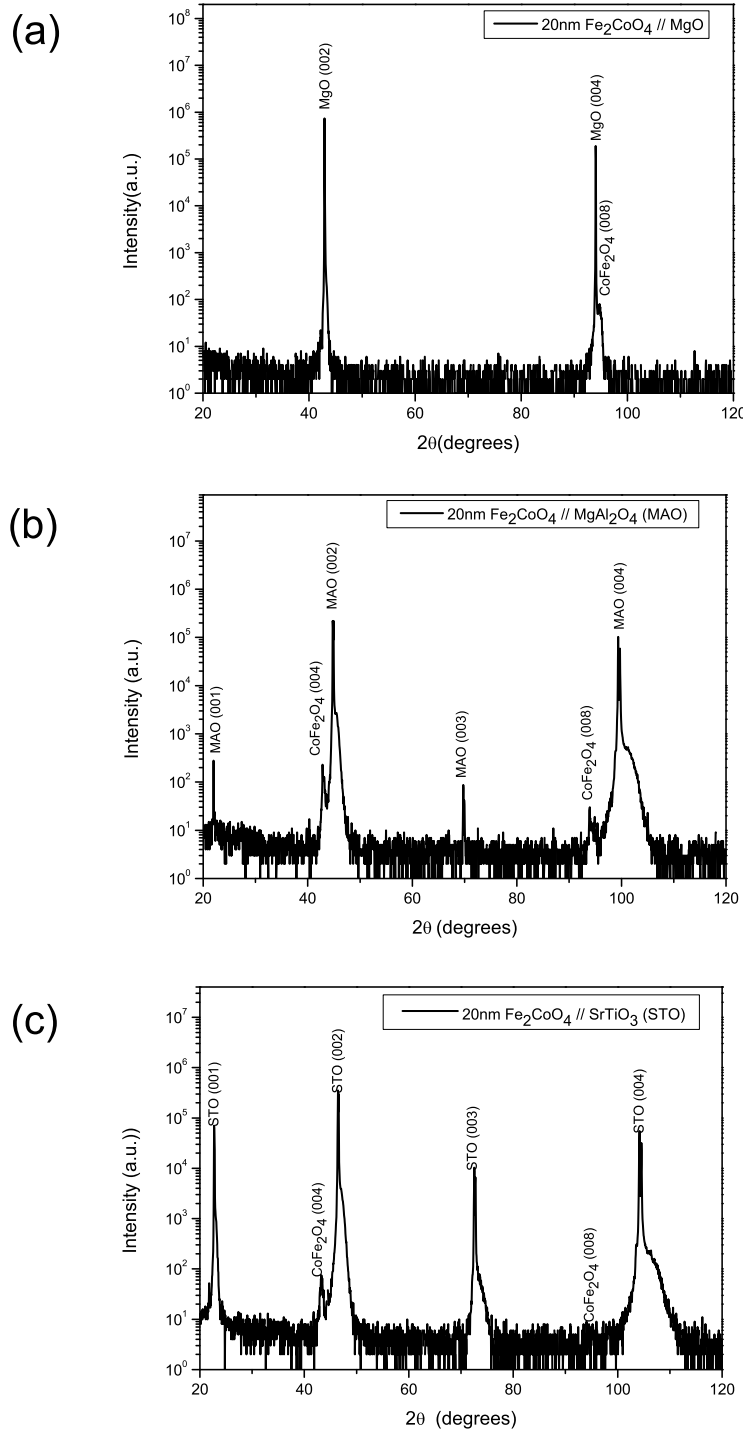


Figure 3.7: 2θ scan of 20 nm thick Fe_2CoO_4 grown on (a) MgO (100), (b) MgAl_2O_4 (100) and (c) SrTiO_3 substrates.

strate. Based on the Poisson effect, the film, which experiences tensile strain, leads to increase in-plane lattice parameter and decrease out-of plane lattice parameter. Since the Fe_2CoO_4 film experiences tensile strain on MgO substrate, the c lattice parameter of Fe_2CoO_4 will decrease, as a consequence the reflection peaks appear at the higher 2θ values. On the other side, the films, which experiences compressive strain, leads to decrease in-plane lattice parameter and increase out-of plane lattice parameter. So does the case for the Fe_2CoO_4 film grown on MgAl_2O_4 and SrTiO_3 substrates, the c lattice parameter of Fe_2CoO_4 should increase, hence the reflection peaks appear at the lower 2θ values.

The Reciprocals Space Maps (RSM) measurement was done to these sample by performing several 2θ scan for increasing values of ω around the non-specular reflection. This measurement provides in-plane $k_{//}$ and out-of plane k_{\perp} components, respectively. From that it can provide the information about the strain state and the strain relaxation. Figure 3.8 shows a two-dimensional map of the reciprocal space of 20 nm Fe_2CoO_4 films on different substrates. In general, there are two features in the picture: the bright one is corresponding to the substrate, while the weaker one at larger k_{\perp} is corresponding to the Fe_2CoO_4 film. Each features has two peaks which is originating from non-monochromatized source. Two major points that can be inferred from the map result. First, if the diffraction peaks of the film are as narrow as those of the substrate, it indicates that the film has well-ordered crystal structure. Second, if the substrate and the Fe_2CoO_4 peaks are at the same $k_{//}$ values, it confirms that the film is fully coherent. Based on this concept, the Fe_2CoO_4 film shows coherent growth on MgO substrate. This result consistent with the former results [61, 62, 69, 70]. Unfortunately, the RSM result for the Fe_2CoO_4 film grown on MgAl_2O_4 substrate was not convincing. But the $\theta - 2\theta$ result on $\text{Fe}_2\text{CoO}_4/\text{MgAl}_2\text{O}_4$ indicates that the out-of-plane lattice parameter is bigger than the bulk value. So that it is difficult to get a clear conclusion to this case. On the other hand, the map result for Fe_2CoO_4 film grown on SrTiO_3 substrate shows relaxed growth [33, 67, 68]. This result supports the RHEED result for Fe_2CoO_4 film grown on SrTiO_3 substrate which shows an island growth mode due to incoherent growth on the substrate.

Lattice parameter	in-plane (a) Å	out-plane (c) Å
Fe_2CoO_4 on MgO	8.42	8.364
Fe_2CoO_4 on MgAl_2O_4	-	8.436
Fe_2CoO_4 on SrTiO_3	8.39	8.356
Bulk Fe_2CoO_4 [38]	8.3765	8.3765

Table 3.2: Lattice parameter from XRD measurement.

The $\theta - 2\theta$ results combine with the Reciprocal space maps data have been

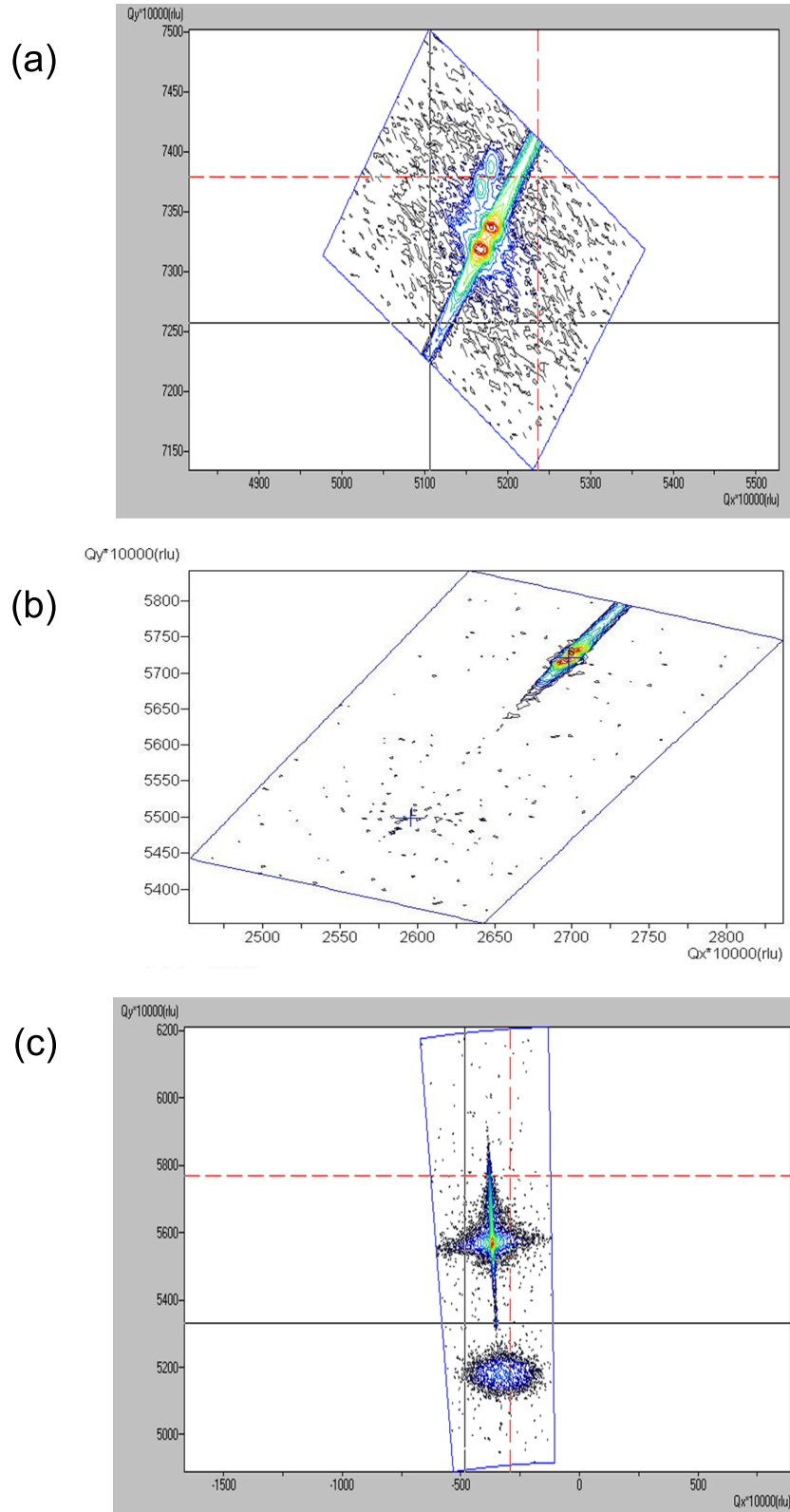


Figure 3.8: Reciprocal space map around the (224) reflection of Fe_2CoO_4 on MgO (100) substrate (a), the (113) reflection of Fe_2CoO_4 on MgAl_2O_4 (100) substrate (b), and the (202) reflection of Fe_2CoO_4 on SrTiO_3 (100) substrate (c).

used to determine the in-plane and out-of-plane lattice parameters and the epitaxial relationship of Fe_2CoO_4 on three different substrates (MgO , MgAl_2O_4 and SrTiO_3). The results are tabulated in table 3.2. Based on this table, the Fe_2CoO_4 film grown on MgO and MgAl_2O_4 substrates have strains consistent to their lattice mismatches, i.e., tensile strain for Fe_2CoO_4 film grown on MgO substrate and compressive strain for Fe_2CoO_4 film grown on MgAl_2O_4 substrate. While the Fe_2CoO_4 film grown on SrTiO_3 substrate has tensile strain even though the lattice mismatch would indicate a preference for compressive strain. This tensile behavior proves that the film has already relaxed, so that it grows in the "bulk" like form. This argument is consistent with RHEED data which shows an island growth mode for Fe_2CoO_4 grown on SrTiO_3 substrate.

X-ray Photoemission study of $\text{Fe}_{3-x}\text{Co}_x\text{O}_4$ Thin Films

4.1 Introduction

The detailed growth of Co-doped in Fe_3O_4 ($\text{Fe}_{3-x}\text{Co}_x\text{O}_4$) thin films has been presented in the previous chapter. Besides, their structural properties have also been verified. In addition, the chemical composition and the electronic structure information of $\text{Fe}_{3-x}\text{Co}_x\text{O}_4$ thin films will be scrutinized in this chapter. Substitution Co atoms into spinel structure may reshuffle the site occupations in the structure. The oxidized Fe may have many possible Fe valencies, i.e., Fe^{2+} or Fe^{3+} . Same goes to Co ion, it may endure Co^{2+} or Co^{3+} valencies in this compound. These ions will reside in two possible sites, i.e., octahedral or tetrahedral. Therefore, X-ray Photoelectron Spectroscopy (XPS) was used to check the chemical composition and the electronic structure of $\text{Fe}_{3-x}\text{Co}_x\text{O}_4$ thin films [71–73].

The presence of strong satellite structure accompanying the main peak is common in the 2p core-level XPS of transition metal compounds [74]. Systematic variations in the positions and intensities of these satellites, depend on the chemical nature of the compound. These imply the important evidence regarding the understanding of the electronic structure. The XPS spectra of iron oxides also exhibit charge transfer satellite structure. These satellite structures, which are very sensitive to the electronic structure of the compounds, are frequently used as fingerprints to identify Fe and Co electronic structure.

This chapter present the XPS study of $\text{Fe}_{3-x}\text{Co}_x\text{O}_4$ thin films grown epitaxially on MgO (100) and SrTiO_3 (100) substrates. The O 1s core level will give the information on the cleanliness of the film's surface since the XPS spectrum are very sensitive to the presence of contaminations such as water and hydrocarbons on the surface. Further study on the chemical composition and the valencies of the ions down to Co-substitution were also provided. Finally, valence band spectra will complete the information on the electronic properties.

4.2 Experiment

$\text{Fe}_{3-x}\text{Co}_x\text{O}_4$ films with 20 nm thick was prepared on MgO (100) and SrTiO_3 (100) substrates for XPS measurements. Detailed growth conditions have been addressed in the previous chapter. After deposition, the samples were immediately transferred from MBE chamber to XPS chamber under UHV conditions. XPS measurement was performed by using monochromatized Al $K\alpha$ radiation ($h\nu = 1486.6$ eV) and Scienta R3000 hemispherical analyzer. The pressure of the XPS chamber during the measurement was 1×10^{-10} mbar while the instrumental resolution measured at the Fermi edge was estimated to be about 0.3 eV with a 100 eV pass energy and a 0.8 mm entrance slit.

In the insulating samples, the XPS spectrum shows a shift (< 2 eV) towards higher binding energy because of a charging effect. The binding energies were corrected by assuming a constant binding energy for the O 1s peak at 530.1 eV [71]. All spectra were normalized to the integrated intensity after background subtraction.

4.3 Results and Discussion

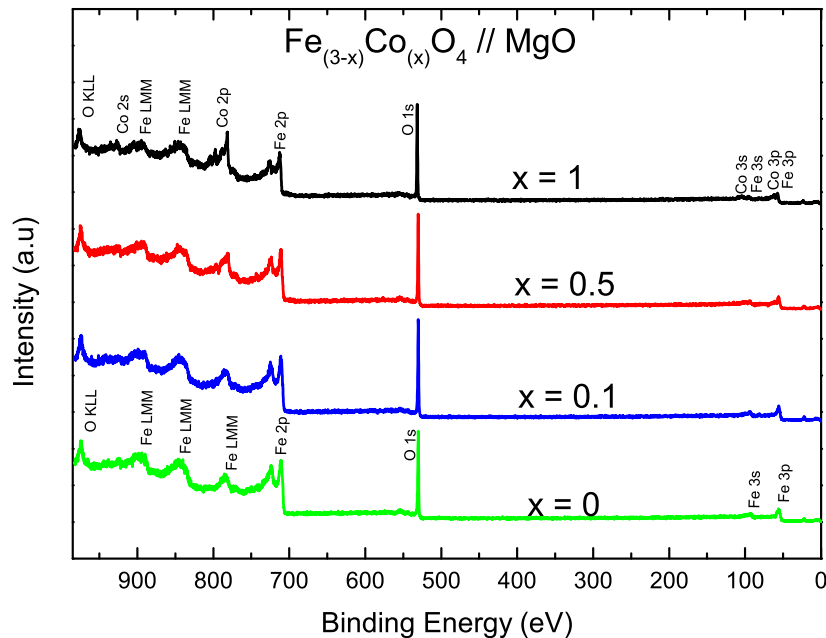


Figure 4.1: XPS wide scan obtained at normal emission for epitaxial $\text{Fe}_{3-x}\text{Co}_x\text{O}_4$ films with $x = 0.1, 0.5, 1$ on MgO (100) (top panel) and reference epitaxial film of Fe_3O_4 on MgO (100).

The general overview of the chemical composition on the sample surface was recorded in the survey scan. Figure 4.1 shows the survey spectrum for $\text{Fe}_{3-x}\text{Co}_x\text{O}_4$ thin films along with the reference spectrum of Fe_3O_4 film. The Fe and O core levels peaks and also its Auger peaks are clearly seen in the Fe_3O_4 survey spectrum. There are extra peaks originating from Co core levels seen in doped samples ($\text{Fe}_{3-x}\text{Co}_x\text{O}_4$). These peaks represent the Co manifestation in $\text{Fe}_{3-x}\text{Co}_x\text{O}_4$ structure. Moreover, there are no other peaks especially C peak in the spectrum. It means that the surfaces are very clean without any contaminants. Detailed scan of the core levels and the valence band were also conducted and will be discussed in the following section.

4.3.1 Core Levels

Before entering to the discussion of core levels spectra, one should remind that Fe_3O_4 is a mixed valence compound with Fe^{3+} residing in octahedral and tetrahedral site, and Fe^{2+} in octahedral site. At room temperature, the octahedral Fe^{3+} and Fe^{2+} ions can formally be written as $\text{Fe}^{2.5+}$. The rapid electron hopping in this site has a frequency of about 10^{-11} sec. However, the core-hole lifetime in the photoemission process is on the order of 10^{-15} sec [75], which is much faster than the hopping frequency. Hence, XPS measurement is a suitable tool for studying the influence of Co-substitution to the ion distribution in $\text{Fe}_{3-x}\text{Co}_x\text{O}_4$ films structure.

Figure 4.2 shows O 1s core level spectra of $\text{Fe}_{3-x}\text{Co}_x\text{O}_4$ thin films grown on MgO (100) substrate (top panel) and SrTiO_3 (100) substrate (bottom panel). The spectra look similar to the results reported by Chambers *et al.* [66]. All of the O1s core level spectra of $\text{Fe}_{3-x}\text{Co}_x\text{O}_4$ films show a single peak which indicates the presence of single anion site in the lattice. Detailed look on the spectra reveals a slightly variation on the line shape. There is an asymmetric shape at higher binding energy in Fe_3O_4 spectra. This asymmetric shape reduces with the increasing of Co substitution concentrations. Since Fe_3O_4 is a bad metal at room temperature, one could purpose that this behavior originates from the Doniach-Sunjic asymmetry shown in metals [76]. This physical phenomenon is attributed to the presence of electron-hole pair excitations upon creating of the core hole, i.e., screening of the core hole by conduction-band electrons. Since Co-substitution reduces the conductivity of the samples [22], the more insulating character of the compound could explain the progressive change to a more symmetric shape of the XPS speaks. All in all, the single-peak shape without low-intensity side band proves the cleanliness of the surfaces.

Figure 4.3 shows a series of Fe 2p core level spectra of $\text{Fe}_{3-x}\text{Co}_x\text{O}_4$ thin films as a function of Co substitution. The top panel corresponds to the films grown on MgO substrate, while the bottom one shows the films grown on SrTiO_3 substrate. The spin orbit coupling mainly splits Fe 2p spectrum into two parts, namely Fe $2p_{3/2}$ at

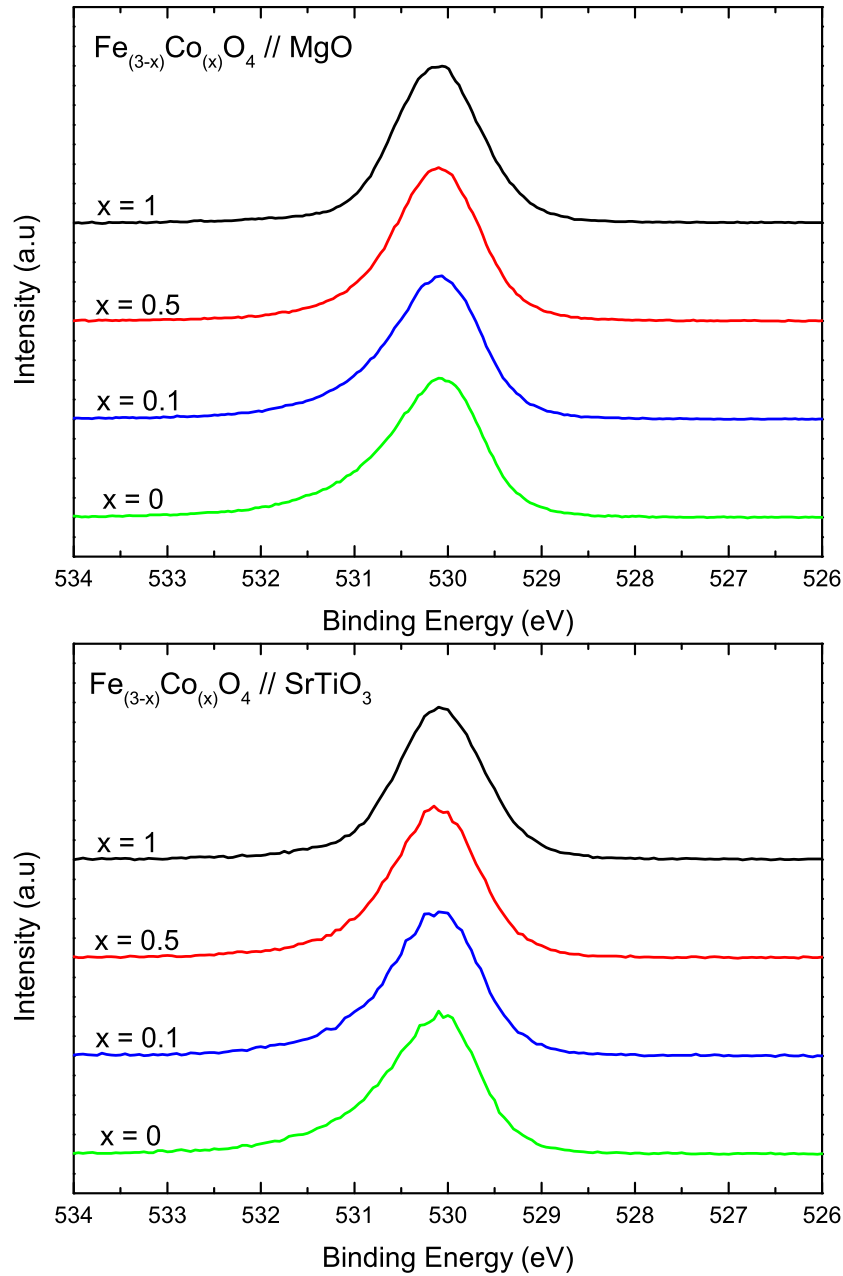


Figure 4.2: XPS O 1s core-level spectra obtained at normal emission for epitaxial $\text{Fe}_{3-x}\text{Co}_x\text{O}_4$ films with $x = 0, 0.1, 0.5, 1$ on MgO (100) (top panel) and SrTiO_3 (100) (bottom panel).

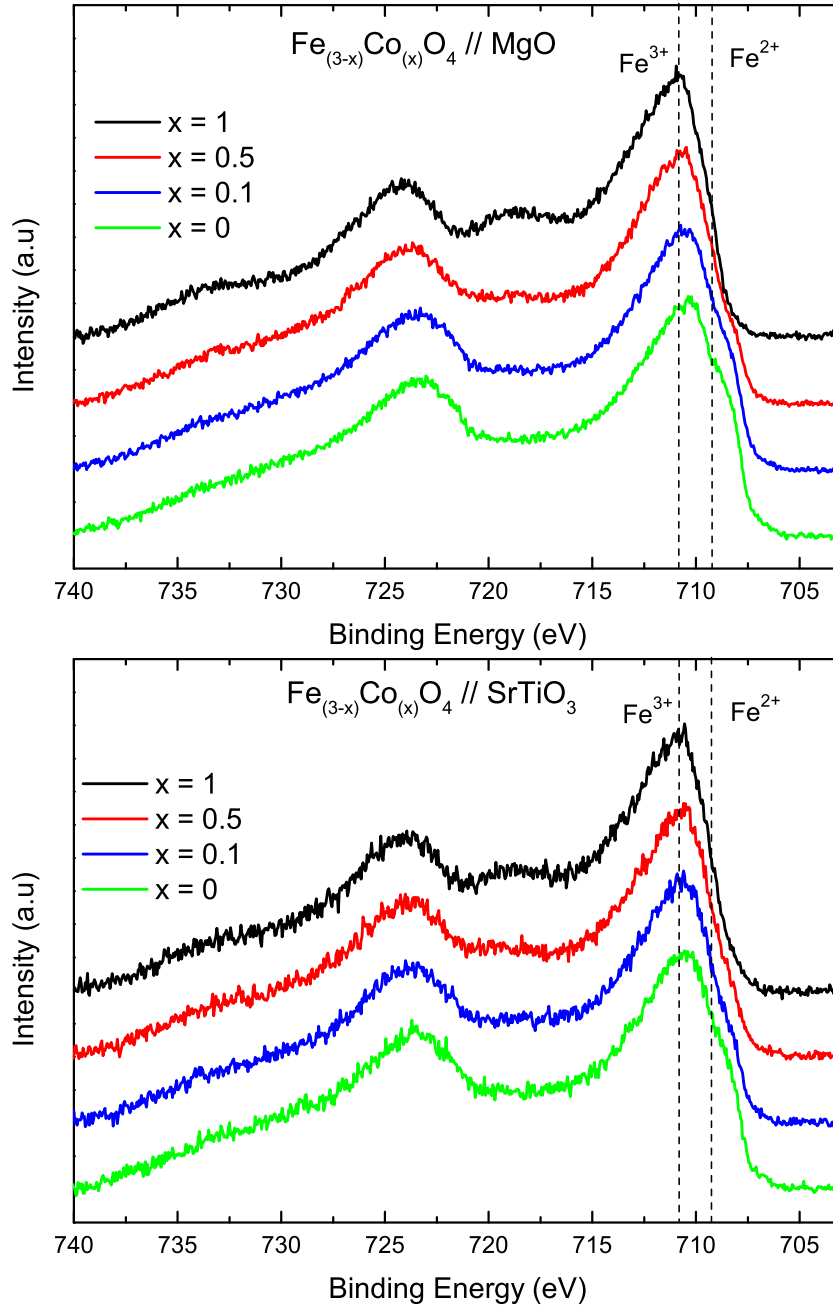


Figure 4.3: XPS Fe 2p core-level spectra obtained at normal emission for epitaxial $\text{Fe}_{3-x}\text{Co}_x\text{O}_4$ films with $x = 0, 0.1, 0.5, 1$ on MgO (100) (top panel) and SrTiO_3 (100) (bottom panel).

710.22 eV and Fe $2p_{1/2}$ at 723.32 eV. Barely look on these spectra, the changing of Fe $2p_{3/2}$ peak width which is getting smaller with the increasing Co-substitution. It is because of the reduction a shoulder-peak at 709.22 eV. This main-peak shoulder at 709.22 eV is a fingerprint of Fe^{2+} ions in the structure.

Upon increasing the Co-substitution concentrations, the Fe $2p_{3/2}$ and $2p_{1/2}$ main peaks slowly move to higher binding energy (at 710.8 eV and 724.20 eV for Fe_2CoO_4 samples) and follow with the appearance of satellite peaks at 719 eV and 733.15 eV. These satellite peaks are the fingerprint for the charge transfer satellites of Fe^{3+} ions. These features are more pronounced on Fe_2CoO_4 spectra. From these evidences, it confirms that the introduced Co-ions replace the Fe^{2+} in octahedral site. So that the Fe_2CoO_4 film only remains with the Fe^{3+} ions distributed in octahedral and tetrahedral sites. In addition, the Fe 2p core level spectra of Fe_2CoO_4 thin film looks similar to the Fe 2p spectra of $\gamma\text{-Fe}_2\text{O}_3$ which has spinel structure constituted by Fe^{3+} in octahedral and tetrahedral sites [74].

There is an absent of the charge transfer satellites in the Fe 2p core level spectra of Fe_3O_4 thin films. Typically, because of the charge transfer interaction between the ligand 2p orbitals and the transition metal, the main peak of the 2p core level spectrum is followed by higher-energy states, comprising the satellite structures [77]. It is confirmed from the cluster calculation of Fe 2p on Fe_3O_4 done by Fujii *et al.* [74]. From this calculation results, both Fe^{2+} and Fe^{3+} ions have charge transfer satellites. Since Fe_3O_4 has two possible valencies in two different sites, the sum up of these three spectra results is only two main peaks without any indication of satellites.

Figure 4.4 shows a series of Co 2p core level spectra of $\text{Fe}_{3-x}\text{Co}_x\text{O}_4$ thin films grown on MgO (100) substrate (top panel) and SrTiO_3 (100) substrate (bottom panel). Both figures show similar trend. Generally in the Co 2p core-hole spectra, the spin-orbit coupling splits the spectrum roughly into two main peaks at ~ 780.05 eV for Co $2p_{3/2}$ and ~ 796.00 eV for Co $2p_{1/2}$. Both main peaks are followed by the charge transfer satellites at ~ 786.45 eV and ~ 802.65 eV.

The Co 2p line shape is changing dramatically during increasing the Co-substitution concentrations as shown in figure 4.4. Especially for low doped ($x = 0.1$) spectra, it has different line shape compared to full doped ($x = 1$) spectra. The maximum peak is also shifted to the lower binding energy at around ~ 782.5 eV. It is noted that the Co 2p core level overlap with the Fe Auger peak at 784 eV (see figure 4.1). Therefore, in this case, the Co 2p spectra consist of two spectra, i.e., Fe Auger and Co 2p core level. Increasing the Co-substitution concentrations, the spectra gain more spectral weight from Co 2p core level rather than Fe Auger. As a result, the Fe_2CoO_4 spectrum has a clear Co 2p line shape compared to the others.

In order to find out which valence state Co ions have in $\text{Fe}_{3-x}\text{Co}_x\text{O}_4$ films, CoO spectra were used as a reference for Co^{2+} spectra. By looking at the Co 2p core level spectra in figure 4.5, the $\text{Fe}_{3-x}\text{Co}_x\text{O}_4$ spectra have similar line shape with

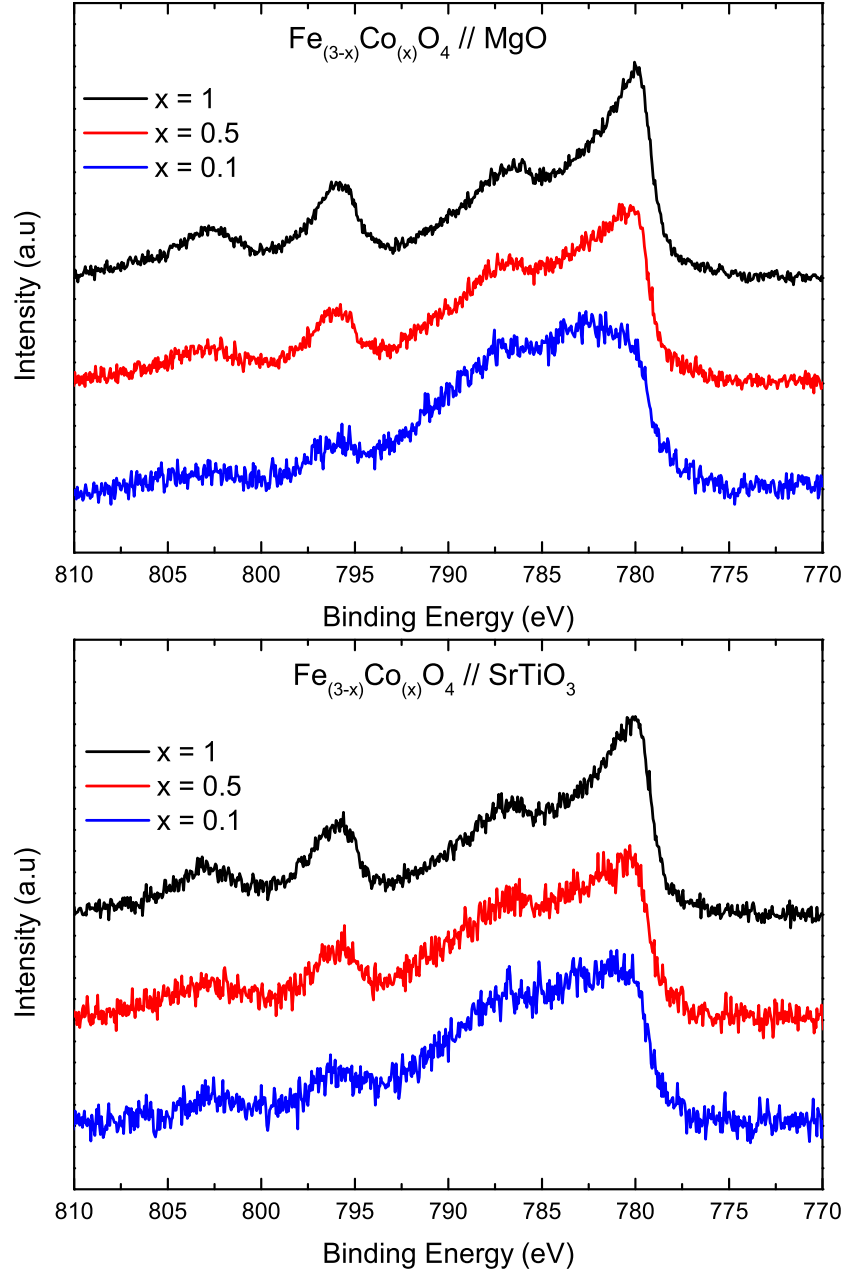


Figure 4.4: XPS Co 2p core-level spectra obtained at normal emission for epitaxial $\text{Fe}_{3-x}\text{Co}_x\text{O}_4$ films with $x = 0, 0.1, 0.5, 1$ on MgO (100) (top panel) and SrTiO_3 (100) (bottom panel).

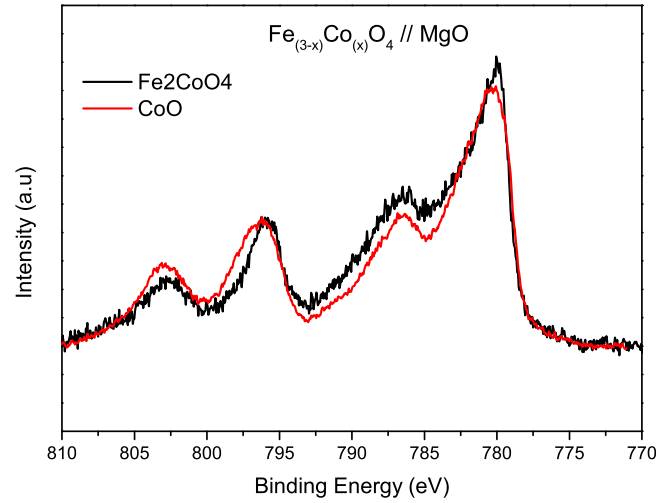


Figure 4.5: Comparison Co 2p core-level spectra obtained at normal emission for epitaxial Fe_2CoO_4 on MgO (100) and bulk single-crystal CoO.

the CoO spectra. It confirms that the Co ion has 2+ valency with high spin state character in $\text{Fe}_{3-x}\text{Co}_x\text{O}_4$ thin films.

Based on the core levels spectra of $\text{Fe}_{3-x}\text{Co}_x\text{O}_4$ thin films, one can say that the Fe^{2+} , Fe^{3+} and Co^{2+} cations are in the high spin states. It is expected that the 2p core level line shape will be broadened by unresolved multiplet splitting [71]. The Fe2p and Co2p core levels spectra of $\text{Fe}_{3-x}\text{Co}_x\text{O}_4$ thin films show strong charge transfer satellites. It has been confirmed by Frost *et al.* [78] that high spin states of transition metal ions have strong charge transfer satellites; whereas low spin states have weak zero satellite structure.

4.3.2 Valence band

The XPS valence band spectrum of $\text{Fe}_{3-x}\text{Co}_x\text{O}_4$ thin films grown on MgO (100) and SrTiO_3 (100) substrates are shown in figure 4.6 and 4.7. The spectrum consists of the main band (at 0-10 eV) and O 2s level (at 21.5 eV). Looking at the spectral weight around the Fermi energy (E_F), they are decreasing systematically as the increasing Co-substitution concentrations. The most remarkable feature in the spectra is the reduction of the peak intensity around 0.5 eV. This peak corresponds to the removal of a minority down-spin electron of Fe^{2+} t_{2g} orbital at octahedral site reaching the ${}^6\text{A}_{1g}$ final state of the d^5 configuration [79]. This assignment is to be compared with the band structure prediction by Anisimov [80]. Decreasing of the electrical conductivity is mainly originated from the reduction of the spin-down state in t_{2g} orbital of Fe ions at octahedral site because of Co^{2+} substitution.

According to the explanation suggested by Takaobushi *et al.* [20], the changing

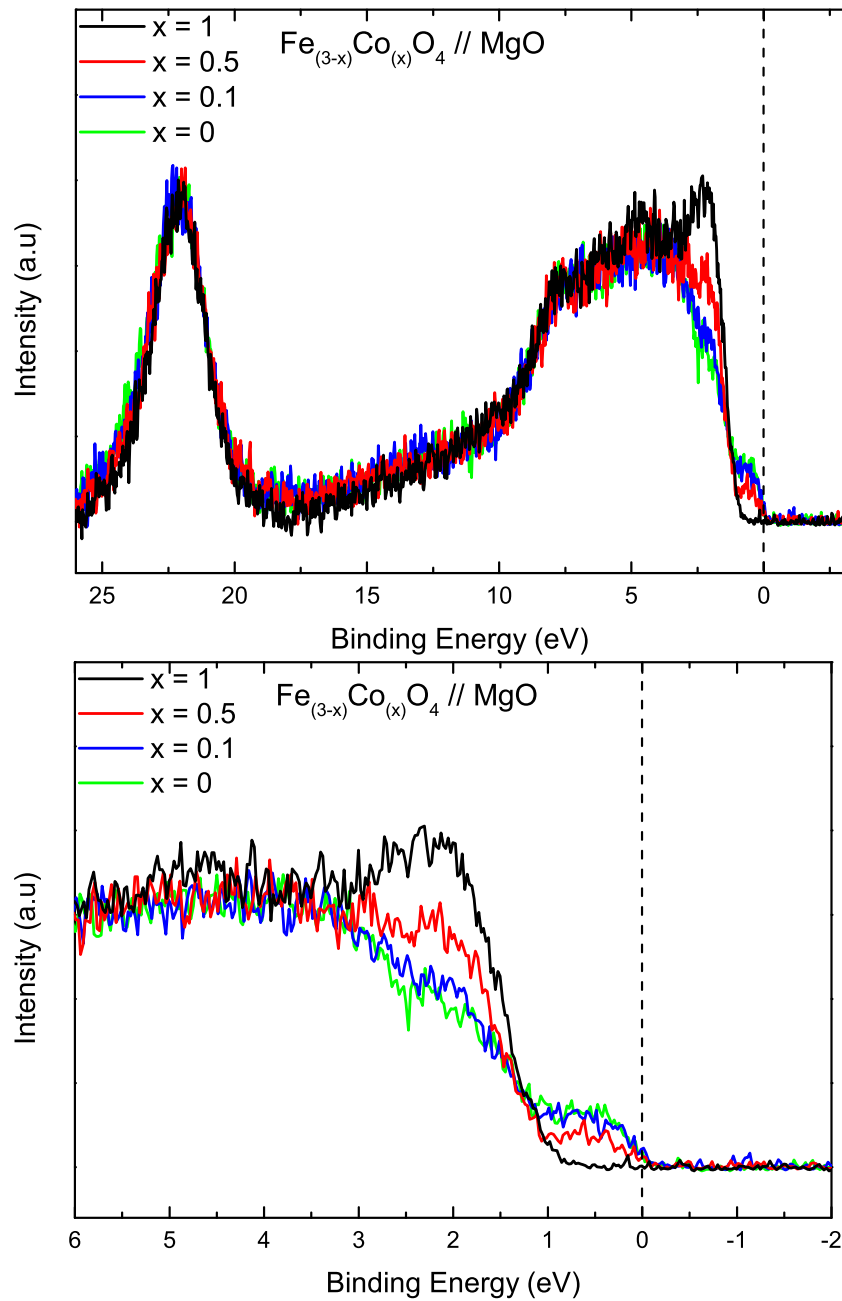


Figure 4.6: XPS valence band spectra obtained at normal emission for epitaxial $\text{Fe}_{3-x}\text{Co}_x\text{O}_4$ films with $x = 0, 0.1, 0.5, 1$ on MgO (100) (top panel) and a zoom in the Fermi cut (bottom panel).

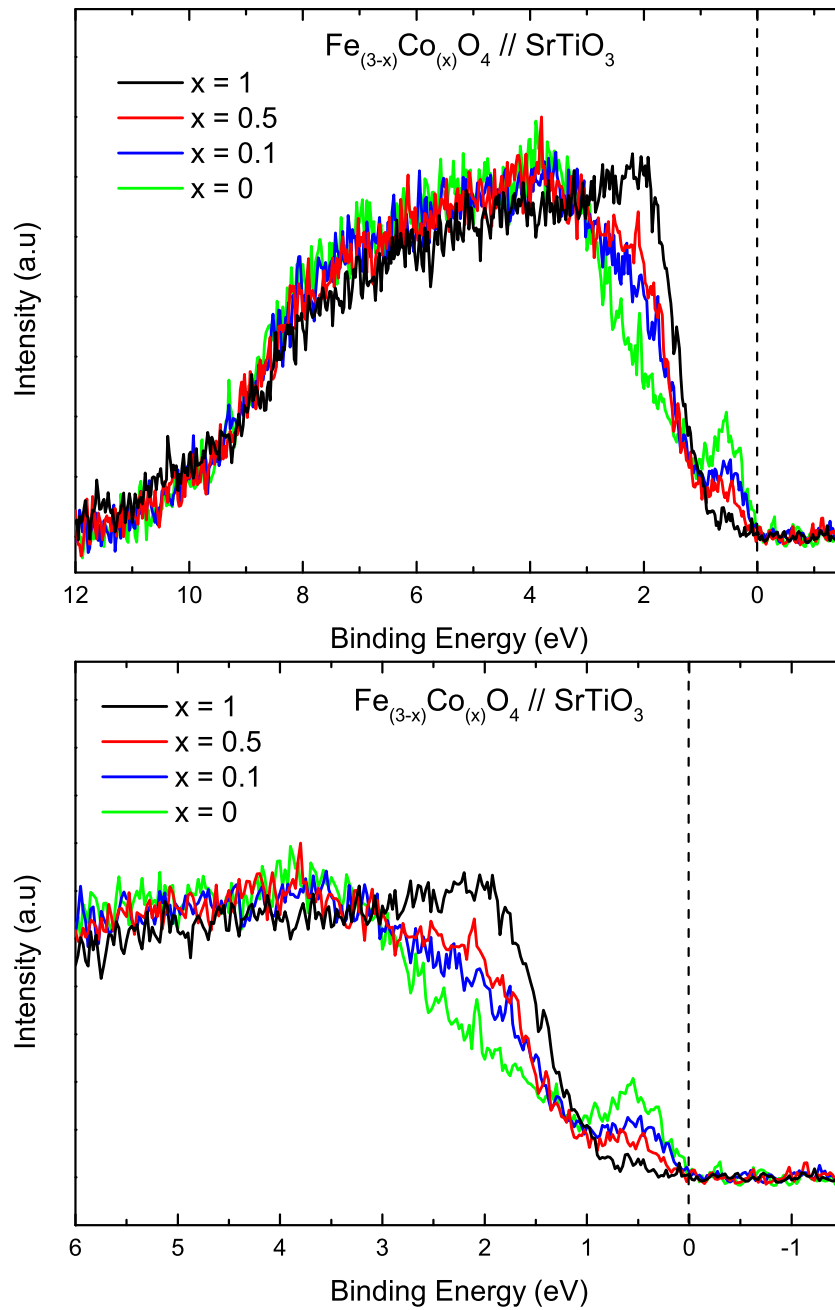


Figure 4.7: XPS valence band spectra obtained at normal emission for epitaxial $\text{Fe}_{3-x}\text{Co}_x\text{O}_4$ films with $x = 0, 0.1, 0.5, 1$ on SrTiO_3 (100) (top panel) and a zoom in the Fermi cut (bottom panel).

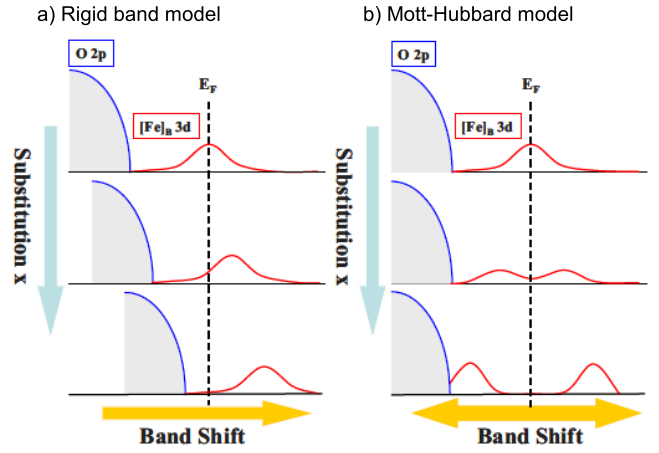


Figure 4.8: Schematic illustration of valance band evolution by Co-substitution. a) Rigid band model. b) Mott- Hubbard model. For simplicity, only O 2p and Fe 3d at the octahedral site are shown. DOS at the tetrahedral site were omitted. This figure is retrieved from Ref. [20].

of spectra weight around E_F proves the hypothesis of the correlated electron effects in this compound. If $\text{Fe}_{3-x}\text{Co}_x\text{O}_4$ system is a conventional semiconductor band gap, decreasing the carrier concentration would cause a chemical potential shifting on the basis of the rigid band model. However, core level spectra of O 1s, Fe 2p, and Co 2p did not shift against E_F . One therefore can conclude that the Co substituted Fe_3O_4 is not an ordinary semiconductor that gets doped. Takaobushi *et al.* proposed that this phenomenon can be explained by the Mott-Hubbard model as shown in figure 4.8 [20]. This model is utilized to explain the spectra change as following: (i) substituting Co^{2+} decrease the Fe^{2+} to Fe^{3+} ratio, (ii) the electron-electron correlation (effective Coulomb interaction) increases with decreasing screening effect due to the reduction of carrier concentration, (iii) consequently, the gap becomes larger and the peak shifts to the higher binding energy side, and finally, (iv) the Mott gap is formed at the $x=1$ component (Fe_2CoO_4). However, when comparing the experimental data as shown in figures 4.6 and 4.7 with panel b of figure 4.8, we must conclude that also the picture of Takaobushi *et al* is not applicable. The experimental spectra show that Co substitution results in a decrease/disappearance of the ${}^6\text{A}_{1g}$ peak at 0.5 eV binding energy and in a concomitant appearance/increase of a new feature at 2 eV binding energy. By viewing Fe_3O_4 as a 50% doped Mott-Insulator that becomes semiconducting at low temperatures due to the Wigner crystallization of polarons, we infer that the replacement of the Fe^{2+} ions by Co^{2+} introduces effectively impurity potentials that makes the polarons more deeply bound and thus increases the semiconducting gap.

Initial study of sites occupation on $\text{Fe}_{3-x}\text{Co}_x\text{O}_4$ films by X-ray Absorption (XAS)

5.1 Introduction

Photoemission study of Fe_3O_4 confirms that it is a bad metal at room temperature [79]. This conductivity behavior can be modified by introducing substitution agent such as Co atom into Fe_3O_4 compound ($\text{Fe}_{3-x}\text{Co}_x\text{O}_4$) [22]. Therefore, it is highly desired to determine the electronic structure of $\text{Fe}_{3-x}\text{Co}_x\text{O}_4$ experimentally. However, there is no direct approach to this system because of the simultaneous presence of Fe^{2+} and Fe^{3+} valences as well as octahedral and tetrahedral sites. Furthermore, a standard electron spectroscopic method yields rather broad spectral line shape. In addition, featureless spectroscopy spectra require precise analysis about the details of the localized structure of the ions, the effective crystal field and the cation distribution in the structure.

The XPS study has been done to reveal the electronic structure of $\text{Fe}_{3-x}\text{Co}_x\text{O}_4$ thin films. In addition to XPS results, the XAS measurement has been done and will be discussed in this chapter. The XPS measurement probes the occupied core-level density of states, while the XAS measurement probes both the empty valence-band density of states and the occupied core-level density of states. Due to its site and symmetry selective character, the $L_{2,3}$ XAS of transition metal is a powerful tool to study the electronic structure of transition-metal oxides [55, 64, 81].

The XAS measurement can be analyzed qualitatively to obtain the information of site occupancies for different cation valence states. The site occupation of $\text{Fe}_{3-x}\text{Co}_x\text{O}_4$ for different Co-concentration is qualitatively figured out in this chapter. The study of the cations (Fe^{2+} , Fe^{3+} and Co^{2+}) distribution in two different sites (octahedral and tetrahedral) is verified upon substitution the Fe_3O_4 with Co atoms. Further, the site occupancy for different thickness is discussed to have some information of the growth process in Fe_3O_4 and Fe_2CoO_4 films.

5.2 Experiment

For the substitution dependent study, 20 nm thick $\text{Fe}_{3-x}\text{Co}_x\text{O}_4$ with nominal concentration $x = 0, 0.1, 0.5$ and 1 on MgO (100) substrate were prepared. Additionally, thinner Fe_3O_4 and Fe_2CoO_4 films with the thickness of 5 ML and 20 ML were also prepared for the thickness dependent study. Detailed growth description can be found in chapter 3. All samples were capped with a 10 ML MgO film to protect the surface of the films from further oxidation after removal from the UHV system.

The XAS measurement was performed at the Dragon beam line of the National Synchrotron Radiation Research Center (NSRRC) in Taiwan. The photon energy resolution was 0.35 eV for Co $L_{2,3}$ edges and 0.3 eV for Fe $L_{2,3}$ edges. The spectra were recorded using the total electron yield method (TEY). The TEY method is chosen as it is less susceptible to saturation effects and other distortions presented in the fluorescence yield (FY). The CoO and Fe_2O_3 single crystals were measured simultaneously in separate chambers to calibrate the photon energy. The measured spectra were normalized to the average spectral intensity in the energy range of 700-730 eV for Fe $L_{2,3}$ and of 770-805 eV for Co $L_{2,3}$ respectively, after the subtraction of the pre-edge background (approximated by a linear fit) in order to enable one to directly compare the difference between spectra to spectra.

5.3 Results

The typical XAS spectrum of transition metal at the $L_{2,3}$ edges has two well-separated parts due to 2p core-hole spin-orbit coupling. They are the L_3 edge with a photon energy of around 710 eV (780 eV) for the Fe (Co) ion and the associated L_2 edge with a photon energy of around 722 eV (795 eV). The line shape of each edge is strongly dependent on the multiplet structure, mainly established by the atomic like 3d-3d and 2p-3d Coulomb and the exchange interaction, as well as by the local crystal field and the hybridization with the O 2p ligands. It is a unique character for a certain valency and site symmetry.

Figure 5.1 (top curve) shows the experimental Fe $L_{2,3}$ XAS spectrum of 20 nm Fe_3O_4 film on MgO (100) at room temperature. It is clearly seen that there are two regions of peaks, namely the Fe L_3 edge which exists at 705-712 eV and its counterpart, the Fe L_2 edge, which exists at 717-724 eV. A completely distinct spectral line shape between the L_3 and L_2 edges implicitly indicates that the electron-electron and the core-hole electron interactions due to spectroscopic processes cannot be neglected. As a reference, the XAS spectrum of bulk Fe_3O_4 crystal is also depicted in the middle curve. Here one can directly notice that except for a little discrepancy below the main L_3 peak (i.e., a small hump at ca. 707.6 eV), the similarity between both spectra is reasonably compelling, suggesting that the overall stoichiometry of

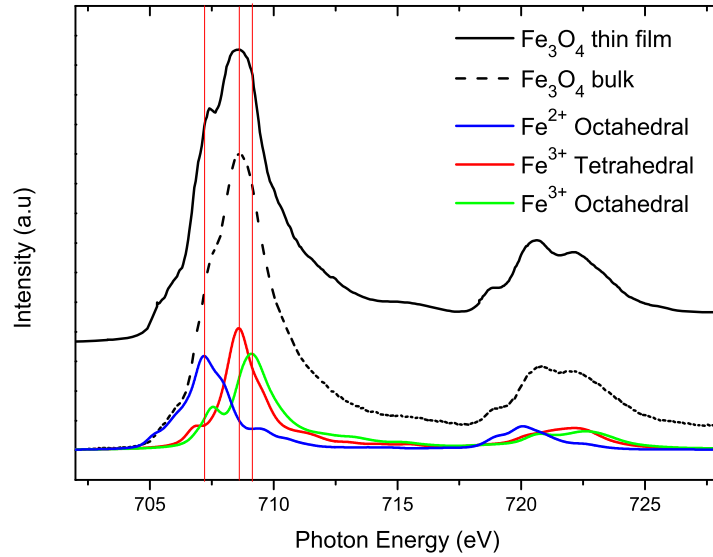


Figure 5.1: (Top curve) Experimental Fe $L_{2,3}$ XAS spectrum of 20 nm Fe_3O_4 thin film on MgO (100). (Middle curve) Experimental Fe $L_{2,3}$ XAS spectrum of bulk Fe_3O_4 . (Bottom curves with color line) Three calculated spectra for different valency and local symmetry of Fe ions [64].

the film is retained even after deposition of the MgO overlayer.

It is well known that in Fe_3O_4 , Fe^{2+} ions are only coordinated in the octahedral symmetry, while Fe^{3+} ions are split between the tetrahedral and the octahedral sites. The calculated XAS spectra for each Fe ion components based on the configuration interaction cluster model reported by Chang [64] are displayed in the bottom curves of the figure 5.1. There are some important features on each of the calculated spectra that are directly linked to the line shape of the experimental spectra. The contribution of the Fe^{2+} is obviously seen at the lower energy side of the main L_3 peak where the energy position of the Fe^{2+} peak matches with either the shoulder of the bulk Fe_3O_4 or the small hump of the Fe_3O_4 film. More importantly, the existence of the spectral foot at the leading edge of both the L_3 and L_2 regions is associated with the presence of Fe^{2+} ion. This is a key signature to determine whether or not a ferrite film contains Fe^{2+} ion with the octahedrally coordinated site. Furthermore, the main peak L_3 edge is dominated by Fe^{3+} in the tetrahedral site while its counterpart in the octahedral site governs the high energy side of the main L_3 peak. Although the energy separation between these Fe^{3+} peaks is small, their spectral structure in the L_3 region are different, specifically the pre-peak of the L_3 in the octahedral site is more pronounced. In other words, the intensity ratio

between the pre-peak and the main peak of the octahedral Fe^{3+} site is higher than that of the tetrahedral Fe^{3+} . This note is also corroborated by the fact that in the L_2 region the Fe^{3+} octahedral site has double peaks, whereas the Fe^{3+} tetrahedral site exhibits only one broad peak. All of these highlighted characteristics will be used for our qualitative XAS analysis in the following section.

5.3.1 Substitution dependence

The experimental Fe $L_{2,3}$ XAS spectra of the 20nm thick $\text{Fe}_{3-x}\text{Co}_x\text{O}_4$ samples with different Co substitution composition x are displayed in figure 5.2. It is clearly seen that the spectral line shape alters as the Co concentration varies, implying that the proportion of the site occupation of Fe ions in the Co-doped film gradually change from that in the undoped one. Here, it notes three important features at each edge that are used for the following substitution dependence analysis. In the L_3 region, the lower energy shoulder is labeled as feature A; the pre-peak as feature B; and the main peak as feature C. Similarly in the L_2 region, the lower energy shoulder of the L_2 edge is labeled as feature D; the lower- and higher-energy L_2 peaks are labeled as feature E and F, respectively. The spectrum of the undoped Fe_3O_4 film (green line) is re-plotted from figure 5.1 and it has been discussed in the previous section. By introducing 3.3% Co concentration into the $\text{Fe}_{3-x}\text{Co}_x\text{O}_4$ sample ($x = 0.1$, $\text{Fe}_{2.9}\text{Co}_{0.1}\text{O}_4$), the spectral weight with the feature A, B, D and E diminishes, while that with the feature C and F slightly increases. A similar trend also occur when Co concentration is added up to 16.25% ($x = 0.5$, $\text{Fe}_{2.5}\text{Co}_{0.5}\text{O}_4$) and even to 33% ($x = 1$, Fe_2CoO_4), namely the decrease of the pre-peak (feature B) and the increase of the main peak (feature C) of the L_3 edge as well as the decrease of the feature E and the increase of the feature F of the L_2 edge. Furthermore, it is noted that for the Co concentration of 33%, the spectral weight A and D completely vanish. This is obviously not observed at the lower Co substitution composition.

Referring to the calculated spectra in figure 5.1, the reduction of spectra weight in the L_3 and L_2 regions (feature A, B, D, and E) with increasing Co concentration is attributed mainly to a decrement of the Fe^{2+} cation in the octahedral site. With the reduction of the octahedral Fe^{2+} content, it naturally leads to another consequence, namely the increasing percentage of both Fe^{3+} components with respect to the total number of Fe cations per formula unit. In the figure 5.2, one can clearly see that the intensity of the main peak with the feature C gradually intensifies and its peak position is slightly shifted to the higher energy as the Co concentration increases. It implies that the spectra are predominantly governed by both Fe^{3+} in the tetrahedral and octahedral sites. One might tend to think that the shift of the main L_3 peak to the higher energy is related to the relative deficiency of the tetrahedral Fe^{3+} site to its octahedral counterpart, yet, the present analysis cannot differentiate whether or not both Fe^{3+} sites have an unequal weight. For the Fe_2CoO_4 case, it is certain

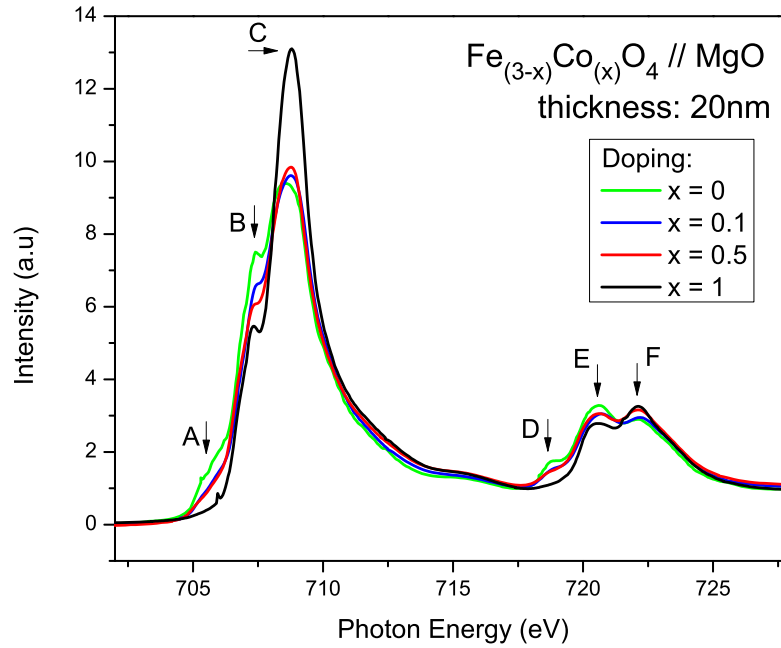


Figure 5.2: (Top part) Experimental Fe $L_{2,3}$ XAS spectra of $\text{Fe}_{3-x}\text{Co}_x\text{O}_4$ ($x = 0, 0.1, 0.5, 1$) on MgO (100) for different Co substitution concentration.

that the Fe^{2+} ions in the octahedral sites are completely missing and they are fully replaced by Co dopant ions. Basically, it supports the XPS results outlined in the previous chapter and confirms the earlier published work by Moyer *et al.* [22].

The corresponding Co $L_{2,3}$ XAS spectra of the 20nm thick $\text{Fe}_{3-x}\text{Co}_x\text{O}_4$ are plotted in figure 5.3. The Co L_3 edge is characterized by three sharp peaks: the low energy pre-peak at 777.75 eV (marked as A), the two main peaks at 779.25 eV (marked as B) and 780.25 eV (marked as C), and the shoulder at the high-energy end marked as D. Moreover, the Co L_2 edge has less structure which only a single broad peak can be clearly seen at 794.5 eV (marked as E). Note that it was quite difficult to align the spectra, especially for the films with lower Co concentrations, since the pre-edge background and the post edge jump deviate quite a lot and have a different slope. At the present moment, one possible is that the smaller Co-substitution makes the Fe $L_{2,3}$ edge gain more intensity. Therefore it is very small intensity contribution for Co $L_{2,3}$ edge compare to Fe $L_{2,3}$ edge. As a consequence, the determination of Co concentration for the lower x with respect to the Fe_2CoO_4 would be unreliable; therefore an attempt to calculate the actual Co stoichiometry in comparison to the nominal one was not carried out.

Broadly speaking, all the Co $L_{2,3}$ XAS spectra in figure 5.3 have a similar line shape. They look identical to the XAS spectrum of the CoO, the work that was reported by Csiszar *et al.* [34]. It is reckoned as a reference for a divalent Co ion

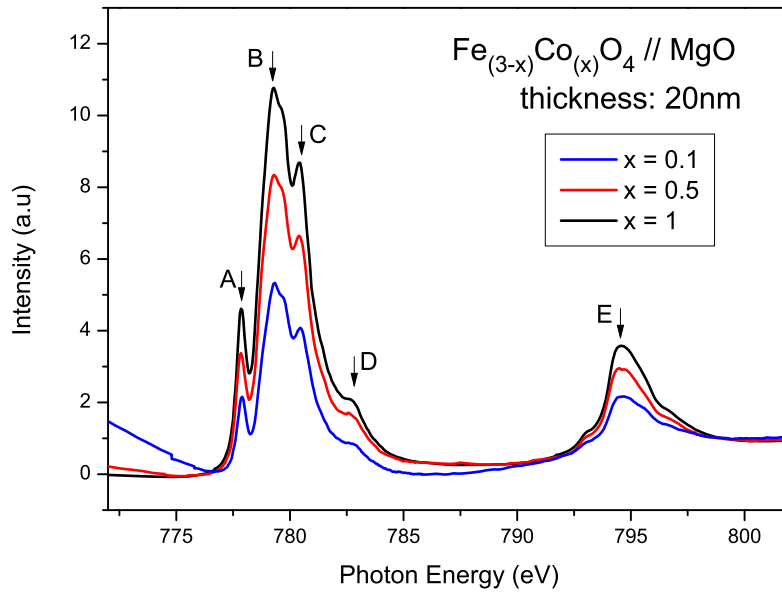


Figure 5.3: Experimental Co $L_{2,3}$ XAS spectra of 20 nm $\text{Fe}_{3-x}\text{Co}_x\text{O}_4$ $x = 0, 0.1, 0.5, 1$ on MgO (100) substrate.

with the octahedral symmetry. A closer look at the figure 5.3, one can yet notice some differences as follows. The intensity ratio of the feature C to B of the L_3 peak is not as high as that of the pristine CoO, or in other words, the intensity dip between feature B and C is not as striking as that of the CoO. Moreover, the L_2 peak (feature E) looks a bit sharper. All of these characteristics may indicate that the Co^{2+} may also coexist in the tetrahedral sites [82]. However, as Moyer *et al.* pointed out, their existence in an average number per formula unit is less than 0.1 for the range of the Co concentration between $0 < x \leq 1$ [22]. Therefore, the most important information that can be drawn from all the Co $L_{2,3}$ XAS spectra (figure 5.3) is that there is no indication of higher valency (Co^{3+}). If there is any of this, the contribution is very negligible [22, 60]. In conclusion, substitution Co in $\text{Fe}_{3-x}\text{Co}_x\text{O}_4$ compounds mainly replaces the octahedral Fe^{2+} ion and the Co dopant is notably divalent where its preferential site is in the octahedral site.

5.3.2 Thickness dependence

Having shown the role of the Co dopant as well as its valency and site preference in the thick $\text{Fe}_{3-x}\text{Co}_x\text{O}_4$ films, now the investigation of the cation distribution in the thinner films, namely 5 monolayers (ML) and 20 ML thick, will be carried out. By making use of the Fe $L_{2,3}$ XAS spectra, the sites occupation of all cations at the initial stage of growth will be qualitatively analyzed. To simplify the case, it will only explore the thickness dependent films for $x = 0$ (Fe_3O_4) and $x = 1$ (Fe_2CoO_4).

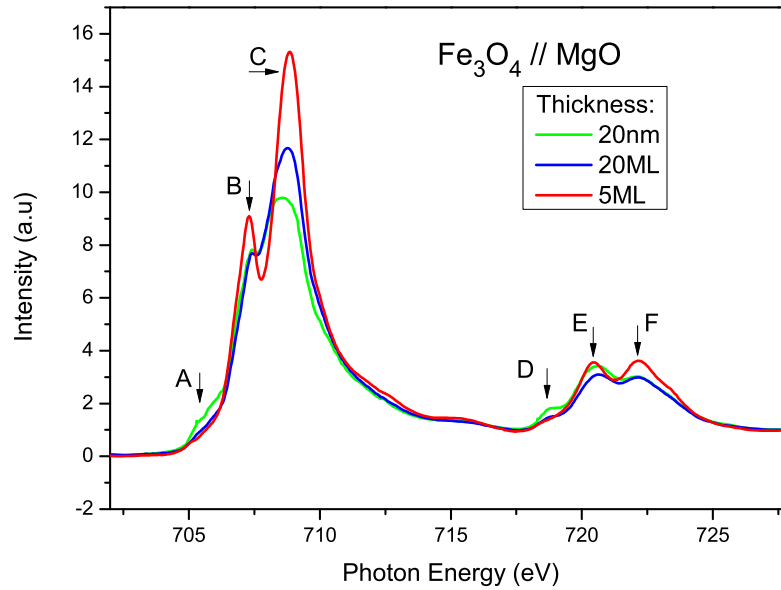


Figure 5.4: Thickness dependent Fe $L_{2,3}$ XAS spectra of Fe_3O_4 films.

All other Co concentrations are excluded in this section.

Figure 5.4 shows the Fe $L_{2,3}$ XAS spectra of Fe_3O_4 films with the thickness of 5 ML and 20 ML on MgO substrate. As a reference, the XAS spectrum of 20 nm thick Fe_3O_4 film is also re-plotted in the same figure. One can clearly see a gradual change of the spectral weight, especially at the L_3 region, from the 20 nm to 5 ML samples. The spectral weight that is marked with the feature A decreases and the main peak with the feature C increases as the films are getting thinner. A similar trend is also observed in the L_2 region although it is less obvious. It is important to note that for the 5 ML film, there is a region where a clear spectral dip exists between the pre-peak with the feature B and the main peak with the feature C. As the film is getting thicker and thicker, the spectral weight in this region is developing.

The existence of the spectral dip between feature B and C for the 5 ML film is likely attributed to a shortage of Fe^{3+} ions in the tetrahedral sites. If it is extrapolated to the initial stage of growth, it is natural to envisage that the tetrahedral Fe^{3+} ions are completely absent in the first monolayer. In order to preserve its bulk stoichiometry, the Fe ions in the octahedral sites are required to fill in the absence of the tetrahedral sites. Theoretically, the ratio of the Fe^{2+} to the Fe^{3+} in the octahedral sites should be close to 1:2; however for the 5 ML film, it seems that the Fe^{2+} contribution is slightly less than the bulk value as it is indicated by the decrease of feature A. As the film is getting thicker, for example the 20 ML film, the spectral dip between feature B and C is less pronounced, indicating that the Fe^{3+} tetrahedral sites are more and more populated. As a consequence, the content of the Fe^{3+}

octahedral sites is gradually decreasing. By increasing the film thickness further, it is expected that the ratio of the Fe^{2+} octahedral and the Fe^{3+} tetrahedral and the Fe^{3+} octahedral sites becomes approximately 1:1:1. This balanced ratio ensures the stoichiometry of the bulk Fe_3O_4 .

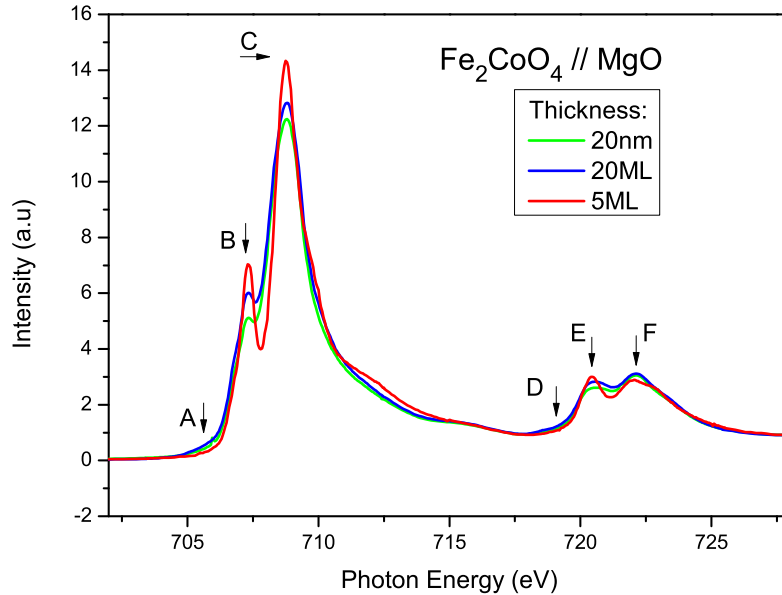


Figure 5.5: Thickness dependent Fe $L_{2,3}$ XAS spectra of Fe_2CoO_4 films.

Thickness dependent XAS spectra at the Fe $L_{2,3}$ edges for Fe_2CoO_4 films are depicted in figure 5.5. One can obviously see that there is practically no spectral weight at the respective leading edges with the feature A and D for all films, demonstrating that the Fe^{2+} ions in the octahedral sites are completely absent as they are substituted by the Co^{2+} dopant ions. It basically verifies the argument in the previous section that only Fe^{3+} cations are distributed in the octahedral and tetrahedral sites for all the Fe_2CoO_4 films. However it does not necessarily mean that the tetrahedral and octahedral Fe^{3+} ions have an equal population for all thickness. As an evidence to affirm this statement, one can clearly notice a progressive development of the spectral weight at the energy position between the feature B and C with increasing thickness. It implies that at the beginning of growth, not only the octahedral Fe^{2+} ions, but also the tetrahedral Fe^{3+} ions are nearly missing. In other words, the initial cationic distribution is mainly dominated by the octahedral Fe^{3+} ions. As a matter of fact, the XAS spectrum of the 5 ML film resembles the reference spectrum of Fe_2O_3 where the Fe^{3+} ions reside in the octahedral symmetry [83]. As the film thickness increases, the tetrahedral Fe^{3+} ions are populated more and more, whereas the proportion of the octahedral Fe^{3+} ions are gradually reduced until they are expected to be balanced at the ratio of 1 to 1 for an ideal

Fe_2CoO_4 film.

From these studies, it can be concluded that both ferrites (Fe_3O_4 and Fe_2CoO_4) share a generic growth mechanism. The Fe ions in the octahedral sites are mainly populated whereas those in the tetrahedral sites are nearly empty in the beginning of growth. Sustaining the stage of film growth, the population of the Fe ions in the tetrahedral sites gradually increases while those in the octahedral sites gradually declines until they reach a balanced ratio. It basically agrees well with the study reported by Chang *et al.* [84] about the initial stage of growth of polar Fe_3O_4 film on MgO substrate, which suggests that in the beginning of growth the Fe^{3+} tetrahedral cations are much less populated than the bulk value, but the bulk stoichiometry is still preserved at each monolayer. They proposed a model for growth process of Fe_3O_4 thin film at the initial stages, where each consecutive nonpolar $\text{Fe}_{3/4}\text{O}$ layers without the tetrahedral Fe^{3+} ions give away one Fe^{3+} ion (or $\text{Fe}_{1/8}$ per formula unit) to the spatial gap in between them so that a layer with two tetrahedral Fe^{3+} ions is formed. This mechanism eventually creates a half charge termination at the most outer layers and acts as a solution to stabilize the polar Fe_3O_4 surface and interface. In fact, this similar model can be extended and applied to explain the growth mechanism of the Fe_2CoO_4 film as well. In this case, one can think a combined nonpolar CoO plus $\text{Fe}_{2/3}\text{O}$ layer without the tetrahedral Fe^{3+} ions as a starting monolayer. While the octahedral Co^{2+} layers remain robust during the growth, each of the $\text{Fe}_{2/3}\text{O}$ layer has to transfer one Fe^{3+} ion per layer to the space in between them, similar to the growth process of Fe_3O_4 . Consequently, it will lead to the elimination of the polar catastrophe at the Fe_2CoO_4 interface.

Magnetic study of $\text{Fe}_{3-x}\text{Co}_x\text{O}_4$ films

6.1 Introduction

Cobalt ferrite (Fe_2CoO_4) has a unique property among the spinel structure ferrite, specifically a large magnetic anisotropy accompanied by a large anisotropy magnetostriction [70, 85]. The origin of magnetic anisotropy in Fe_2CoO_4 is believed to arise from the Co^{2+} ions in the crystalline field of a low symmetry [86]. In the high-spin configuration of Co^{2+} in octahedral site, it has five spins in the lowest-lying threefold degenerating orbital levels in which each spin is subject to exchange field. These orbital levels are further split into d_{xy} , d_{xz} and d_{yz} orbitals by lowering symmetry field of Co^{2+} ion and spin-orbit coupling. The magnitude of this energy splitting depends on the direction of the exchange field, which affects the direction of the magnetization. Based on these phenomena the origin of the anisotropy energy arises.

The investigation on Co-doped in Fe_3O_4 becomes the prototype for understanding the large anisotropy of Co atoms in the spinel structure and the role of directional ordering in induced anisotropy [87]. Several studies recognized that substitution agent and residual strain play an important role in controlling the magnetic easy axis and other magnetic properties of Fe_2CoO_4 so that makes it different from Fe_3O_4 [23, 32, 60, 70, 88, 89]. Moyer *et al.* has been reported that the substitution of a small amount of Co^{2+} ions in spinel ferrite causes the change of magnetic easy axis from in plane to out-of-plane direction [60]. A large anisotropy energy in Fe_2CoO_4 compound makes the magnetic easy axis lies in the out-of-plane direction. Furthermore, the introduction of an underlying substrate constrains the film and gives rise to anomalous behavior which is not observed in the bulk [70]. It has been reported by Huang [32] that strong magnetic anisotropy is highly dependent on the lattice mismatch induced strain.

This chapter will focus on exploring the magnetic anisotropy in $\text{Fe}_{3-x}\text{Co}_x\text{O}_4$ thin films with different Co-substitution concentration ($x = 0, 0.1, 0.5, 1$) and lattice mismatch induced strain in Fe_2CoO_4 thin films. SQUID magnetometry was done to determine the bulk magnetic properties and specify the magnetic easy axis of $\text{Fe}_{3-x}\text{Co}_x\text{O}_4$ films. X-ray Linear Dichroism (XLD) was utilized to investigate the orientation of the orbital and spin physics of Fe_2CoO_4 thin films grown on MgO , MgAl_2O_4 and SrTiO_3 substrate.

6.2 Experimental

Two sets of samples have been prepared: first, for substitution study, 20 nm thick of Co-doped in Fe_3O_4 ($\text{Fe}_{3-x}\text{Co}_x\text{O}_4$ with $x = 0, 0.1, 0.5$ and 1) films grown on MgO substrate; second, the other 20 nm thick Fe_2CoO_4 films grown on MgO, SrTiO_3 and MgAl_2O_4 substrates. Theoretically, due to lattice mismatch between the film and the substrate, the films on the MgO substrate are under tensile strain while those on the SrTiO_3 and MgAl_2O_4 substrates are under compressive strain. Based on structural characterization described in chapter 3, the Fe_2CoO_4 films grew coherently on MgO and MgAl_2O_4 substrates, while the Fe_2CoO_4 films did not grow coherently on SrTiO_3 substrate due to big lattice mismatch between the substrate and the film.

SQUID measurements were performed by using Quantum design MPMS7 magnetometer. The measurements were done in two different geometry: in-plane and out-of-plane applied magnetic field to the film surface. The sample was glued with GE varnish into a piece of straw in order to avoid the sample movement during measurement. Then it was placed in a plastic straw and attached to the MPMS sample probe. The sample was measured in a certain magnetic field up to 5 T. Prior to measurement, the sample position was aligned with 1 T field cooled environment.

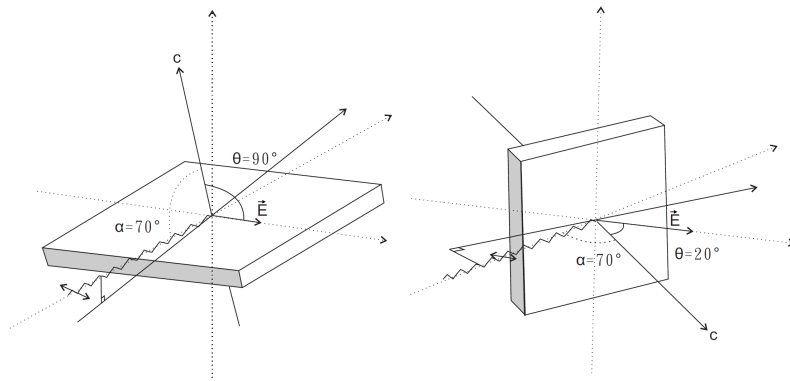


Figure 6.1: XLD measurement geometry [90].

The XLD experiments were performed at the Dragon beamline of the National Synchrotron Radiation Research Center (NSRRC) in Taiwan. The measurement was done by Dr. Zhiwei Hu. The photon energy resolution was set about 0.35 eV at the Co $L_{2,3}$ edges and about 0.3 eV at the Fe $L_{2,3}$ edges with a degree of linear polarization higher than 98 %. The spectra were recorded using the total electron yield method (TEY). The CoO and Fe_2O_3 single crystals were measured simultaneously in separate chambers to calibrate the photon energy.

The samples were tilted with respect to the incoming beam. The Pointing vector of the light made an angle of $\alpha = 70^\circ$ with respect to the c -axis surface normal. To change the polarization, the sample was rotated around the Pointing vector axis as sketched in figure 6.1 [90]. In order to do polarization measurement, the angle between the electric field vector \mathbf{E} and the c axis can be varied between 20° and 90° . This measurement geometry allows doing polarization dependence measurement and guarantees a reliable comparison of the spectral line shape for two polarization directions. Due to different background levels, a spectrum for each sample is required to be normalized to its average spectra intensity after the subtraction of the pre-edge background (approximated by a linear fit). This normalization makes the spectrum comparable from sample to sample.

6.3 Results

6.3.1 Bulk magnetic properties of $\text{Fe}_{3-x}\text{Co}_x\text{O}_4$ films

Figure 6.2(a-d) shows in-plane and out-of-plane M-H loops from SQUID measurements of $\text{Fe}_{3-x}\text{Co}_x\text{O}_4$ grown on MgO substrate. A diamagnetic substrate contribution was subtracted from all the experimental data. Based on these hysteresis loops, the $\text{Fe}_{3-x}\text{Co}_x\text{O}_4$ films grown on MgO substrate exhibit ferromagnetism. The in-plane and out-of-plane values for coercive field (H_c), saturation magnetization (M_s) and remnant magnetization (M_r) are summarized in figure 6.2(e-h) and table 6.1.

The pure Fe_3O_4 film has an in-plane M_s value of 442.19 emu/cc at 100 K. This M_s value is considerably reduced with respect to the bulk value of 514 emu/cc [60]. It is attributed to the presence of antiphase boundaries (APB) or void between the grains. The APBs occurs during the growth of Fe_3O_4 on MgO substrate [91, 92].

Substitution the $\text{Fe}_{3-x}\text{Co}_x\text{O}_4$ ($x = 0, 0.1, 0.5, 1$) films reduce the in-plane M_s value at 100 K from 442.19 emu/cc to 184.76 emu/cc. These values are significantly less than the bulk values which should decrease linearly from 514 to 464 emu/cc with increasing x from 0 to 1 [60]. Besides APBs contribution, the reduction of M_s in $\text{Fe}_{3-x}\text{Co}_x\text{O}_4$ compared to Fe_3O_4 is caused by the smaller magnetic moment of Co^{2+} ($3 \mu_B$) than that of Fe^{2+} ($4 \mu_B$), thus the total magnetic moment decreases with the substitution of Co^{2+} for Fe^{2+} . Another possible reason for reducing M_s is the generation of structural defects which is induced by the difference of the ionic radius between Co^{2+} (0.745\AA) and Fe^{2+} (0.78\AA) [59]. Moreover, as suggested by Moyer *et al.* [60], the reducing M_s in $\text{Fe}_{3-x}\text{Co}_x\text{O}_4$ occurs due to disorder of ferrimagnetism alignment between the octahedral and tetrahedral sites for doped samples.

Further magnetic information that can be acquired from figure 6.2 is the mag-

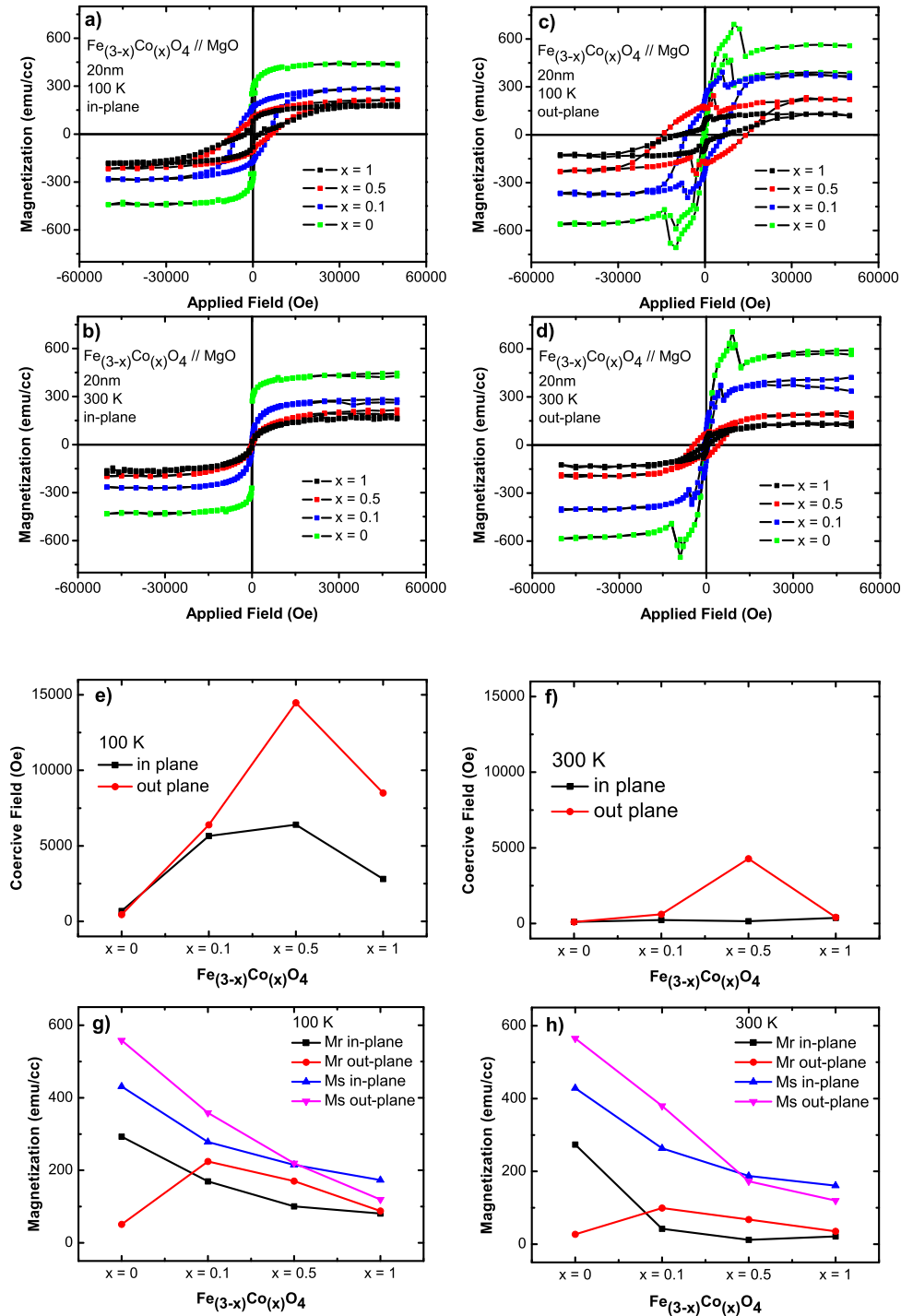


Figure 6.2: (a-d) Hysteresis loops of the 20nm thick $\text{Fe}_{3-x}\text{Co}_x\text{O}_4$ films ($x = 0, 0.1, 0.5, 1$) on MgO substrate at 100 K (a) and 300 K (b) with an applied magnetic field aligned in the in-plane direction, as well as at 100 K (c) and 300 K (d) aligned in the out-of-plane direction. (e-h) Their associated magnetic values: comparison of in-plane and out-of-plane coercive fields at 100 K (e) and 300 K (f), and in-plane and out-of-plane saturation and remnant magnetization at 100 K (g) and 300 K (h).

x	Temp. (K)	H _c (Oe) H//ab	H _c (Oe) H//c	Mr (emu/cm ³) H//ab	Mr (emu/cm ³) H//c	Ms (emu/cm ³) H//ab	Ms (emu/cm ³) H//c
x = 0	100	681	448	292.83	51	442.19	562.03
	300	101	99	273.55	27	433.37	586.49
x = 0.1	100	5648	6393	169.37	224.18	285.03	368.78
	300	223	600	42.35	99.36	264.91	408.29
x = 0.5	100	6400	14475	100.68	170.33	216.13	232.62
	300	143	4274	11.92	67.64	199.31	186.73
x = 1	100	2804	8500	80.65	87.79	184.76	130.57
	300	360	400	21.39	35.48	179.69	124.11

Table 6.1: Table of coercivity, remnant and saturation magnetization of $\text{Fe}_{3-x}\text{Co}_x\text{O}_4$ ($x = 0, 0.1, 0.5, 1$) on MgO (100) at 100 K and 300 K. H//ab denotes magnetic field is applied parallel to the in-plane direction and H//c denotes the out-of-plane direction.

netic easy axes. It is determined by comparing the in-plane and out-of-plane H_c value. As plotted in figure 6.2e and 6.2f, the H_c values of Co-doped samples ($\text{Fe}_{3-x}\text{Co}_x\text{O}_4$) are larger for the out-of-plane than the in-plane direction. Meanwhile, the pure sample (Fe_3O_4) shows the opposite where the in-plane H_c is larger than the out-of-plane direction. This leads to the conclusion that the $\text{Fe}_{3-x}\text{Co}_x\text{O}_4$ ($x = 0.1, 0.5, 1$) films have an out-of-plane magnetic easy axes in contrast to the Fe_3O_4 sample which has an in-plane magnetic easy axis. This finding is coherent with the result by Moyer *et al.* [60].

Furthermore, the in-plane H_c at 100 K jumps from 681 Oe for the Fe_3O_4 sample to about 6400 Oe as the Co concentration increases up to about 16.25% ($\text{Fe}_{3-x}\text{Co}_x\text{O}_4$ $x = 0.5$), and thereafter slightly decreases to 2804 Oe when the Co-substitution concentration rises to 33% (Fe_2CoO_4). It suggests that Co-doped in $\text{Fe}_{3-x}\text{Co}_x\text{O}_4$ sample is a very hard ferromagnetic film due to higher magnetocrystalline anisotropy. The enhancement of H_c in Co-doped samples ($\text{Fe}_{3-x}\text{Co}_x\text{O}_4$) has attributed to the increase of anisotropy due to enhancement Co^{2+} content [24]. However, in this work, when the Co-substitution concentration is higher than about 16.25% (just about 50% Fe^{2+} in the octahedral site are replaced by Co^{2+}), the H_c reduces with increasing Co-substitution concentration. This phenomenon is also reported by Tripathy *et al.* [23]. It might suggest that the interaction between Fe^{2+} and Co^{2+} dopant ions affects the strength of the coercive field. It reaches the maximum value when approximately 50% of Fe^{2+} is replaced by Co^{2+} in $\text{Fe}_{3-x}\text{Co}_x\text{O}_4$ sample.

According to the M-H loop results, it can be concluded that the magnetic prop-

erties of the Co-doped ($\text{Fe}_{3-x}\text{Co}_x\text{O}_4$) samples are drastically different compared to the pure (Fe_3O_4) sample, with the $\text{Fe}_{3-x}\text{Co}_x\text{O}_4$ ($x = 0.1, 0.5, 1$) having notably reduced M_s and larger H_c than the Fe_3O_4 sample. Moreover, since the Co ion has a big magnetocrystalline constant which can induce magnetic anisotropy in $\text{Fe}_{3-x}\text{Co}_x\text{O}_4$ sample, the magnetic easy axis switches from the in-plane direction for the Fe_3O_4 film to the out-of-plane direction for the Co-doped Fe_3O_4 film.

6.3.2 Magnetic anisotropy induced by strain in Fe_2CoO_4 films

This section is focused on the magnetic properties of Fe_2CoO_4 thin films epitaxially grown on three different substrates, MgO , SrTiO_3 and MgAl_2O_4 as a model system for Fe_2CoO_4 under epitaxial strain. Due to the lattice mismatch between the film and the substrate, the Fe_2CoO_4 experiences tensile strain from MgO substrate and compressive strain from SrTiO_3 and MgAl_2O_4 substrate, respectively. The objective is to establish how the magnetic anisotropy as well as the spin and orbital contributions to the magnetic moments depend on the lowering of the local crystal field symmetry by epitaxial strain.

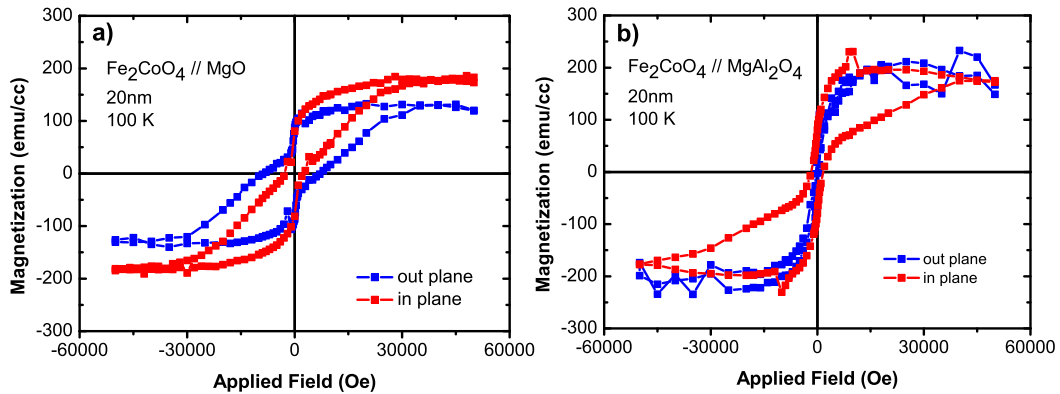


Figure 6.3: Hysteresis loops of the 20nm thick $\text{Fe}_{3-x}\text{Co}_x\text{O}_4$ film on MgO (a) and MgAl_2O_4 (b) substrate at 100 K with an applied magnetic field aligned in the in-plane (red) and out-of-plane (blue) direction.

It was explicitly asserted in the chapter 3 that Fe_2CoO_4 thin films grow coherently on MgO and MgAl_2O_4 substrates, in contrast to that on SrTiO_3 substrate. To verify the magnetic properties of the former samples, particularly their magnetic easy axis in relation to its strain, SQUID measurements were conducted on both films. Figure 6.3 shows the hysteresis loops measured at 100 K for the 20 nm Fe_2CoO_4 films grown on MgO (panel a) and MgAl_2O_4 (panel b) substrates. Note that the small diamagnetic contribution of each substrate has been subtracted from

each raw data. As seen in figure 6.3, both films exhibit a clear ferromagnetic hysteresis behavior. The M_s and H_c values for in-plane and out-of plane direction of Fe_2CoO_4 grown on MgAl_2O_4 substrate are found to be 174.69 emu/cc and 2000 Oe, and 198.8 emu/cc and 400 Oe, respectively. As the in-plane H_c value is higher than the out-of-plane one, it can be determined that the Fe_2CoO_4 film on MgAl_2O_4 has a magnetic easy axis in the in-plane direction. On the other hand, the Fe_2CoO_4 film grown on MgO substrate has a lower in-plane H_c value, therefore it possesses out-of-plane magnetic easy axis. Furthermore, comparing the in-plane and out-of plane H_c values between these two samples, it can be seen that the Fe_2CoO_4 grown on MgO has the in-plane H_c three times higher than the out-of plane one (see table 6.1), while the Fe_2CoO_4 grown on MgAl_2O_4 has the out-of-plane H_c five times higher than the in-plane one. It basically designates that the anisotropy of both films, especially that on MgAl_2O_4 substrate is very strong. To put it simply, the distinct magnetic easy axis of the Fe_2CoO_4 film in dependence on a substrate indicates that the magnetic properties of the film can essentially be controlled by tuning the lattice mismatch between the film and the substrate.

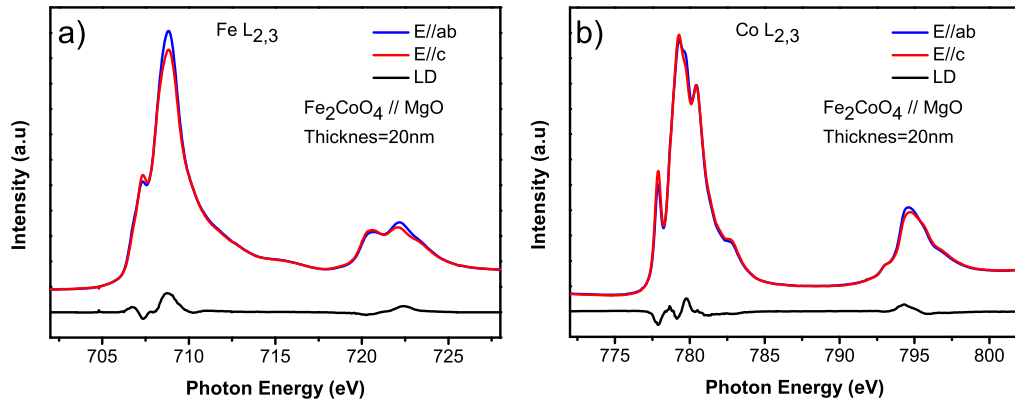


Figure 6.4: The polarization dependent Fe $L_{2,3}$ edges (a) and Co $L_{2,3}$ edges (b) XAS spectra of Fe_2CoO_4 on MgO substrate. E//ab denotes in-plane and E//c denotes out-of-plane polarization. The linear dichroism (LD) spectra defined as E//ab - E//c are also shown at the bottom.

To find a correlation between the SQUID magnetic anisotropy and the anisotropy of the valance charge as well as their dependence on strain, polarization-dependent XAS measurements on the Fe_2CoO_4 films were also carried out. Figure 6.4 shows the Fe $L_{2,3}$ edges (a) and Co $L_{2,3}$ edges (b) XAS spectra of Fe_2CoO_4 on MgO substrate for E//ab (in-plane) and E//c (out-of-plane) polarization. One can clearly see the polarization contrast between the two orientations at both edges. The spectral difference between the two polarization (E//ab - E//c), known as linear dichroism

(LD), is also plotted in the bottom part of the figure. The XLD spectra of Fe_2CoO_4 on MgO are in agreement with those reported by Moyer *et al.* [60]. The LD region of the Fe L_3 edge is characterized by two positive peaks at 706.8 eV and 708.8 eV, and three negative peaks at 707.3 eV, 708.1 eV and 710.3 eV, while the Fe L_2 edge has a broad negative peak at 720.6 eV and a broad positive peak at 722.3 eV. For the Co L_3 edge, the LD regions of interest are three negative peaks at 777.9 eV, 779.1 eV and 781 eV, and three positive peaks at 778.65 eV, 779.75 eV, and 780.7 eV, while the Co L_2 edge has a broad positive peak at 794.3 eV and a broad negative peak at 795.5 eV. As a quantitative analysis is not presented in this work, the discussion below will use these highlighted characteristics in comparison with those of the Fe_2CoO_4 film on different substrates. In general, the linear dichroic effect of the XLD spectra originates from either charge anisotropies that are caused by a lower crystal field than cubic symmetry (pure charge distribution) or a combination of the charge distribution and those that are induced by exchange and spin-orbit interactions relative to the easy magnetic axis (spin distribution).

The polarization-dependent XAS of the Fe_2CoO_4 film grown on MgAl_2O_4 (top panel) and SrTiO_3 (middle panel) substrates are now depicted together with those on MgO (bottom panel) substrate in figure 6.5 for the Fe $L_{2,3}$ edges and in figure 6.6 for the Co $L_{2,3}$ edge, respectively. In the same figures, each of LD spectra is displayed with a magnification of a factor of 5 for clarity. By focusing first onto the spectra on MgAl_2O_4 and MgO substrates, one can clearly see that some spectral features of that on MgAl_2O_4 are diametrically opposed to those on MgO. For instance, the intensity of the Fe L_3 main peak at 708.8 eV in the $\text{Fe}_2\text{CoO}_4/\text{MgAl}_2\text{O}_4$ is higher for E//c, while that in $\text{Fe}_2\text{CoO}_4/\text{MgO}$ is higher for E//ab. In fact, the sign of LD at both the Fe $L_{2,3}$ edges and Co $L_{2,3}$ edges is all reversed between the two cases. It basically validates that the Fe_2CoO_4 films undergo opposite strain due to substrates, i.e., a compressive strain on MgAl_2O_4 substrate versus a tensile strain on MgO. Moreover, for the sake of clarity, the contrast of the LD sign and the change of the LD magnitude for all films are also plotted in figure 6.7(a) for the Fe $L_{2,3}$ and (b) for the Co $L_{2,3}$. Here it is observed that although the magnitude of LD of $\text{Fe}_2\text{CoO}_4/\text{SrTiO}_3$ is somewhat smaller, its overall LD sign seems to closely resemble that on MgO substrate. It is not surprising to find a slight tensile strain of Fe_2CoO_4 film on SrTiO_3 as it is in essence consistent with the XRD results outlined in the chapter 3.

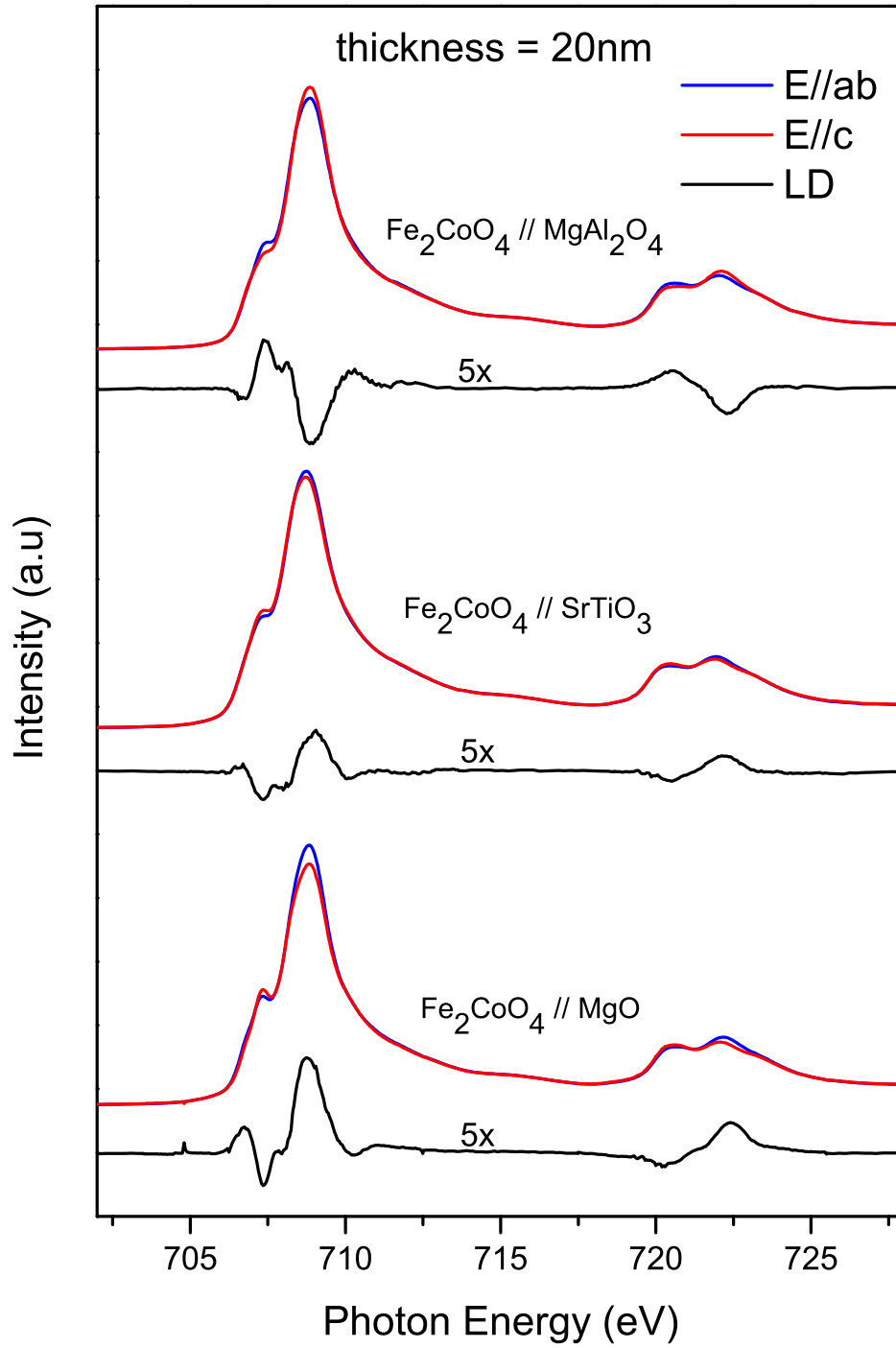


Figure 6.5: The polarization dependent Fe $L_{2,3}$ XAS edges spectra (from top to bottom) of 20 nm thick Fe_2CoO_4 films on MgAl_2O_4 , SrTiO_3 , and MgO substrates. Spectra is shown for two different beam polarization with respect to the surface normal of the film: E//ab (blue line) and E//c (red line). The spectral difference (LD) is shown by a black line.

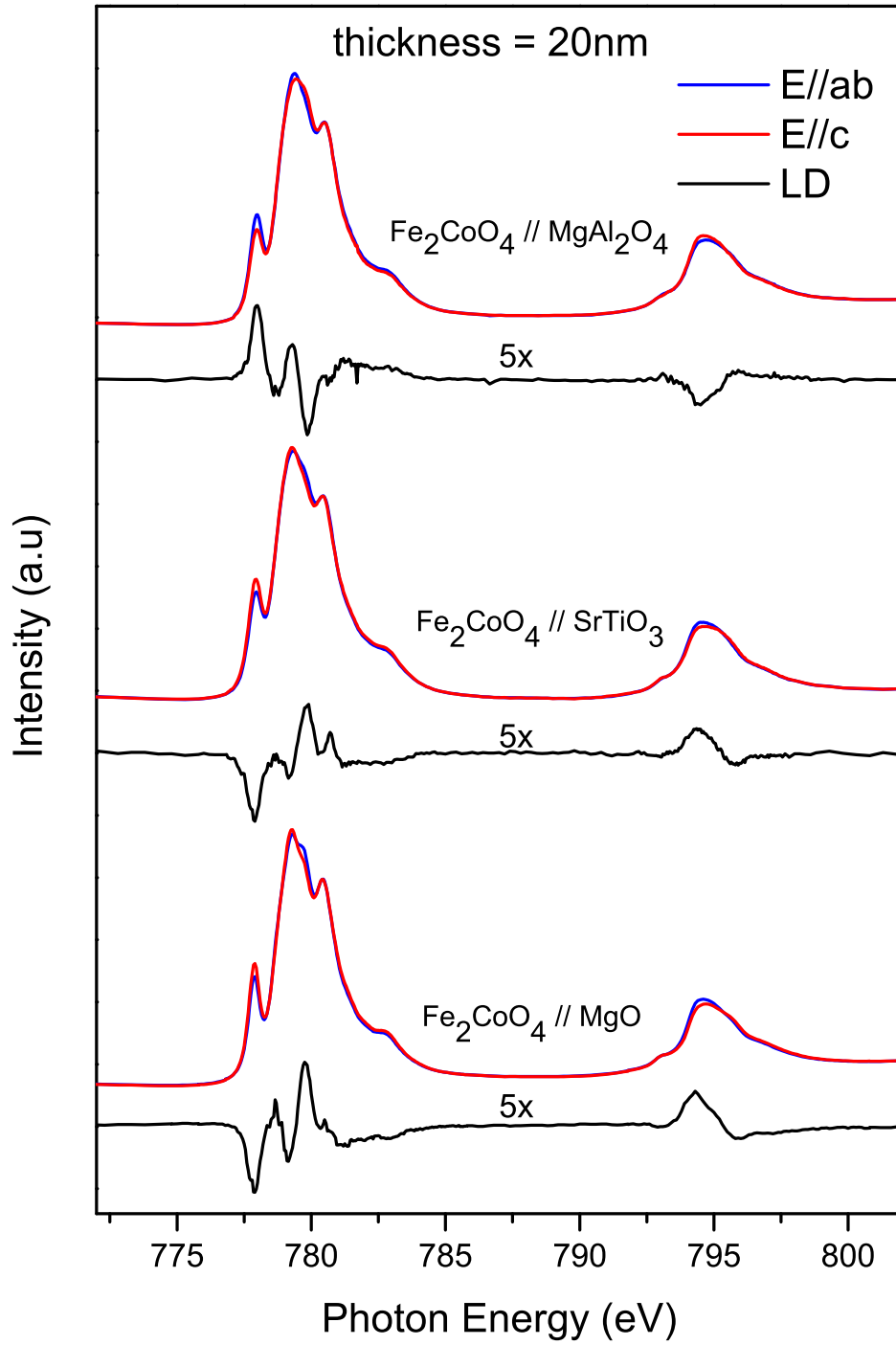


Figure 6.6: The polarization dependent Co $L_{2,3}$ XAS edges spectra (from top to bottom) of 20 nm thick Fe_2CoO_4 films on MgAl_2O_4 , SrTiO_3 , and MgO substrates. Spectra is shown for two different beam polarization with respect to the surface normal of the film: $E//ab$ (blue line) and $E//c$ (red line). The spectral difference (LD) is shown by a black line.

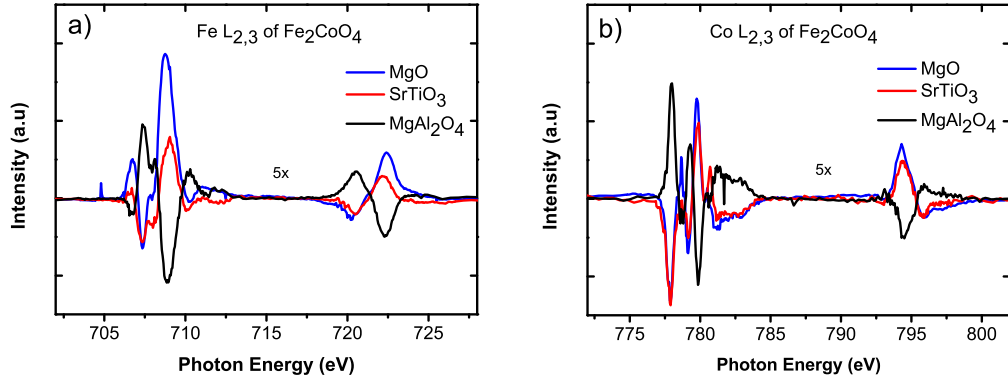


Figure 6.7: The LD spectra of 20 nm thick Fe_2CoO_4 film on MgO (blue line), SrTiO_3 (red) and MgAl_2O_4 (black) substrates at the Fe $L_{2,3}$ edges (a) and Co $L_{2,3}$ edges (b). All spectra are magnified by a factor of 5 for clarity.

Naively, one may not have expected to observe an LD effect at the Fe $L_{2,3}$ edges as the half-filled Fe^{3+} ion (i.e., the $3d^5$ electron configuration in the high spin state) in Fe_2CoO_4 is essentially spherically symmetric. Even if the lattice is distorted due to strain, the charge density in the ground state remains close to the spherical symmetry. One possible cause of the observed natural LD at the Fe $L_{2,3}$ edges is therefore linked to the non-degenerate final-state orbital energies. A distortion can lift the degeneracy of the final state, where an electron has to cost a different amount of energy, depending on the orbital that the electron is added to. In addition to the final state charge anisotropy, the LD effect may also be originated to the slight deformation of the charge distribution due to exchange interaction between the Fe^{3+} ions in the tetrahedral site and the Fe^{3+} ions as well as the Co^{2+} ions in the octahedral site. It is notes that the LD measurements were conducted far below the Curie temperature of Fe_2CoO_4 of ca. 790 K.

Going to the Co $L_{2,3}$ edges XLD spectra in figure 6.6 and 6.7 (b), one can clearly observe that the LD sign is predominantly positive for the Fe_2CoO_4 film on MgAl_2O_4 substrate and negative for that on MgO substrate. So how does the strain-dependent LD sign of Fe_2CoO_4 films correlate to its SQUID magnetic easy axis result? It is known that based on ligand field theory, the atomic $3d$ levels in Oh symmetry are split into a threefold degenerate t_{2g} and twofold degenerate e_g orbitals. In one-electron-like picture, Co^{2+} ions with $3d^7$ electron configuration in the high spin state have therefore one hole in the spin-down t_{2g} and two holes in the spin-down e_g orbitals. Lowering the symmetry due to a tetragonal distortion, where the c -axis (out-of-plane) is not similar to the a -axis (in-plane), further splits the t_{2g} levels into the lower d_{xy} level and the higher d_{xz} and d_{yz} levels for $c/a \ll 1$ (tensile strain) or the lower d_{xz} and d_{yz} levels and the higher d_{xy} level for $c/a \gg 1$

(compressive strain). The negative LD sign for the $\text{Fe}_2\text{CoO}_4/\text{MgO}$ may indicate that the only t_{2g} hole resides in the combined state of d_{xz} and d_{yz} orbitals. This state has an orbital moment which is oriented out-of-plane. Mediated by the spin-orbit coupling, the orientation of the spin moment is then out-of-plane also. It seems that the t_{2g} hole in the d_{xz}/d_{yz} states ensures the observation of the out-of-plane magnetic easy axis as revealed by the SQUID results (see Fig. 6.3a). For the other case of the $\text{Fe}_2\text{CoO}_4/\text{MgAl}_2\text{O}_4$ where the positive LD sign implies that the t_{2g} hole mainly resides in the d_{xy} orbital, one can obtain that the orbital moment and the spin moment are indeed directed in-plane, similar to the case of $\text{CoO}/\text{Ag}(100)$ [34]. This also explains why the SQUID results in figure 6.3b exhibit that the magnetic easy axis is directed in-plane for the $\text{Fe}_2\text{CoO}_4/\text{MgAl}_2\text{O}_4$.

As a conclusion, the SQUID and XLD results confirm a magnetic anisotropy behavior induced by strain in the Fe_2CoO_4 film. The Fe_2CoO_4 film grown on MgO substrate under tensile strain has out-of-plane magnetic easy axis, where the t_{2g} hole in the d_{xz}/d_{yz} orbital carries the out-of-plane magnetic moment. On the contrary, the Fe_2CoO_4 film grown on MgAl_2O_4 substrate experiences compressive strain. It has in-plane magnetic easy axis, where the t_{2g} hole in the d_{xy} orbital carries the in-plane magnetic moment. The behavior of Co^{2+} ion under strain in the Fe_2CoO_4 film is consistent with that in CoO film [34]. Control over the sign and direction of the strain may open new opportunities for applications in the field of exchange bias in magnetic thin film.

CHAPTER 7

Summary

$\text{Fe}_{3-x}\text{Co}_x\text{O}_4$ ($x = 0, 0.1, 0.5, 1$) thin films were grown successfully by using MBE technique. MgO substrate was chosen as a substrate due to the small lattice mismatch between the substrate and the film. In addition, three different thicknesses (5ML, 20ML and 20 nm) of Fe_3O_4 and Fe_2CoO_4 films were also grown on MgO substrate. Besides MgO substrate, Fe_2CoO_4 film was also grown on two other substrates (MgAl_2O_4 and SrTiO_3). Based on the lattice mismatch between the substrate and the film, the substrates can induce tensile (MgO and SrTiO_3) and compressive (MgAl_2O_4) strains to the Fe_2CoO_4 film. All of these are part of a comprehensive study of changes in the physical properties of Fe_3O_4 film by the effects of Co-substitution, thickness and strains induced by the substrates.

The structural study using RHEED and LEED measurements showed that substitution Co atoms to Fe_3O_4 compound established $\text{Fe}_{3-x}\text{Co}_x\text{O}_4$ ($x = 0, 0.1, 0.5, 1$) compounds. The RHEED patterns of $\text{Fe}_{3-x}\text{Co}_x\text{O}_4$ films grown on MgO and MgAl_2O_4 substrates showed streak patterns which indicate the presence of a smooth and flat surface. The diffraction rods of $\text{Fe}_{3-x}\text{Co}_x\text{O}_4$ films grown on MgO substrate appeared on the half spacing of the substrate diffraction rods. It means the in-plane dimension of the spinel unit cell of $\text{Fe}_{3-x}\text{Co}_x\text{O}_4$ is exactly twice of the rocksalt unit cell of MgO. For $\text{Fe}_{3-x}\text{Co}_x\text{O}_4$ films grown on MgAl_2O_4 substrate, both of them have a spinel structure with face centered symmetry. Therefore, it found that they have the same diffraction rods, meaning the film follows the substrate structure. The contrary was shown for $\text{Fe}_{3-x}\text{Co}_x\text{O}_4$ grown on SrTiO_3 substrate. It had spotty RHEED patterns which show a tendency of the island terminated growth [33, 67, 68]. Bigger lattice mismatch makes the $\text{Fe}_{3-x}\text{Co}_x\text{O}_4$ films not grow coherently on SrTiO_3 but still show epitaxial growth. Furthermore, the XRD measurements complete the structural study of Fe_2CoO_4 films on MgO, MgAl_2O_4 and SrTiO_3 substrates. It suggests that the Fe_2CoO_4 grown on MgO and MgAl_2O_4 substrates have strained consistent to their lattice mismatches, i.e., tensile strain for Fe_2CoO_4 on MgO substrate and compressive strain for Fe_2CoO_4 on MgAl_2O_4 substrate. Meanwhile the Fe_2CoO_4 grown on SrTiO_3 has tensile strain even though the lattice mismatch would indicate a preference for compressive strain. This tensile behavior proves that the film has already relaxed, so that it shows an island growth mode.

The XPS study was done to provide the information on the chemical composition and the valencies of the cations down to Co-substitution in $\text{Fe}_{3-x}\text{Co}_x\text{O}_4$ films.

Its valence band spectra can acquire the information on the electronic properties of $\text{Fe}_{3-x}\text{Co}_x\text{O}_4$ films. Based on XPS survey scan result, the Fe, Co and O core level peaks and also its Auger peaks are clearly seen in the spectra. There is no other peaks especially C peak in the spectrum meaning that the surfaces are very clean without any contaminants. The O 1s core-level spectra also support this argument that show a single-peak shape without low-intensity side band, meaning only single anion site is presence in the sample. Both Fe 2p and Co 2p core level spectra show a characteristic of strong charge transfer satellites. It is originated from the charge transfer interaction between the ligand 2p orbitals and the transition metal. Based on Fe 2p core-level spectra, it confirms that the Co-substitution replaces the Fe^{2+} in octahedral site. Therefore, the Fe^{3+} ions only remain in octahedral and tetrahedral site for Fe_2CoO_4 film. This finding is also supported by Co 2p core-level which shows a characteristic of Co^{2+} valency. However, the spectra line shape of Fe 2p and Co 2p core levels indicate a characteristic of high spin state for all the cations in $\text{Fe}_{3-x}\text{Co}_x\text{O}_4$ films. thus it is expected that the 2p core level line shape will be broaden by unresolved multiplet splitting [71]. Furthermore, the XPS valance band spectra showed a tendency of reduced spectra weight around the Fermi energy with the increase of Co-substitution in $\text{Fe}_{3-x}\text{Co}_x\text{O}_4$ films.

The XAS study also completes the XPS results due to its site and symmetry selective character in $L_{2,3}$ XAS spectra. It qualitatively figured out the sites occupation for different Co-substitution concentration in $\text{Fe}_{3-x}\text{Co}_x\text{O}_4$ films. It suggests that the ratio of Fe^{3+} cations to the total number of iron cations increases and the Fe^{2+} octahedral reduces as the Co-substitution concentration increases in the sample. As a result, it confirms that the Fe $L_{2,3}$ XAS spectra of Fe_2CoO_4 are mainly composed by Fe^{3+} in octahedral and tetrahedral site. The Co $L_{2,3}$ XAS spectra also verify that the Fe^{2+} in octahedral site is mainly replaced by Co^{2+} sitting in octahedral site. There is also very small indication for Co^{2+} sitting in tetrahedral site in Fe_2CoO_4 film. But, there is no indication of Co higher valency (Co^{3+}) in $\text{Fe}_{3-x}\text{Co}_x\text{O}_4$ films.

The information about the growth process in ferrite film is also obtained from the XAS study. It suggests the site occupancies for different film thickness in Fe_3O_4 and Fe_2CoO_4 films. It can be concluded that both ferrites (Fe_3O_4 and Fe_2CoO_4) share a generic growth mechanism. The Fe ions in the octahedral sites are mainly populated whereas those in the tetrahedral sites are nearly empty in the beginning of growth. Sustaining the stage of film growth, the population of the Fe ions in the tetrahedral sites gradually increases while those in the octahedral sites gradually declines until they reach a balanced ratio. It basically agrees well with the study reported by Chang *et al.* [84] about the initial stage of growth of polar Fe_3O_4 film on MgO substrate, which suggests that in the beginning of growth the Fe^{3+} tetrahedral cations are much less populated than the bulk value, but the bulk stoichiometry is still preserved at each monolayer. The proposed a model for growth process of

Fe_3O_4 thin film at the initial stages, where each consecutive nonpolar $\text{Fe}_{3/4}\text{O}$ layers without the tetrahedral Fe^{3+} ions give away one Fe^{3+} ion (or $\text{Fe}_{1/8}$ per formula unit) to the spatial gap in between them so that a layer with two tetrahedral Fe^{3+} ions is formed. This mechanism eventually creates a half charge termination at the most outer layers and acts as a solution to stabilize the polar Fe_3O_4 surface and interface. In fact, this similar model can be extended and applied to explain the growth mechanism of the Fe_2CoO_4 film as well. In this case, one can think a combined nonpolar CoO plus $\text{Fe}_{2/3}\text{O}$ layer without the tetrahedral Fe^{3+} ions as a starting monolayer. While the octahedral Co^{2+} layers remain robust during the growth, each of the $\text{Fe}_{2/3}\text{O}$ layer has to transfer one Fe^{3+} ion per layer to the space in between them, similar to the growth process of Fe_3O_4 . Consequently, it will lead to the elimination of the polar catastrophe at the Fe_2CoO_4 interface.

SQUID magnetometry was done to utilize the bulk magnetic properties and specify the magnetic easy axis of $\text{Fe}_{3-x}\text{Co}_x\text{O}_4$ films grown on MgO substrate. It was done by applying a particular magnetic field up to 5 T. Two different measurement geometries (in-plane and out-of-plane) were done in order to differentiate the magnetic anisotropy in this sample. According to the M-H loop results, the magnetic properties of the Co-doped ($\text{Fe}_{3-x}\text{Co}_x\text{O}_4$) samples are drastically different compared to the pure (Fe_3O_4) sample with the $\text{Fe}_{3-x}\text{Co}_x\text{O}_4$ ($x = 0.1, 0.5, 1$) having notably reduced M_s and larger H_c than the Fe_3O_4 sample. Also, since the Co element has a big magnetocrystalline constant which can induce magnetic anisotropy in $\text{Fe}_{3-x}\text{Co}_x\text{O}_4$ sample, it turns the magnetic easy axis of Fe_3O_4 from in-plane direction to out-of-plane for Co-doped in $\text{Fe}_{3-x}\text{Co}_x\text{O}_4$ films.

The magnetic study on Fe_2CoO_4 film due to the lowering of the local crystal field symmetry by epitaxial strain was done by performing SQUID and XLD measurements. The origin of magnetic anisotropy in Fe_2CoO_4 is believed to arise from the Co^{2+} ions in the crystalline field of a low symmetry [86]. In the high-spin configuration of Co^{2+} in octahedral site, it has five spins in the lowest-lying threefold degenerating orbital levels in which each spin is subject to exchange field. These orbital levels are further split into d_{xy} , d_{xz} and d_{yz} orbitals by lowering symmetry field of Co^{2+} ion and spin-orbit coupling. The magnitude of this energy splitting depends on the direction of the exchange field, which depends on the direction of the magnetization. The measurement results confirm a magnetic anisotropy behavior induced by strain in the Fe_2CoO_4 film. The Fe_2CoO_4 grown on MgO substrate under tensile strain has out-of-plane magnetic easy axis and also out-of-plane orbital occupation for Co^{2+} ion. The other way around happened in Fe_2CoO_4 film grown on MgAl_2O_4 substrate which experiences compressive strain, it has in-plane magnetic easy axis and in-plane orbital occupation for Co^{2+} ions. The behavior of Co^{2+} ion under strain is consistent from the previous study on CoO film [34]. Control over the sign and direction of the strain may open new opportunities for applications in the field of exchange bias in magnetic thin film.

Bibliography

- [1] H. Zheng, J. Wang, S. E. Lofland, Z. Ma, L. Mohaddes-Ardabili, T. Zhao, L. Salamanca-Riba, S. R. Shinde, S. B. Ogale, F. Bai, D. Viehland, Y. Jia, D. G. Schlom, M. Wuttig, A. Roytburd, and R. Ramesh. *Multiferroic BaTiO₃-CoFe₂O₄ Nanostructures*. *Science*, 303(5658):661–663, 2004.
- [2] K.F. Wang, J.-M. Liu, and Z.F. Ren. *Multiferroicity: the coupling between magnetic and polarization orders*. *Advances in Physics*, 58(4):321–448, 2009.
- [3] Ce-Wen Nan, M. I. Bichurin, Shuxiang Dong, D. Viehland, and G. Srinivasan. *Multiferroic magnetoelectric composites: Historical perspective, status, and future directions*. *Journal of Applied Physics*, 103(3):031101, 2008.
- [4] Chow Hong Sim, Z. Z. Pan, and John Wang. *Residual stress and magnetic behavior of multiferroic CoFe₂O₄/Pb(Zr_{0.52}Ti_{0.48})O₃ thin films*. *Journal of Applied Physics*, 105(8):084113, 2009.
- [5] J. J. Yang, Y. G. Zhao, H. F. Tian, L. B. Luo, H. Y. Zhang, Y. J. He, and H. S. Luo. *Electric field manipulation of magnetization at room temperature in multiferroic CoFe₂O₄/Pb(Mg_{1/3}Nb_{2/3})_{0.7}Ti_{0.3}O₃ heterostructures*.
- [6] R. A. de Groot, F. M. Mueller, P. G. van Engen, and K. H. J. Buschow. New class of materials: Half-metallic ferromagnets. *Phys. Rev. Lett.*, 50:2024–2027, Jun 1983.
- [7] Akira Yanase and Kiiti Siratori. Band structure in the high temperature phase of fe₃o₄. *Journal of the Physical Society of Japan*, 53(1):312–317, 1984.
- [8] R. A. de Groot, F. M. Mueller, P. G. van Engen, and K. H. J. Buschow. Half-metallic ferromagnets and their magneto-optical properties (invited). *Journal of Applied Physics*, 55(6), 1984.
- [9] R.A. de Groot and K.H.J. Buschow. Recent developments in half-metallic magnetism. *Journal of Magnetism and Magnetic Materials*, 54-57, Part 3(0):1377 – 1380, 1986.
- [10] Mizue Ishikawa, Hidekazu Tanaka, and Tomoji Kawai. *Preparation of highly conductive Mn-doped Fe₃O₄ thin films with spin polarization at room temperature using a pulsed-laser deposition technique*. *Applied Physics Letters*, 86(22):222504, 2005.

- [11] Daniel Fritsch and Claude Ederer. *Effect of epitaxial strain on the cation distribution in spinel ferrites CoFe_2O_4 and NiFe_2O_4 : A density functional theory study*. *Applied Physics Letters*, 99(8):081916, 2011.
- [12] Y H Hou, Y J Zhao, Z W Liu, H Y Yu, X C Zhong, W Q Qiu, D C Zeng, and L S Wen. *Structural, electronic and magnetic properties of partially inverse spinel CoFe_2O_4 : a first-principles study*. *Journal of Physics D: Applied Physics*, 43(44):445003, 2010.
- [13] C.D. Owens. *A Survey of the Properties and Applications of Ferrites below Microwave Frequencies*. *Proceedings of the IRE*, 44(10):1234 –1248, oct 1956.
- [14] Yong Hui Li, Taejoon Kouh, In-Bo Shim, and Chul Sung Kim. *Investigation of cation distribution in single crystalline $\text{Fe}_{3-x}\text{Mn}_x\text{O}_4$ microspheres based on Mössbauer spectroscopy*. *Journal of Applied Physics*, 111(7):07B544, 2012.
- [15] P. Sivakumar, R. Ramesh, A. Ramanand, S. Ponnusamy, and C. Muthamizhchelvan. *Synthesis and characterization of nickel ferrite magnetic nanoparticles*. *Materials Research Bulletin*, 46(12):2208 – 2211, 2011.
- [16] L. Ajroudi, S. Villain, V. Madigou, N. Mliki, and Ch. Leroux. *Synthesis and microstructure of cobalt ferrite nanoparticles*. *Journal of Crystal Growth*, 312(16):2465 – 2471, 2010.
- [17] S. Ghatak, M. Sinha, A.K. Meikap, and S.K. Pradhan. *Electrical transport properties of nanocrystalline zinc ferrite*. *Physica E: Low-dimensional Systems and Nanostructures*, 40(8):2686 – 2693, 2008.
- [18] K. Khaja Mohaideen and P. A. Joy. *High magnetostriction and coupling coefficient for sintered cobalt ferrite derived from superparamagnetic nanoparticles*. *Applied Physics Letters*, 101(7):072405, 2012.
- [19] Junichi Takaobushi, Hidekazu Tanaka, Tomoji Kawai, Shigenori Ueda, Jung-Jin Kim, Masaaki Kobata, Eiji Ikenaga, Makina Yabashi, Keisuke Kobayashi, Yoshinori Nishino, Daigo Miwa, Kenji Tamasaku, and Tetsuya Ishikawa. *$\text{Fe}_{3-x}\text{Zn}_x\text{O}_4$ thin film as tunable high Curie temperature ferromagnetic semiconductor*. *Applied Physics Letters*, 89(24):242507, 2006.
- [20] Junichi Takaobushi, Mizue Ishikawa, Shigenori Ueda, Eiji Ikenaga, Jung-Jin Kim, Masaaki Kobata, Yukiharu Takeda, Yuji Saitoh, Makina Yabashi, Yoshinori Nishino, Daigo Miwa, Kenji Tamasaku, Tetsuya Ishikawa, Issei Satoh,

- Hidekazu Tanaka, Keisuke Kobayashi, and Tomoji Kawai. *Electronic structures of $Fe_{3-x}M_xO_4$ ($M = Mn, Zn$) spinel oxide thin films investigated by x-ray photoemission spectroscopy and x-ray magnetic circular dichroism*. *Phys. Rev. B*, 76:205108, Nov 2007.
- [21] Shigenori Ueda, Hidekazu Tanaka, Junichi Takaobushi, Eiji Ikenaga, Jung-Jin Kim, Masaaki Kobata, Tomoji Kawai, Hitoshi Osawa, Naomi Kawamura, Motohiro Suzuki, and Keisuke Kobayashi. *Hard X-ray Photoemission Spectroscopy Combined with Magnetic Circular Dichroism: Application to $Fe_{3-x}Zn_xO_4$ Spinel Oxide Thin Films*. *Appl. Phys. Express*, 1:077003, 2008.
- [22] J. A. Moyer, C. A. F. Vaz, E. Negusse, D. A. Arena, and V. E. Henrich. *Controlling the electronic structure of $Co_{1-x}Fe_{2+x}O_4$ thin films through iron doping*. *Phys. Rev. B*, 83:035121, Jan 2011.
- [23] D. Tripathy, S.N. Adeyeye, A.O. and Piramanayagam, C.S. Mah, Xingyu Gao, and A.T.S. Wee. *Effect of cobalt doping concentration on the structural and magnetic properties of Fe_3O_4* . *Thin Solid Films*, 505:45, 2006.
- [24] D. Tripathy, A. O. Adeyeye, C. B. Boothroyd, and S. N. Piramanayagam. *Magnetic and transport properties of Co-doped Fe_3O_4 films*. *J. Appl. Phys.*, 101:013904, 2007.
- [25] Deepak Venkateshvaran, Matthias Althammer, Andrea Nielsen, Stephan Geprägs, M. S. Ramachandra Rao, Sebastian T. B. Goennenwein, Matthias Opel, and Rudolf Gross. *Epitaxial $Zn_xFe_{3-x}O_4$ thin films: A spintronic material with tunable electrical and magnetic properties*. *Phys. Rev. B*, 79:134405, 2009.
- [26] Ulrike Lüders, Manuel Bibes, Jean-François Bobo, Matteo Cantoni, Riccardo Bertacco, and Josep Fontcuberta. *Enhanced magnetic moment and conductive behavior in $NiFe_2O_4$ spinel ultrathin films*. *Phys. Rev. B*, 71:134419, Apr 2005.
- [27] A. Lisfi, C. M. Williams, L. T. Nguyen, J. C. Lodder, A. Coleman, H. Corcoran, A. Johnson, P. Chang, A. Kumar, and W. Morgan. *Reorientation of magnetic anisotropy in epitaxial cobalt ferrite thin films*. *Phys. Rev. B*, 76:054405, Aug 2007.
- [28] J. A. Moyer, C. A. F. Vaz, D. P. Kumah, D. A. Arena, and V. E. Henrich. *Enhanced magnetic moment in ultrathin Fe-doped Fe_2CoO_4 films*. *Phys. Rev. B*, 86:174404, 2012.
- [29] S. W. Cheong and M. Mostovoy. *Multiferroics: a magnetic twist for ferroelectricity*. *Nature Materials*, 6:13, 2007.

- [30] R. Ramesh, Spaldin, and A. Nicola. *Multiferroics: progress and prospects in thin films*. *Nature Materials*, 6:21, 2007.
- [31] B. H. Liu and J. Ding. *Strain-induced high coercivity in CoFe_2O_4 powders*. *Applied Physics Letters*, 88(4):042506, 2006.
- [32] W. Huang, J. Zhu, H. Z. Zeng, X. H. Wei, Y. Zhang, and Y. R. Li. *Strain induced magnetic anisotropy in highly epitaxial CoFe_2O_4 thin films*. *Applied Physics Letters*, 89(26):262506, 2006.
- [33] J. A. Moyer, D. P. Kumah, C. A. F. Vaz, D. A. Arena, and V. E. Henrich. *Epitaxial strain-induced changes in the cation distribution and resistivity of Fe-doped CoFe_2O_4* . *Applied Physics Letters*, 101(2):021907, 2012.
- [34] S. I. Csiszar, M. W. Haverkort, Z. Hu, A. Tanaka, H. H. Hsieh, H.-J. Lin, C. T. Chen, T. Hibma, and L. H. Tjeng. *Controlling Orbital Moment and Spin Orientation in CoO Layers by Strain*. *Phys. Rev. Lett.*, 95:187205, Oct 2005.
- [35] A. D. Rata and T. Hibma. *Strain induced properties of VO_x thin films*. *The European Physical Journal B*, 43:195, 2005.
- [36] M. E. Fleet. *The structure of magnetite*. *Acta Crystallographica Section B*, B37:917, 1981.
- [37] E. J.W. Verwey. *Electronic Conduction of Magnetite and its Transition Point at Low Temperatures*. *Nature (London)*, 144:327, 1939.
- [38] J. Teillet, F. Bouree, and R. Krishnan. *Magnetic structure of cofe_2o_4* . *Journal of Magnetism and Magnetic Materials*, 123(1):93 – 96, 1993.
- [39] Alex Goldman. *Modern Ferrite Technology*. Springer, 2006.
- [40] L.W. Martin and R. Chu, Y.-H. and Ramesh. *Advances in the growth and characterization of magnetic, ferroelectric, and multiferroic oxide thin films*. *Materials Science and Engineering R*, 68:89, 2010.
- [41] J. A. Venables, G. D. T. Spiller, and M. Hanbucken. *Nucleation and growth of thin films*. *Rep. Prog. Phys*, 47:399, 1984.
- [42] G. Rispen. *Strain and composition effects in epitaxial ferroelectrics*. PhD thesis, Rijksuniversiteit Groningen, 2010.
- [43] S. Csiszar. *X-ray diffraction and X-ray absorption of strained CoO and MnO thin films*. PhD thesis, Rijksuniversiteit Groningen, 2005.
- [44] M. Ohring. *Materials science of thin films*. Academic Press, Sandiego, 2002.

- [45] M. P. Seah and W. A. Dench. *Quantitative electron spectroscopy of surface: A standart data base for electron inelastic mean free patches in solids*. *Surf. Interface Anal*, 1:2, 1979.
- [46] A. D. Rata. *Strained-induced properties of epitaxial VO_x thin films*. PhD thesis, Rijksuniversiteit Groningen, 2004.
- [47] N. Hollmann. *Orbital Occupation and Local Magnetism of Novel transition Metal Oxides*. PhD thesis, Universität zu Köln, 2010.
- [48] Frank de Groot and Akio Kotani. *Core level spectroscopy of solids*. CRC Press, 2008.
- [49] P. W. Anderson. *Magnetism: a treatise on modern theory and materials*. Academic Press, New York, 1963.
- [50] J. B. Goodenough. *Progress in Solid State Chemistry*. Pergamon, Oxford, 1971.
- [51] K. I. Kugel and D. I. Khomskii. *Sov. Phys. Usp*, 25:231, 1982.
- [52] M. Haverkort. *Spin and orbital degrees of freedom in transition metal oxides and oxide thin films studied by soft X-ray absorption spectroscopy*. PhD thesis, Universität zu Köln, 2005.
- [53] F. Reinert and S. Hüfner. *Photoemission spectroscopy-from early days to recent applications*. *New J. Phys*, 7:97, 2005.
- [54] W. Gudat and C. Kunz. *Colse similarity between photoelectric yield and photoabsorption spectra in the sot-x-ray range*. *Phys. Rev. Lett*, 29:169, 1972.
- [55] F.M.F. de Groot. X-ray absorption and dichroism of transition metals and their compounds. *Journal of Electron Spectroscopy and Related Phenomena*, 67(4):529 – 622, 1994.
- [56] C. Mitra, P. Hu, Z.and Raychaudhuri, S. I.and Hsieh H. H.and Lin H.-J.and Chen C. T. Wirth, S.and Csiszar, and L. H. Tjeng. *Phys. Rev. B*, 67:092404, 2003.
- [57] H. Wu, Z. Martin C.and Maignan A. Brunus, T.and Hu, J. C. Cezar, A. Tanaka, N. B. Brookes, D. I. Khomskii, and L. H. Tjeng. *Phys. Rev. Lett*, 102:026404, 2009.
- [58] C. T. Chen, J.and Kao H. L.and Rudolf P.and Sette F. Tjeng, L. H.and Kwo, and R. M. Fleming. *Phys. Rev. Lett*, 68:2543, 1992.

- [59] F. Y. Ran, Y. Tsunemaru, T. Hasegawa, Y. Takeichi, A. Harasawa, K. Yaji, and S. Kim. *Valence band structure and magnetic properties of Co-doped Fe_3O_4 (100)*. *J. Appl. Phys.*, 109:123919, 2011.
- [60] J. A. Moyer, C. A. F. Vaz, D. A. Arena, D. Kumah, E. Negusse, and V. E. Henrich. *Magnetic structure of Fe-doped CoFe_2O_4 probed by x-ray magnetic spectroscopies*. *Phys. Rev. B*, 84:054447, Aug 2011.
- [61] F. C. Voogt, T. Fujii, P. J. M. Smulders, L. Niesen, M. A. James, and T. Hibma. *NO_2 -assisted molecular-beam epitaxy of Fe_3O_4 , $\text{Fe}_{3-\delta}\text{O}_4$, and $\gamma\text{-Fe}_2\text{O}_3$ thin films on $\text{MgO}(100)$* . *Phys. Rev. B*, 60, Oct 1999.
- [62] S.A. Chambers and S.A. Joyce. *Surface termination, composition and reconstruction of Fe_3O_4 (001) and Fe_2O_3 (001)*. *Surface Science*, 420(2):111 – 122, 1999.
- [63] F.C. Voogt. *NO_2 assisted Molecular Beam Epitaxy of Iron Oxide Films*. PhD thesis, Rijksuniversiteit Groningen, 1998.
- [64] C.F. Chang. *Study of Charge, Spin and Orbital States in Strongly Correlated Transition-Metal Oxides*. PhD thesis, Universität zu Köln, 2009.
- [65] J. F. Anderson, Markus Kuhn, Ulrike Diebold, K. Shaw, P. Stoyanov, and D. Lind. *Surface structure and morphology of Mg-segregated epitaxial Fe_3O_4 (001) thin films on $\text{MgO}(001)$* . *Phys. Rev. B*, 56:9902, Oct 1997.
- [66] S.A. Chambers, R.F.C. Farrow, S. Maat, M.F. Toney, L. Folks, J.G. Catalano, T.P. Trainor, and G.E. Brown Jr. *Molecular beam epitaxial growth and properties of CoFe_2O_4 on $\text{MgO}(001)$* . *Journal of Magnetism and Magnetic Materials*, 246(1):124 – 139, 2002.
- [67] A. Ishikawa, J. Nohara, and S. Sugai. *Raman Study of the Orbital-Phonon Coupling in LaCoO_3* . *Phys. Rev. Lett.*, 93:136401, Sep 2004.
- [68] F. Rigato, J. Geshev, V. Skumryev, and J. Fontcuberta. *The magnetization of epitaxial nanometric CoFe_2O_4 (001) layers*. *Journal of Applied Physics*, 106(11):113924, 2009.
- [69] J. X. Ma, D. Mazumdar, G. Kim, H. Sato, N. Z. Bao, and A. Gupta. *A robust approach for the growth of epitaxial spinel ferrite films*. *Journal of Applied Physics*, 108(6):063917, 2010.
- [70] Y. Suzuki, G. Hu, R.B. van Dover, and R.J. Cava. *Magnetic anisotropy of epitaxial cobalt ferrite thin films*. *Journal of Magnetism and Magnetic Materials*, 191(1-2):1 – 8, 1999.

- [71] C.R Brundle, T.J Chuang, and K Wandelt. *Core and valence level photoemission studies of iron oxide surfaces and the oxidation of iron*. *Surface Science*, 68(0):459 – 468, 1977.
- [72] N. S. McIntyre and D. G. Zetaruk. *X-ray photoelectron spectroscopic studies of iron oxides*. *Analytical Chemistry*, 49(11):1521–1529, 1977.
- [73] A. Fujimori, M. Saeki, N. Kimizuka, M. Taniguchi, and S. Suga. *Photoemission satellites and electronic structure of Fe_2O_3* . *Phys. Rev. B*, 34:7318–7328, Nov 1986.
- [74] T. Fujii, F. M. F. de Groot, G. A. Sawatzky, F. C. Voogt, T. Hibma, and K. Okada. *In situ XPS analysis of various iron oxide films grown by NO_2 -assisted molecular-beam epitaxy*. *Phys. Rev. B*, 59:3195–3202, Jan 1999.
- [75] M. O. Krause and J. H. Oliver. *Natural widths of atomic K and L levels, K alpha X-ray lines and several KLL Auger lines*. *Journal of Physical and Chemical Reference Data*, 8(2):329–338, 1979.
- [76] S. Doniach and M. Sunjic. *Many-electron singularity in X-ray photomission and X-ray line spectra from metals*. *Journal of Physics Part C Solid State Physics*, 3(2):285, 1970.
- [77] A. E. Bocquet, T. Mizokawa, T. Saitoh, H. Namatame, and A. Fujimori. *Electronic structure of 3d-transition-metal compounds by analysis of the 2p core-level photoemission spectra*. *Phys. Rev. B*, 46:3771–3784, Aug 1992.
- [78] D.C. Frost, C.A. McDowell, and I.S. Woolsey. *X-ray photoelectron spectra of cobalt compounds*. *Molecular Physics*, 27(6):1473–1489, 1974.
- [79] J.-H. Park, L. H. Tjeng, J. W. Allen, P. Metcalf, and C. T. Chen. *Single-particle gap above the Verwey transition in Fe_3O_4* . *Phys. Rev. B*, 55:12813–12817, May 1997.
- [80] V. I. Anisimov, I. S. Elfimov, N. Hamada, and K. Terakura. *Charge-ordered insulating state of Fe_3O_4 from first-principles electronic structure calculations*. *Phys. Rev. B*, 54:4387–4390, Aug 1996.
- [81] Arata Tanaka and Takeo Jo. *Resonant 3d, 3p and 3s Photoemission in Transition Metal Oxides Predicted at 2p Threshold*. *Journal of the Physical Society of Japan*, 63(7):2788–2807, 1994.
- [82] N. Hollmann, Z. Hu, M. Valldor, A. Maignan, A. Tanaka, H. H. Hsieh, H. H. Lin, Chen, C.T., and L. H. Tjeng. *Electronic and magnetic properties of the kagome systems YBaCo_4O_7 and $\text{YBaCo}_3\text{MO}_7$ ($M=\text{Al, Fe}$)*. *Phys. Rev. B*, 80:085111, 2009.

- [83] Pieter Kuiper, Barry G. Searle, Petra Rudolf, L.H. Tjeng, and C.T. Chen. *X-Ray Magnetic Dichroism of Antiferromagnet Fe_2O_3 : The Orientation of Magnetic Moments Observed by Fe_{2p} X-Ray Absorption Spectroscopy*. *Phys. Rev. Lett*, 70:1549, 1993.
- [84] S. Klein R. Sutarto A. Tanaka J. C. Cezar N. B. Brookes H.-J. Lin H. H. Hsieh C. T. Chen A. D. Rata C. F. Chang, Z. Hu and L. H. Tjeng. *Initial stages of epitaxial growth of the polar $\text{Fe}_3\text{O}_4/\text{MgO}$ (001) thin films: a new path to cure the polar catastrophe at the interface. to be submitted in Phys. Rev. Lett.*
- [85] R. M. Bozorth, Elizabeth F. Tilden, and Albert J. Williams. *Anisotropy and Magnetostriction of Some Ferrites*. *Phys. Rev.*, 99:1788–1798, Sep 1955.
- [86] Masashi Tachiki. *Origin of the Magnetic Anisotropy Energy of Cobalt Ferrite*. *Progress of Theoretical Physics*, 23:1055, 1960.
- [87] R.F Penoyer. *Origin of the Magnetic Anisotropy Energy of Cobalt Ferrite*. *Progress of Theoretical Physics*, 23:1055, 1960.
- [88] T. Dhakal, D. Mukherjee, R. Hyde, P. Mukherjee, M. H. Phan, H. Srikanth, and S. Witanachchi. *Magnetic anisotropy and field switching in cobalt ferrite thin films deposited by pulsed laser ablation*. *Journal of Applied Physics*, 107(5):053914, 2010.
- [89] S. Matzen, J.-B. Moussy, R. Mattana, F. Petroff, C. Gatel, B. Warot-Fonrose, A. Cezar, J. C. and Barbier, M.-A. Arrio, and Ph. Saintavit. *Restoration of bulk magnetic properties by strain engineering in epitaxial CoFe_2O_4 (001) ultrathin films*. *Appl. Phys. Lett*, 99:052514, 2011.
- [90] H.-J. Lin, Y. Y. Chin, Z. Hu, G. J. Shu, F. C. Chou, H. Ohta, K. Yoshimura, S. Hébert, A. Maignan, A. Tanaka, L. H. Tjeng, and C. T. Chen. *Local orbital occupation and energy levels of Co in Na_xCoO_2 : A soft x-ray absorption study*. *Phys. Rev. B*, 81:115138, Mar 2010.
- [91] F. T. and Rudee M. L. and Spada F. E. Margulies, D. T. and Parker, J. N. Chapman, P. R. Aitchison, and A. E. Berkowitz. *Origin of the Anomalous Magnetic Behavior in Single Crystal Fe_3O_4 Films*. *Phys. Rev. Lett*, 79:5162, 1997.
- [92] F. C. Hibma, T. and Voogt, P. A. A. and de Jonge W. J. M. and Donkers J. J. T. M. Niesen, L. and van der Heijden, and P. J. van der Zaag. *Anti-phase domains and magnetism in epitaxial magnetite layers*. *J. Appl. Phys.*, 85:5291, 1999.

Abstract

Magnetite (Fe_3O_4) is one of the transition metal (TM) oxide compounds which has promising applications in microelectronic and microwave devices as well as sensitive sensors. These possible applications are derived from the strongly correlated 3d electrons occupying the incomplete 3d orbitals in the transition metal cations. Fe_3O_4 has an inverse spinel structure where the Fe cations have two valence states; Fe^{2+} and Fe^{3+} ions. The Fe^{2+} ions reside in the octahedral (B) sites only, while the Fe^{3+} ions are split between the tetrahedral and the octahedral sites.

This thesis will present a study of substitution, thickness and strain effects in $\text{Fe}_{3-x}\text{Co}_x\text{O}_4$ compounds. The Co-substitution was carefully tuned to obtain films with the following stoichiometry, $\text{Fe}_{3-x}\text{Co}_x\text{O}_4$ with $x = 0, 0.1, 0.5$ and 1 . The discussion about the structural, electronic and magnetic properties will be presented based on comprehensive measurements. Afterwards, three different film thicknesses (5ML, 20ML, and 20nm) of Fe_3O_4 and Fe_2CoO_4 will be scrutinized to give an impression about the initial stages of the growth process. In the last part, the effect of different strain states induced by various substrates will be also discussed. All samples in this thesis were prepared by using the Molecular Beam Epitaxy (MBE) technique.

The Co element as the substitution agent induces magnetic anisotropy in $\text{Fe}_{3-x}\text{Co}_x\text{O}_4$ compounds. It modifies structural, electronic and magnetic properties of $\text{Fe}_{3-x}\text{Co}_x\text{O}_4$ films. The amount of substitution tunes the conductivity of $\text{Fe}_{3-x}\text{Co}_x\text{O}_4$ films. The resistivity and density of states near the Fermi energy of $\text{Fe}_{3-x}\text{Co}_x\text{O}_4$ vary systematically upon substitution. Various techniques were employed to investigate the properties of $\text{Fe}_{3-x}\text{Co}_x\text{O}_4$ films. Reflection High-Energy Electron Diffraction (RHEED), Low-Energy electron Diffraction (LEED) and X-Ray Diffraction (XRD) measurements were used to confirm the structure and the film quality. However, substitution Co atoms into spinel structure may reshuffle the site occupations in the structure. The oxidized Fe may have many possible valencies, i.e., Fe^{2+} or Fe^{3+} , while Co ion may endure Co^{2+} or Co^{3+} valencies. These ions will reside in two possible sites, i.e., octahedral or tetrahedral. In order to investigate these issues, X-ray Photoelectron Spectroscopy (XPS) was used to check the chemical composition and the electronic structure of $\text{Fe}_{3-x}\text{Co}_x\text{O}_4$ films. In addition, X-ray Absorption Spectroscopy (XAS) was employed to this system due to its site and symmetry selective character. Both results confirm that the Fe^{2+} ions in octahedral site is replaced by the Co^{2+} ions which are also sitting in octahedral site. Finally, SQUID magnetometry was utilized to determine the bulk magnetic properties and

specify the magnetic easy axis of $\text{Fe}_{3-x}\text{Co}_x\text{O}_4$ films. It verifies that the magnetic easy axis turns from in-plane direction for Fe_3O_4 films to out-of-plane direction for doped films.

The thickness dependent study of Fe_3O_4 and Fe_2CoO_4 films suggests that both ferrites share a generic growth mechanism. The Fe ions in the octahedral sites are mainly populated whereas those in the tetrahedral sites are nearly empty at the beginning of growth. Sustaining the stage of film growth, the population of the Fe ions in the tetrahedral sites gradually increases while those in the octahedral sites gradually declines until they reach a balanced ratio.

The Fe_2CoO_4 films have been grown epitaxially on three different substrates, MgO, MgAl_2O_4 and SrTiO_3 as a model system for Fe_2CoO_4 under epitaxial strain. Theoretically, based on the lattice mismatch between the film and the substrate, the MgO substrate induces tensile strain while the other two substrates (SrTiO_3 and MgAl_2O_4) induce compressive strain. The structural studies from RHEED, LEED and XRD measurements showed that Fe_2CoO_4 films grow coherently on MgO and MgAl_2O_4 substrates but on SrTiO_3 substrate the growth was relaxed. Fe_2CoO_4 film could not follow the strain induced by SrTiO_3 substrate due to a big lattice mismatch between them. As a consequence, Fe_2CoO_4 films grown on SrTiO_3 substrate experienced tensile-like strain even though the lattice mismatch would indicate a preference for compressive strain. SQUID result showed that strained Fe_2CoO_4 films have an out-of-plane magnetic easy axis while compressed Fe_2CoO_4 films have an in-plane magnetic easy axis. This finding is also supported by the XLD results. The XLD results also explain the effect of strain on the orbital occupation in Co^{2+} cations. The Co^{2+} cations in strained Fe_2CoO_4 film have out-of-plane orbital moment and spin moment. The other way around was observed for films grown under compressive strain. These findings give a new perspective about magnetic anisotropy behavior induced by substrate strain in Fe_2CoO_4 films.

Kurzzusammenfassung

Magnetit (Fe_3O_4) gehört zu den Übergangsmetalloxiden, die vielversprechende Anwendungen in Mikroelektronik- und Mikrowellengeräten sowie empfindlichen Sensoren haben. Diese potentiellen Anwendungen haben ihren Ursprung in den stark korrelierten 3d Elektronen, die die unvollständig gefüllten 3d Orbitale besetzen. Fe_3O_4 hat eine inverse Spinell-Struktur, in der die Fe-Kationen zwei Valenz-Zustände haben: Fe^{2+} - und Fe^{3+} -Ionen. Die Fe^{2+} -Ionen befinden sich nur auf den oktaedrischen (B) Plätzen, während die Fe^{3+} -Ionen auf die tetraedrischen und oktaedrischen Plätze aufgeteilt sind.

Diese Arbeit zeigt eine Studie von Substitutions-, Dicke-, und Verspannungseffekten in $\text{Fe}_{3-x}\text{Co}_x\text{O}_4$ -Verbindungen. Die Co-Substitution wurde sorgfältig abgestimmt, um Filme mit folgenden Stöchiometrien zu erhalten: $\text{Fe}_{3-x}\text{Co}_x\text{O}_4$ mit $x = 0; 0,1; 0,5$ und 1. Die strukturellen, elektronischen und magnetischen Eigenschaften werden auf Basis umfangreicher Messungen diskutiert. Im Anschluss werden drei Schichtdicken (5 ML, 20 ML und 20 nm) untersucht, um einen Eindruck von den anfänglichen Phasen des Wachstumsprozesses zu erhalten. Im letzten Teil wird auch der Effekt von verschiedenen Verspannungszuständen, hervorgerufen durch verschiedene Substrate, diskutiert. Alle Proben in dieser Arbeit wurden mit der Molekularstrahlepitaxie-Technik hergestellt.

Das Element Co als Substitutionsstoff ruft eine magnetische Anisotropie in $\text{Fe}_{3-x}\text{Co}_x\text{O}_4$ -Verbindungen hervor. Es verändert die strukturellen, elektronischen und magnetischen Eigenschaften von $\text{Fe}_{3-x}\text{Co}_x\text{O}_4$ -Filmen. Der Substitutionsgrad stellt die Leitfähigkeit von $\text{Fe}_{3-x}\text{Co}_x\text{O}_4$ -Filmen ein. Durch Substitution ändern sich der spezifische Widerstand und die Zustandsdichte nahe der Fermi-Energie von $\text{Fe}_{3-x}\text{Co}_x\text{O}_4$ -Filmen systematisch. Um die $\text{Fe}_{3-x}\text{Co}_x\text{O}_4$ -Filme zu untersuchen und deren Eigenschaften zu überprüfen, wurden verschiedene Techniken eingesetzt. Reflektive Hochenergie-Elektronenbeugung (RHEED, Reflection High-Energy Electron Diffraction), Niedrigenergie-Elektronenbeugung (LEED, Low-Energy Electron Diffraction) und Röntgenbeugung (XRD, X-Ray Diffraction) wurden benutzt, um die Struktur und die Filmqualität zu bestätigen. Das Substituieren von Co-Atomen in die Spinell-Struktur kann jedoch die Belegung der Plätze in der Struktur umverteilen. Das oxidierte Fe kann viele mögliche Valenzen haben, d.h. Fe^{2+} oder Fe^{3+} , während das Co Valenzen von Co^{2+} oder Co^{3+} annehmen kann. Diese Ionen halten sich an zwei möglichen Plätzen auf, d.h. oktaedrisch oder tetraedrisch. Um diese Punkte zu untersuchen, wurde Röntgen-Photoelektronenspektroskopie (XPS, X-ray Photoelectron Spectroscopy) zur Überprüfung der chemischen Zusammensetzung und der elektronischen Struktur der $\text{Fe}_{3-x}\text{Co}_x\text{O}_4$ -Filme benutzt. Zusätzlich

wurde Röntgenabsorptionsspektroskopie (XAS, X-ray Absorption Spectroscopy) an diesem System eingesetzt, weil diese Methode Platz- und Symmetrie-spezifisch ist. Beide Ergebnisse bestätigen, daß die Fe^{2+} -Ionen auf den Oktaeder-Plätzen durch die Co^{2+} -Ionen ersetzt werden, die auch auf den Oktaeder-Plätzen sitzen. Schließlich wurde SQUID Magnetometrie benutzt, um die magnetischen Volumen-Eigenschaften zu bestimmen und die magnetische Vorzugsrichtung der $\text{Fe}_{3-x}\text{Co}_x\text{O}_4$ -Filme anzugeben. Es bestätigt, daß die magnetische Vorzugsrichtung in substituierten Fe_3O_4 -Filmen sich von einer Richtung in der Ebene (in reinem Fe_3O_4) zu einer Richtung außerhalb der Ebene dreht.

Die Schichtdicken-abhängige Untersuchung von Fe_3O_4 - und Fe_2CoO_4 -Filmen deutet darauf hin, dass beide Ferrite einen generischen Wachstums-Mechanismus haben. Zu Beginn des Wachstums werden hauptsächlich die Fe-Ionen auf den Oktaeder-Plätzen bevölkert, während die auf den Tetraeder-Plätzen nahezu leer sind. Bei fortwährendem Filmwachstum nimmt die Bevölkerung mit Fe-Ionen auf den Tetraeder-Plätzen schrittweise zu, während sie auf den Oktaeder-Plätzen schrittweise abnimmt bis sie ein ausgeglichenes Verhältnis erreicht.

Die Fe_2CoO_4 -Filme wurden epitaktisch gewachsen auf drei verschiedenen Substraten, MgO , MgAl_2O_4 und SrTiO_3 als Modell-System für Fe_2CoO_4 unter epitaktischer Spannung. Theoretisch, aufgrund der Gitter-Fehlanpassung zwischen Film und Substrat, verursacht das MgO -Substrat Zugspannung, während die anderen zwei Substrate (SrTiO_3 und MgAl_2O_4) Stauchspannung verursachen. Die Strukturuntersuchungen aus RHEED-, LEED und XRD-Messungen zeigten, dass ein Fe_2CoO_4 -Film kohärent auf MgO - und MgAl_2O_4 -Substraten wächst, aber das Wachstum auf SrTiO_3 entspannt verläuft. Der Fe_2CoO_4 -Film konnte durch die große Gitter-Fehlanpassung nicht der Spannung folgen, die durch das SrTiO_3 hervorgerufen wird. Infolgedessen erfuhr der Fe_2CoO_4 -Film auf einen SrTiO_3 -Substrat Zugspannung, obwohl die Gitter-Fehlanpassung auf einen Vorzug für Stauchspannung hindeutet. SQUID Ergebnisse zeigten, dass ein verspannter Fe_2CoO_4 -Film eine magnetische Vorzugsrichtung außerhalb der Ebene hat, während ein komprimierter Fe_2CoO_4 -Film eine magnetische Vorzugsrichtung in der Ebene hat. Diese Erkenntnis wird auch von XLD-Ergebnissen unterstützt. Die XLD-Ergebnisse erklären auch den Effekt von Spannung auf die orbitale Besetzung in Co^{2+} -Kationen. Die Co^{2+} -Kationen in verspannten Fe_2CoO_4 -Filmen haben ein orbitales Moment und Spin-Moment außerhalb der Ebene. Umgekehrtes wurde für Filme beobachtet, die mit Stauchspannung gewachsen sind. Diese Erkenntnisse geben eine neue Perspektive auf das magnetische Anisotropie-Verhalten, das in Fe_2CoO_4 -Filmen durch Substrat-Spannung hervorgerufen wird.

Acknowledgement

It was a great pleasure having a chance to carry out my PhD studies under the EU SORANO project at the Department of Physics II at the University of Cologne, and Max-Planck-Institute CPfS Dresden. I would like to thank all the people who made this thesis possible and supported during my PhD journey.

First of all, I would like to thank Prof. L. H. Tjeng, thank you for your support and giving me the opportunity to work in your group. I have learned a lot from your lectures and discussions. It enriches my experiences in the thin films world.

Prof. T. Michely, thank you very much for refereeing my thesis and giving me the opportunity to complete my PhD in Uni-Köln.

I would also thanks to Prof. M. O. Tjia and Agung Nugroho for recommending and convincing me to this PhD study. You are the ones who help me to build my paths in this great scientific world.

Diana Rata, thank you for teaching me to get deep in the thin film science. You are not just a supervisor for me but also as a friend, where I can also talk of other things with you. It makes me feel safe even I am far away from my country.

Ronny Sutarto, thank you for reading and correcting my thesis several times and also for all the supports during my PhD study. Even we are Indonesian friends, but you look like my remote supervisor.

Zhiwei Hu, thank you for teaching me XAS and also many thanks for your helps with the XAS data. It is also a pleasure to work and discuss with you.

Stefano Agrestini, thank you for reading and correcting my XPS chapter. It is also a pleasure to discuss physics with you.

Jonas Wienen and Tim Haupricht, thank you for assisting me in the beginning my PhD to get used with the HBFG chamber. It is also a pleasure to discuss physics with you. Also special thanks to Jonas who is helping me to translate my abstract into German.

I would like to express my gratitude to my colleagues Anna Efimenko, Simone Altendorf, Yi-Ying Chin, Nils Hollmann, Martin Rotter, Roger Chang, Chang-Yang Kuo, Katharina Höfer, Xionghua Liu, and Fabio Strigari. Anna, thank you very much for your great support in the last years. You are a best friend for me. Hopefully our friendship will last forever even though we are far away then. Simone, thank you for accompanying me in hospital last time. Yi-Ying, Chang-Yang and Roger, thank you so much to share your experience on XAS measurement in Taiwan. Yi-Ying, it is also nice to spend our time together along SOPRANO program. Nils and Martin, thank you to share your knowledge on XAS theory and also

always available to answer my questions. Katharina, Liu and Fabio, it is also nice to work with you in the same lab.

Special thanks to Claudia Strohbach, Andrea Severing, Anke Riebe, and Thomas Koethe for helping me to deal with all the administration process. You have made my life in Germany became easier.

A big thank goes also to the technical staff: Lucie Hamdan, Uwe, Thomas Mende, and Christoph Becker for all the preparation and help in the background.

Furthermore, I would also thank to the EU SOPRANO project and also people within the SPORANO project, especially: Sylvie Herbert, Mathieu Le Tacon, and Magali Kerdreux. I also want to thank for the support from Max-Plank Institute FKF Stuttgart, where I was employed for 1 year.

Finally, I would like to express my deepest gratitude to my family. My parents (Hasdi Aimon and Rita Helmi), thank you very much for you full support. I can be at this stage because of you everlasting support and prays. My parents-in-law (Maryadi and Siti Zainah), thank you for your care, pray and always try to help me with your best. My dearest husband (Arie Wibowo), thank you to let me reach my dream and far away from you in the last 4 years. Hopefully these struggle and sacrifice will give us a better life future for our little family. My lovely daughter (Aqeela Freda Wibowo), thank you for being born from my womb, a mother who is fighting for her PhD studies. You are my spirit since you were in my womb until now as my little girl. Hopefully this journey can inspire you in the future. My brother and sisters (Alfajri, Ratih and Arhimny), thank you so much for your supports and helps.

Erklärung

Ich versichere, dass ich die von mir vorgelegte Dissertation selbständig angefertigt, die benutzten Quellen und Hilfsmittel vollständig angegeben und die Stellen der Arbeit - einschließlich Tabellen, Karten und Abbildungen-, die anderen Werken im Wortlaut oder dem Sinn nach entnommen sind, in jaden Einzelfall als Entlehnung kenntlich gemacht habe; dass diese Dissertation noch keiner anderen Fakultät oder Universität zur Prüfung vorgelegen hat; dass sie - abgesehen von unten angegebenen Teilpublikationen - noch nicht veröffentlicht worden ist sowie, dass ich eine solche Veröffentlichung vor Abschluss des Promotionsverfahrens nicht vornehmen werde. Die Bestimmungen der Promotionsordnung sind mir bekannt. Die von mir vorgelegte Dissertation ist von Prof. Dr. L. H. Tjeng und Prof. Dr. T. Michely betreut worden.



Akfiny Hasdi Aimon

Curriculum vitae

Name: Akfiny Hasdi Aimon
Date of birth: 14th of April 1984
Place of birth: Padang (Indonesia)
Nationality: Indonesian

1990-1996 Elementary School "SDN no. 23" in Padang - Indonesia
1996-1999 Junior High School "SMPN no. 7" in Padang - Indonesia
1999-2002 Senior High School "SMUN no.2" in Padang - Indonesia
2002-2006 Institut Teknologi Bandung - Indonesia
Bachelor thesis under the supervision of Prof. Mitra Djamal
2007-2009 Institut Teknologi Bandung - Indonesia
Master thesis under the supervision of Prof. Petra Rudolf and Dr. Yudi Darma
2008-2009 Rijksuniversitaet Groningen - the Netherlands
Exchange student in the group of Prof. Petra Rudolf
Aug. 2009 II. Physikalisches Institut, Universität zu Köln - Germany
Ph.D. study under the supervision of Prof. Liu Hao Tjeng

